Heat Transfer of HVAC Cables Installed in Underground Pipes Buried in Layered Soil

By

Zhongtian Li

in fulfilment of the requirements for the degree of

Master of Science
in Electrical Power Engineering

at the Delft University of Technology,
to be defended publicly on Thursday July 30, 2020 at 10:00 AM.

Supervisor:	Dr. ir. Mohamad Ghaffarian Niasar	TU Delft
	Prof.ir. Peter Vaessen	TU Delft
	Dr. ir. Mohsen Kavian	DNV GL
	ir. Frank de Wild	DNV GL
Thesis committee:	Prof.ir. Peter Vaessen	TU Delft
	Dr. ir. Mohamad Ghaffarian Niasar	TU Delft
	Dr. Aleksandra Lekic-Vervoort	TU Delft
	Dr. ir. Mohsen Kavian	DNV GL

Table of contents

List of figures

Abstract

HVAC cable is normally installed in a PE (Polyethylene) pipe underground. The pipe is placed in the underground path formed by horizontal directional drilling (HDD). During power transmission, the generated heat from the cable is dissipated by natural convection of water in the gap between cable and pipe. In this project, the first part focuses on the analysis of natural convection in water in the annulus space formed by a cable-pipe boundary. The second part simulates the heat dissipation process of the underground cable-water-pipe system with the influence of the layered soil. The temperature distribution along the HDD path shows an abnormal variation due to different thermal conductivity of soil layer, which causes some hotspots to form on the surface of the pipe.

Heat transfers by conduction, convection and radiation. In this project, only conduction and convection are considered. The thermal radiation analysis is not considered and reserved for future study. Convection can only occur in fluid (liquid or gas). In convection mode, the fluid near the heat source which gains energy become less dense and rises forming a convection flow. The thesis covers two main sections. The first section covers analysis of two problems: the first one is the study of natural convection in the concentric annulus (corresponds to the geometry of cable at the centre of the pipe) and the second one is the natural convection analysis in the eccentric annulus (corresponds to the geometry that cables touches the pipe bottom due to gravity). For the concentric annulus, the highest temperature occurs in the top region of the annulus. For the eccentric annulus, the highest temperature occurs in the narrow region where the inner cylinder touches the outer cylinder. Generally, in the laminar flow regime, the eccentric annulus has a poorer heat transfer rate compared to the concentric annulus.

In the second section, a time-dependent model based on the HDD scenario is built in COMSOL, taking into account the influence of natural convection in water and inhomogeneous thermal conductivity of layered soil. The heat transfer process from the cable to the soil along the HDD path is simulated. The heat dissipation rate from the pipe to soil varies due to different thermal conductivity of each soil layer, which causes unpredictable temperature changes at different position of the pipe surface. Hence, some hotspots form on the surface of the pipe. The location of hotspots is detected by numerical modelling in COMSOL. The simulation model can be used in the future for localization of potential hotspots and cable life calculation.

Acknowledgement

Nomenclature

c_p = specific heat, (SI units: J/kg · K)

D_i = inner cylinder diameter

D_o = outer cylinder diameter

g = acceleration due to gravity.

h = local heat transfer coefficient

k = thermal conductivity of medium, W/m · K

$\overline{k_{eq}}$ = average equivalent conductivity, $\overline{k_{eq}} = \dfrac{\overline{Nu}}{Nu_{cond}}$

L = characteristic length of concentric cylinder geometry, $L = \dfrac{D_o - D_i}{2}$

Nu = Nusselt number, $Nu = \dfrac{hL}{k}$

Pr = Prandtl number, $Pr = \dfrac{c_p \mu}{k} = \dfrac{v}{\alpha}$

p_{ref} = reference pressure

R_i = inner cylinder radius

R_o = outer cylinder radius

Ra_{D_i} = Rayleigh number of inner cylinder, $Ra_{D_i} = \dfrac{g\beta}{v\alpha}(T_i - T_o)D_i^{\,3}$

Ra_{D_o} = Rayleigh number of inner cylinder, $Ra_{D_o} = \dfrac{g\beta}{v\alpha}(T_i - T_o)D_o^{\,3}$

Ra_L = Rayleigh number based on radius difference, $Ra_L = \dfrac{g\beta}{v\alpha}(T_i - T_o)L^3, L = \dfrac{D_o - D_i}{2}$

Re = Reynolds number, $Re = \dfrac{\rho u_{avg} L}{\mu} = \dfrac{u_{avg} L}{v}$

T_{ref} = reference temperature, K

T_i = Inner cylinder temperature, K

T_o = Outer cylinder temperature, K

u_{avg} = average speed of fluid, m/s

Subscripts

α = thermal diffusivity, $\alpha = k/(\rho c_p)$, m²/s

β = coefficient of thermal expansion(equals to $1/T_0$ for ideal gases, T_0 is absolute temperature), indicates the rate of change of density with respect to temperature at constant temperature.

v = kinematic viscosity (momentum diffusivity), $v = \mu/\rho$, m²/s

ρ = density of medium, kg/m³

ρ_0 = constant density at reference temperature and reference pressure, kg/m³

μ = dynamic viscosity, Pa s = N s/m²

1 INTRODUCTION

1.1 Background

Heat transfers by conducion, convection and radiation. Conduction is a mechanism in which heat transfers from a hotter object towards a colder object, which at a macroscoptic level requires direct contact (e.g., heating a pot on a stove). Convection is the heat transfer process that happens in the flow of the fluids (liquids or gases) [1]. The convection phenomenon can be detected by injecting dye into warm water and observing the motion path of the dye. During the convection process, the heated fluid becomes less dense and rises due to the buoyancy force. The cooler fluid is forced to move down and a convection flow estabilishes. Unlike the previous two mechanisms, radiation does not require a medium to transmit energy. Through electromagnetic radiation, all physical substances in solid, liquid, or gaseous states can radiate energy by molecules movement [2]. A typical example is the solar radiation, which increases the temperature of the earth's surface. This project concentrates on the analysis of convective heat transfer in the water (which filled in the annulus between pipe and cable) and conductive heat transfer from the water pipe to the surrounding soil. The thermal radiation analysis is not covered and reserved for future study.

The HVAC cable (inner cylinder, 2500 mm^2 Cu XLPE) is normally installed inside a SDR11 HDPE pipeline (wall thickness: 22.7 mm, depth: 20-25 m) buried underground. The cable lies at the bottom region of the pipe and the configuration of the layout is like an eccentric cylinder (annulus). The pipeline path (length: 500 m) is formed by horizontal directional drilling (HDD). The path of HDD crosses the layered soil with different thermal conductivity. During power transmission, heat is produced due to ohmic loss of the cable conductor, sheath loss as well as dielectric loss. The heat dissipation relies on the heat convection in fluid and heat conduction through the wall of pipe, which penetrates the heat onto the surface of pipe and then through soil. The temeperature along the pipeline varies due to different thermal conductivity of each soil layer. The area where the temperature becomes extremely higher than its surrounding along the pipe is called local hotspot.
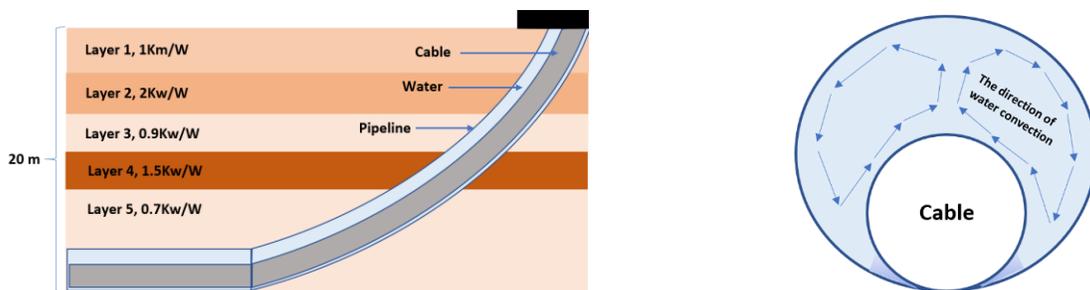
Figure 1-1: Scenario illustration (a) longitudinal direction; (b) transverse direction;

1.2 Scenario Data

The environmental ambient temperature changes with cable burial depth:

Burial Depth	Temperature C
0-5 m	15
5-10 m	12
>10 m	10

Scenario for Horizontal Directional Drilling (HDD) buried in layered soil:

- Consider a Horizontal Directional Drilling, with one cable in one pipe.
- Length of pipe: about 500 m
- Depth of pipe: about 20-25 meters
- Entry and exit points of the inclined part of the pipe make an angle of 18 degrees with the horizontal part of the pipe. The ends of the pipe are sealed such that it is ensured the pipe will always be full of water.
- The bending radius with which the pipe reaches the bottom (20-25 m) is 200 m.
- Type of pipe: SRD11 (outer cross section 250 mm, wall thickness: 22.7 mm).
- Suppose the following is considered for soil thermal conductivity variation with depth;
  - Layer 1: vertical depth (0-5 m) : 1 W/m · K
  - Layer 2: vertical depth (5-8 m) : 2 W/m · K
  - Layer 3: vertical depth (8-12 m) : 0.9 W/m · K
  - Layer 4: vertical depth (12-15 m) : 1.5 W/m · K
  - Layer 5: vertical depth (15m or more) : 0.7 W/m · K

  Note: the pipe crosses all these layers.
- The cable is a normal 2500 mm2 Cu XLPE insulated power cable for 400 kV AC. The size values of the corresponding model are listed as follow:
  - Copper conductor of 2500 mm2, diameter approximately 61.3 mm.
  - Semiconductor screens and insulation with total thickness of 30.0 mm (15.0 mm on each side)
  - Copper wire screen using 1.5 mm thick wires, total cross section 150 mm2
  - Polyester tapes of 2 mm
  - Lead sheath with thickness of 2.5 mm
  - PE sheath with thickness of 5.5 mm
  - Outer diameter: about 145 mm.
- The temperature and losses are considered based on the following values:
  - The maximum allowable cable conductor temperature is 90 °C and the corresponding temperature on the outer sheath is 78.73 ± 0.005 °C.
  - The heat production in the conductor is given by $Q = I^2 R_{ac}$, in which R_{ac} is temperature dependent and dependent on skin effect factors, etc. In this thesis, the conductor losses is considered as constant: $Q = 31.72$ W/m (but note that in reality as the resistance is temperature dependent, the losses will depend on temperature).

1.3 Objective

1 - To setup boundary conditions of conduction and convection heat transfer in unit space model in COMSOL.

2 - To construct 2D models to study the heat transfer rate of fluid in concentric and eccentric annulus and to compare the results with relevant literature.

3 - To study temperature distribution along a vertical cable-pipe structure placed in a multilayer soil structure

4 - To develop a 3D model based on the scenario of a HDD path (in which a cable is installed in a water pipe buired in layered soil), taking into account conductive and convective heat transfer process in order to identiy temperture distribution and location of hotspots.

The general aim of this project is:

To develop a 3D time-dependent model in COMSOL, taking into account of laminar flow in fluids, heat transfer in soilds and fluids, to investigate the influence of layered soil structure on temperature distribution and location of hotspots along the HDD path (in which a cable inside a water pipe buried underground).

1.4 Structure of thesis

The outline of this thesis is as follows:

Chapter 2:

This chapter explains concepts involved in this project. The deduction process of the full Navier-Stokes equation and the applied condition of Bousssinesq approximation are demonstrated. Three different approaches to derive Navier-Stokes equation in COMSOL are discussed and classified according to their characteristics. The categories of flow compressibility are classified and the dimensionless quantities concerned in this project are introduced. Relevant empirical equations and how to calculate heat flux in the annular are shown.

Chapter 3:

This chapter applies the classical benchmark method in [3] to account for the buoyancy flow formed due to temperature difference in free fluids in the unit space. The buoyancy flow is formed due to temperature change (which causes the density variation) in the fluid. All the simulations in this thesis are implemented in COMSOL. To validate the modelling accuracy, the classical benchmark method is used to analyse the natural convection process in unit square and cubical model to make preparation for the simulations in the following chaptes. The models in this chapter are built based on dimensionless quantities.

Chapter 4:

In this chapter, dimensionless models are applied to observe the influence of dimensionless parameters, such as Rayleigh number and Prandtl number, to the motion of free fluid in annulus. After converting Navier-Stokes equations and energy equation to dimensionless form, a general solution can be derived to describe relevant scenario cases. Concentric/eccectric cylinders are built in horizontal and vertical direction considering different combination of Ra, Pr and length of the annulus. An initial dimensionless model is built as preparation for the scenario model simulation in the following chapter. Numerical simulations are implemented with the new combination of Ra and Pr, which has not been covered in the reference papers, to make further prediction of the free fluid motion.

Chapter 5:

In this Chapter, dimensional model is built in COMSOL to derive solution in specific scenario cases. The exported results from COMSOL are compared to experimental data in relevant papers to make further motifcation of the boundary condition setting to improve the simulation quality. The dimensional models of 2D concentric and ecctric cylinders are compared to Kuehn's work in [4] and in [5]. 3D horizontal concentric/eccentric cylinders are built to observe the impact of end effects to the heat transfer process. A vertical axisymmetric concentrical cylinder model is built to observe the influence of layed soil to the heat dissipation process. Finally, the model based on scenario data is built to detect the temperature distribution and location of hotspots along the pipeline.

Note: Since relevant experiment is difficult to be executed, the accuracy of this thesis project highly relies on comparison with experimental/numerical results in relevant papers. The original scenario model has been decomposed into several annulus sections in horizontal, vertical and inclined direction to analyse step by step. The reason why doing this is because it is too difficult to consider all the boundary conditions in the beginning and decide if the settings are correct or wrong, compulsory or not. Hence, the model is modified and corrected in this approach progressively.

2 LITERATURE REVIEW

This chapter includes explanation of all concepts involved in this project. In Section 2.2, the deduction process of the full Navier-Stokes equation is demonstrated. Section 2.3 clearly elaborates the applied condition of Bousssinesq approximation, which is a method to address nonisothermal flow issues with no need to solve Navier-Stokes equations completely. Three different approaches to derive Navier-Stokes equation in COMSOL are discussed and sorted into different applied scenarios according to their characteristics. In Section 2.4, the categories of flow compressibility are distinguished according to their respective continuity and momentum equations applied for fluid motion analysis. In Section 2.5, the dimensionless quantities concerned in this project are introduced and one empirical equation sutiable for analysis of annular space between horizontal concentric cylinders is shown, which can be used for the initial evaluation of heat transfer coefficient in this scenario.

2.1 Horizontal Directional Drilling

In this project, the path where the pipe is installed is built by HDD technique. Horizontal directional drilling (HDD) is a type of pipe installation technique. There are three main stages for one HDD project: localizaition and path planning, reaming and pipe installation. It is suitable to apply this technique in the area where the underground structure and enviroment such as railroad, river and urban region. During constructions, no disruption occurs to any feature being crossed by the HDD installation. The HDD technique make the pipe installation possible in these environement sensitive areas. The impact of the HDD to the underground environment can be reduced to minimum with appropriate plannig and design.

2.2 Navier-Stokes Equations

The Navier-Stokes equation was originally derived for an inviscid fluid based on Newton's laws of motion $f = ma$. It basically describes how fluid velocity changes with time. The change of pressure $-\nabla p$ equals to the fluid density ρ times the material derivative of the velocity field $\frac{D\boldsymbol{u}}{Dt}$ (which represents acceleration). The material derivative $\frac{D\boldsymbol{u}}{Dt}$ computes the time rate of change of velocity for a portion of a material moving with a velocity, $\boldsymbol{u}$. Hence, with the definition of material derivative of velocity field, the Navier-Stokes equation can be expanded to:

$$f = -\nabla p = ma = \rho \frac{D\boldsymbol{u}}{Dt}(t, x, y, z) \qquad \text{2-1}$$

$$\rho \frac{D\boldsymbol{u}}{Dt}(t, x, y, z) = \rho(\frac{\partial \boldsymbol{u}}{\partial t} + \frac{\partial \boldsymbol{u}}{\partial x}\frac{\partial x}{\partial t} + \frac{\partial \boldsymbol{u}}{\partial y}\frac{\partial y}{\partial t} + \frac{\partial \boldsymbol{u}}{\partial z}\frac{\partial z}{\partial t}) = \rho(\frac{\partial \boldsymbol{u}}{\partial t} + u_x \frac{\partial \boldsymbol{u}}{\partial x} + u_y \frac{\partial \boldsymbol{u}}{\partial y} + u_z \frac{\partial \boldsymbol{u}}{\partial z}) = \rho(\frac{\partial \boldsymbol{u}}{\partial t} + \boldsymbol{u} \cdot \nabla \boldsymbol{u})$$

$$-\nabla p = \rho(\frac{\partial \boldsymbol{u}}{\partial t} + \boldsymbol{u} \cdot \nabla \boldsymbol{u}) \qquad \text{2-2}$$

When the shear stresses are included, an extra viscous force term $\mu(\frac{\partial^2 \boldsymbol{u}}{\partial x^2} + \frac{\partial^2 \boldsymbol{u}}{\partial y^2} + \frac{\partial^2 \boldsymbol{u}}{\partial z^2})$ appears in the equation:

$$-\nabla p + \mu(\frac{\partial^2 \boldsymbol{u}}{\partial x^2} + \frac{\partial^2 \boldsymbol{u}}{\partial y^2} + \frac{\partial^2 \boldsymbol{u}}{\partial z^2}) = \rho(\frac{\partial \boldsymbol{u}}{\partial t} + \boldsymbol{u} \cdot \nabla \boldsymbol{u})$$

$$-\nabla p + \mu \nabla^2 \boldsymbol{u} = \rho(\frac{\partial \boldsymbol{u}}{\partial t} + \boldsymbol{u} \cdot \nabla \boldsymbol{u}) \qquad \text{2-3}$$

The symbol μ represents the dynamic viscosity. In this project, water and air can be considered Newtonian. The dynamic viscosity μ for a Newtonian fluid is allowed to depend on the thermodynamic state but not on the velocity field, which means the fluid is uniform and μ can be considered as constant.

If a more specific equation is required, according to COMSOL CFD brochure [6]:

$$\rho(\frac{\partial \boldsymbol{u}}{\partial t} + (\boldsymbol{u} \cdot \nabla)\boldsymbol{u}) = \nabla \cdot [\underset{(2)}{-p\boldsymbol{I}} + \underset{(3)}{\tau}] + \underset{(4)}{\boldsymbol{F}} \qquad\qquad 2\text{-}4$$
$$\underset{(1)}{}$$

where $\boldsymbol{u}$ represents velocity, p represents pressure, ρ represents density, $\boldsymbol{I}$ is the identity matrix and τ is the viscous stress tensor. The different terms correspond to (1) inertial force, (2) pressure force, (3) viscous force and (4) the external force $\boldsymbol{F}$ applied to the fluid.

In 3D model, the gradient of velocity $\nabla \boldsymbol{u}$ is a second-order tensor. It is represented by a 3×3 matrix:

$$\boldsymbol{L} = (\nabla \boldsymbol{u})^T = \begin{pmatrix} \dfrac{\partial u_x}{\partial x} & \dfrac{\partial u_y}{\partial x} & \dfrac{\partial u_z}{\partial x} \\[2mm] \dfrac{\partial u_x}{\partial y} & \dfrac{\partial u_y}{\partial y} & \dfrac{\partial u_x}{\partial y} \\[2mm] \dfrac{\partial u_x}{\partial z} & \dfrac{\partial u_y}{\partial z} & \dfrac{\partial u_z}{\partial z} \end{pmatrix}$$

L can be divided into two matrices $\boldsymbol{S}$, $\boldsymbol{W}$ and $\boldsymbol{L} = \boldsymbol{S} + \boldsymbol{W}$. $\boldsymbol{W}$ is called the spin tensor and $\boldsymbol{S}$ is called the strain rate tensor. These two matrixes can be represented by $\nabla \boldsymbol{u}$:

$$\boldsymbol{S} = \frac{1}{2}(\boldsymbol{L} + \boldsymbol{L}^T) = \frac{1}{2}((\nabla \boldsymbol{u})^T + \nabla \boldsymbol{u}), \qquad \boldsymbol{W} = \frac{1}{2}(\boldsymbol{L} + \boldsymbol{L}^T) = \frac{1}{2}((\nabla \boldsymbol{u})^T - \nabla \boldsymbol{u}) \qquad 2\text{-}5$$

Strain-rate tensor $\boldsymbol{S}$ describes the changing rate of the deformation of a material and $\boldsymbol{W}$ describes the rate of rotation [7]. The equation eq. 2-6 derived by Stokes [8] describes the linear relationship between $\boldsymbol{S}$ and τ:

$$\tau = 2\mu \boldsymbol{S} - \frac{2}{3}\mu(\nabla \cdot \boldsymbol{u})\boldsymbol{I} = \mu(\nabla \boldsymbol{u} + (\nabla \boldsymbol{u})^T) - \frac{2}{3}\mu(\nabla \cdot \boldsymbol{u})\boldsymbol{I} \qquad\qquad 2\text{-}6$$

One thing should be emphasized that this linear relationship is only suitable for Newtonian fluid. After replacing τ by $\mu(\nabla \boldsymbol{u} + (\nabla \boldsymbol{u})^T) - \frac{2}{3}\mu(\nabla \cdot \boldsymbol{u})\boldsymbol{I}$, the full Navier-stokes equation for a compressible fluid can be derived：

$$\rho(\frac{\partial \boldsymbol{u}}{\partial t} + (\boldsymbol{u} \cdot \nabla)\boldsymbol{u}) = \underset{(2)}{-\nabla p} + \nabla \cdot (\mu(\nabla \boldsymbol{u} + (\nabla \boldsymbol{u})^T) - \frac{2}{3}\mu(\nabla \cdot \boldsymbol{u})\boldsymbol{I}) + \underset{(4)}{\boldsymbol{F}} \qquad 2\text{-}7$$
$$\underset{(1)}{} \qquad\qquad\qquad\qquad\qquad \underset{(3)}{}$$

To solve nature convection problem, it normally requires three equations to represent the conservation of mass, momentum and energy. The Navier-Stokes equation is the momentum equation. The continuity equation to represent the conservation of mass is shown as below:

$$\frac{\partial \rho}{\partial t} + \nabla \cdot (\rho \boldsymbol{u}) = 0 \qquad\qquad 2\text{-}8$$

The energy equation (which represents the conservation of energy) evaluates the fluid temperature in different location when the temperature and pressure distribution is not homogenous.

$$\rho C_P \frac{\partial T}{\partial t} + \rho C_P \boldsymbol{u} \cdot \nabla T + \nabla \cdot \boldsymbol{q} = 0, \qquad \boldsymbol{q} = -k\nabla T \qquad\qquad 2\text{-}9$$

The energy equation is necessary especially when the material properties are temperature and pressure-dependent.

2.3 Boussinesq Approximation

2.3.1 Derivation of equation applied in COMSOL

The Boussinesq approximation is a method to address nonisothermal flow problem, such as Natural Convection Flow (NCF) without solving the full compressible formulation of Navier-Stokes equations. The density is assumed as constant ρ_0 in the temporal and convection terms and the only effect of density variation $\Delta\rho$ is in the gravitational term (the buoyancy force term). This assumption is tolerable when density variation $\Delta\rho$ is small enough since in the entire flow the buoyancy force term dominates compared to the temporal and convection terms (which are only influential for a relatively small Mach number). The Boussinesq approximation neglects the influence of $\Delta\rho$ in all terms in Navier-Stokes equations except the buoyancy force term to reduce the nonlinearity of equations. Generally, Boussinesq approximation is valid only when $\Delta\rho \ll \rho_0$ and this method is suitable for cases such as temperature changes of water within 2^oC or of air within 15^oC.

According to definition above, in Boussinesq approximation, the original continuity and momentum (Navier-Stokes) equations can be converted to:

$$\begin{cases} \underbrace{\frac{\partial(\rho_0 + \Delta\rho)}{\partial t}}_{(temporal)} + \underbrace{\nabla \cdot ((\rho_0 + \Delta\rho)\boldsymbol{u})}_{(convection)} = 0 \\ \underbrace{\frac{\partial(\rho_0 + \Delta\rho)\boldsymbol{u}}{\partial t}}_{(temporal)} + \underbrace{\nabla \cdot ((\rho_0 + \Delta\rho)\boldsymbol{uu})}_{(convection)} = -\nabla p + \nabla \cdot (\mu(\nabla\boldsymbol{u} + (\nabla\boldsymbol{u})^T) - \frac{2}{3}\mu(\nabla \cdot \boldsymbol{u})\boldsymbol{I}) + \underbrace{\rho\boldsymbol{g}}_{(Bouyancy)} \end{cases} \qquad \text{2-10}$$

In Boussinesq approximation, the density is treated as constant ρ_0 in the temporal and convection term ($\rho \approx \rho_0$) and it is assumed that the only influenced term due to density changes is in the buoyancy term (gravitational term):

$$\underbrace{\frac{\partial\rho_0}{\partial t}}_{(temporal)} + \rho_0 \underbrace{(\nabla \cdot \boldsymbol{u})}_{(convection)} = 0 \longrightarrow \underbrace{\frac{1}{\rho_0}\frac{\partial\rho_0}{\partial t}}_{(temporal)} + \underbrace{\nabla \cdot \boldsymbol{u}}_{(convection)} = 0 \longrightarrow \underbrace{\nabla \cdot \boldsymbol{u} = 0}_{(Approximation)}$$

$$\rho_0(\underbrace{\frac{\partial\boldsymbol{u}}{\partial t}}_{(temporal)} + \underbrace{(\boldsymbol{u} \cdot \nabla)\boldsymbol{u}}_{(convection)}) = -\nabla p + \nabla \cdot (\mu(\nabla\boldsymbol{u} + (\nabla\boldsymbol{u})^T) - \frac{2}{3}\mu(\nabla \cdot \boldsymbol{u})\boldsymbol{I}) + \underbrace{\rho\boldsymbol{g}}_{(Bouyancy)}$$

It can be seen, after Boussinesq approximation, all $\rho_0 + \Delta\rho$ have been replaced by a constant value ρ_0 except in the buoyancy force term $\boldsymbol{F} = \rho\boldsymbol{g}$. In continuity equation, $\frac{1}{\rho_0}\frac{\partial\rho_0}{\partial t} = 0$ and the original continuity equation $\frac{1}{\rho_0}\frac{\partial\rho_0}{\partial t} + \nabla \cdot \boldsymbol{u} = 0$ can be reduced to the incompressible form $\nabla \cdot u = 0$. It follows that $-\frac{2}{3}\mu(\nabla \cdot u)I = 0$. The momentum and continuity equations become:

$$\rho_0(\frac{\partial\boldsymbol{u}}{\partial t} + \boldsymbol{u} \cdot \nabla\boldsymbol{u}) = -\nabla p + \nabla \cdot (\mu(\nabla\boldsymbol{u} + (\nabla\boldsymbol{u})^T)) + \rho\boldsymbol{g}, \qquad \nabla \cdot \boldsymbol{u} = 0 \qquad \text{2-11}$$

The viscosity μ is normally assumed as constant and the diffusion term $\nabla \cdot (\mu(\nabla u + (\nabla u)^T))$ can thus be simplified as $\mu\nabla^2\boldsymbol{u}$. To remove density from the buoyancy term, $\rho\boldsymbol{g}$ can be replaced by $(\rho_0 + \Delta\rho)g$ to yield:

$$\rho_0(\frac{\partial\boldsymbol{u}}{\partial t} + \boldsymbol{u} \cdot \nabla\boldsymbol{u}) = -\nabla p + \mu\nabla^2\boldsymbol{u} + (\rho_0 + \Delta\rho)\boldsymbol{g} \qquad \text{2-12}$$

An increase in temperature (at constant pressure) normally causes a decrease in pressure, which means $\Delta\rho$ can be considered negative. A new variable "coefficient of thermal expansion" β needs to be introduced. The coefficient of thermal expansion β is defined as :

$$\beta = \frac{1}{\rho_0}(\frac{\partial\rho}{\partial T})_P \qquad \text{2-13}$$

After linear approximation:

$$\beta = \frac{1}{\rho_0}\left(\frac{\partial \rho}{\partial T}\right)_P \approx -\frac{1}{\rho_0}\frac{\rho - \rho_0}{T - T_0} = -\frac{1}{\rho_0}\frac{\Delta\rho}{T - T_0} \rightarrow \rho \approx \rho_0[1 - \beta(T - T_0)]$$

<div align="right">2-14</div>

T_0 is the reference temperature. The original buoyancy term can then be changed to: $\Delta\rho g = (\rho - \rho_0)g = -\rho_0\beta(T - T_0)g$. Eq. 2-12 becomes:

$$\rho_0(\underbrace{\frac{\partial \boldsymbol{u}}{\partial t}}_{\text{(temporal)}} + \underbrace{\boldsymbol{u} \cdot \nabla \boldsymbol{u}}_{\text{(convection)}}) = -\nabla p + \mu\nabla^2\boldsymbol{u} + \underbrace{(1 - \beta(T - T_0))\rho_0\boldsymbol{g}}_{\text{(Bouyancy)}}$$

<div align="right">2-15</div>

or

$$\underbrace{\frac{\partial \boldsymbol{u}}{\partial t}}_{\text{(temporal)}} + \underbrace{\boldsymbol{u} \cdot \nabla \boldsymbol{u}}_{\text{(convection)}} = -\frac{1}{\rho_0}\nabla p + \frac{\mu}{\rho_0}\nabla^2\boldsymbol{u} + \underbrace{[1 - \beta(T - T_0)]\boldsymbol{g}}_{\text{(Bouyancy)}}$$

<div align="right">2-16</div>

It has to be reemphasized that Boussinesq approximation is valid only when $\Delta\rho \ll \rho_0$. In COMSOL, to avoid possible round-off errors in the calculation of buoyancy force term, $-\nabla p + \rho_0\boldsymbol{g}$ is often written as $-\nabla P$ and $P = p + \rho_0 gh$ (where h represents the elevation). The change from p to P can be referred to as a pressure shift. In this condition, the incompressible equation eq. 2-15 can be rewritten as:

$$\rho_0\left(\frac{\partial \boldsymbol{u}}{\partial t} + \boldsymbol{u} \cdot \nabla \boldsymbol{u}\right) = (-\nabla p + \rho_0\boldsymbol{g}) + \mu\nabla^2\boldsymbol{u} - \beta(T - T_0)\rho_0\boldsymbol{g} = -\nabla P + \mu\nabla^2\boldsymbol{u} - \rho_0\boldsymbol{g}\beta\Delta T$$

<div align="right">2-17</div>

2.3.2 Efficiency of different approaches

In COMSOL, by using the ideal gas approximation, the coefficient of thermal expansion β can be computed as $\beta = \frac{1}{T_0}$. The oringial equation eq 2-17 can be written as:

$$\rho_0\left(\frac{\partial \boldsymbol{u}}{\partial t} + \boldsymbol{u} \cdot \nabla \boldsymbol{u}\right) = -\nabla P + \mu\nabla^2\boldsymbol{u} - \rho_0\frac{(T - T_0)}{T_0}\boldsymbol{g}$$

<div align="right">2-18</div>

The time cost of running simulation with three different forms of Navier-Stokes equations is tested in COMSOL [9], the three forms are listed below in descending order according to the time cost:

- Using Boussinesq Approximation with pressure shift:

$$\rho_0\left(\frac{\partial \boldsymbol{u}}{\partial t} + \boldsymbol{u} \cdot \nabla \boldsymbol{u}\right) = -\nabla P + \mu\nabla^2\boldsymbol{u} - \rho_0\frac{(T - T_0)}{T_0}\boldsymbol{g}, \qquad P = p + \rho_0 gh$$

<div align="right">2-19</div>

- Solving the full equation for a compressible fluid:

$$\rho(\frac{\partial \boldsymbol{u}}{\partial t} + \boldsymbol{u} \cdot \nabla \boldsymbol{u}) = -\nabla p + \nabla \cdot (\mu(\nabla \boldsymbol{u} + (\nabla \boldsymbol{u})^T) - \frac{2}{3}\mu(\nabla \cdot \boldsymbol{u})\boldsymbol{I}) + \rho\boldsymbol{g}$$

<div align="right">2-20</div>

- Solving the full equation for a compressible fluid with pressure shift:

$$\rho\left(\frac{\partial \boldsymbol{u}}{\partial t} + \boldsymbol{u} \cdot \nabla \boldsymbol{u}\right) = -\nabla P + \nabla \cdot \left(\mu(\nabla \boldsymbol{u} + (\nabla \boldsymbol{u})^T) - \frac{2}{3}\mu(\nabla \cdot \boldsymbol{u})\boldsymbol{I}\right) + (\rho - \rho_0)\boldsymbol{g}$$

<div align="right">2-21</div>

The result shows that Boussinesq approximation truly reduce the computation perfromance request and save simulation time in dimensionless model cases. However, for the scenario case analysed in this project, there is no real benefits considering the computational time for applying Boussinesq approximation in COMSOL. The reason is because this approximation method works only when the nonlinearity of equation is tiny (i.e. the flow is incompressible). In COMSOL, it is still recommended to solve full Navier-Stokes equations. Only in the case that fluid flow acceleration is not salient, Boussinesq

approximation simplifiy the computation by considering constant density and viscosity. Hence, in this project, Boussinesq approximation is only applied in dimensionless model analysis.

2.4 Flow Compressibility

2.4.1 Compressible flow

In compressible flow, considerable variation can happen (when Mach number>0.3) in fluid density when the temperature or pressure changes. The flow motion can be either turbulent or laminar. The coupling between $\boldsymbol{u}$, p and T is strong. The simulation is implemented by joint solution of full momentum, continuity and energy equations, which are eq. 2-7, eq. 2-8 and eq. 2-9.

Generally compressible flow analysis is appliable for liquid or gas with temperature and pressure dependent density ρ. Since the flow is compressible, not only in the buoyancy force term, but also the parameter ρ appears in the temporal derivative and in the convection term. Hence, Boussinesq approximation is not recommend in this situation and the full compressible formulation of Navier-Stokes equation should be applied instead as the momentum equation. The compressible Navier-Stokes equation is highly nonlinear (which corresponds to the turbulent flow case).

2.4.2 Weakly compressible flow

The equations used in this case are the same as those for compressinle flow. The only difference is that the density ρ is a function independent of pressure change, such as water density, which material properties are mainly temperature dependent. For instance, the natural flow of cold water (5^0C) in room temperature (15^0C) can be considered as weakly compressible flow. In COMSOL, after the weakly compressible flow option is chosen, the density ρ is calculated based on constant reference pressure P_0.

2.4.3 Incompressible flow

A single phase fluid can be considered incompressible if the temperature variation is small or the mass number (Ma) is low enough. The medium density ρ is assumed as constant ρ_0 and the continuity equation $\frac{\partial \rho}{\partial t} + \nabla \cdot (\rho \boldsymbol{u}) = 0$ can be reduced to $\nabla \cdot \boldsymbol{u} = 0$, which has been deduced in Section 2.3.1. A vector field whose divergence is zero is called a passive or tubular field. In fluid mechanics, a fluid with zero density divergence is called incompressible fluid, which means the amount of fluid flowing into a nano-volume element is equal to that flowing out of the nano-volume element at single nano time interval. This assumption is appliable for most liquids and even for some gases at low velocities [10]. In COMSOL, the medium density function is checked before simulation in case it is dependent of other quantities (e.g. concentration field).

The incompressible flow removes time-differential term for density from the continuity equation (which means density ρ is a constant):

$$\nabla \cdot \boldsymbol{u} = 0$$

2-22

And the Navier-Stokes equation can be simplified as:

$$\rho(\frac{\partial \boldsymbol{u}}{\partial t} + \boldsymbol{u} \cdot \nabla \boldsymbol{u}) = -\nabla p + \nabla \cdot (\mu(\nabla \boldsymbol{u} + (\nabla \boldsymbol{u})^T)) + \boldsymbol{F}$$

2-23

2.5 Annular Space between Horizontal Cylinders

2.5.1 Dimensionless quantities

The dimensionless quantities used in this project are shown as below. The value of these parameters can be used to evaluate the intensity of natural convection and judge if the flow is turbulent or laminar. The parameters like T_i, T_o and D_i are well explained in the Nomenclature section in the beginning of this thesis.

1. Nusselt number (Nu) is the ratio between the convective heat transfer coefficient h in flow fluid and the conductive heat transfer coefficient k in a hypothetically motionless fluid:

$$\text{Nu} \equiv \frac{h}{\frac{k}{L}} = \frac{hL}{k} \qquad \qquad 2\text{-}24$$

   L is the characteristic length of geometry structure. For instance, the characteristic length of concentric cylinder geometry is $L = \frac{D_o - D_i}{2}$ [11]. For complex shapes, L can be considered as the ratio between the body volume and the surface area of the geometry.

   In fluid dynamics, convection includes advection (fluid motion) and diffusion (conduction). Rayleigh number (Ra) is strongly associated with Nu. Convection is a combination of diffusion and advection. Diffusion occurs in stationary fluid (e.g. dye in the water). Advection occurs when there is a fluid motion. "Nu=1" represents that heat transfers by "pure conduction" in stationary fluid [12]. A value in range 1-10 describes the state of laminar flow [13]. Usually when analyzing the turbulent flow, the value of corresponding Nu can be 100 or even higher.

2. Prandtl number (Pr) represents a ratio of viscous diffusivity (kinematic viscosity) to thermal diffusivity.

$$\text{Pr} \equiv \frac{\text{momentum diffusivity}}{\text{thermal diffusivity}} \equiv \frac{c_p \mu}{k} = \frac{v}{\propto} \qquad \qquad 2\text{-}25$$

   The thermal diffusivity $\propto$ dominates in fluid motion (e.g. most types of gases) when $\text{Pr} << 1$ while the momentum diffusivity v dominates the behavior (e.g. liquid like water, oil) with large values ($\text{Pr} >> 1$). Heat dissipates quickly in liquid metal while slowly in oils. For instance, the Prandtl number of liquid mercury is around 0.015, which indicates that heat conduction dominates the behavior. Oppositely, convection is more leading for engine oil to transfer energy compared to pure conduction and therefore heat convection is dominant. Therefore, the high temperature layer of liquid metal is much thinner compared to that of oil. For most gases, $\text{Pr} \approx 1$, which shows both momentum and heat dissipate through the fluid at an approximate rate.

3. Grashof number (Gr) is mainly used to analyze the buoyancy effect

$$Gr = \frac{\rho^2 \beta g (T_i - T_o) L^3}{\mu^2} = \frac{\beta g (T_i - T_o) L^3}{v^2} = \frac{\text{buoyancy force}}{\text{viscous force}} \qquad \qquad 2\text{-}26$$

   Grashof number (Gr) reflects the influence of the cavity size to the fluid motion. For instance, for a single cylinder, the characteristic length $L = D_i$ while for an annulus $L = \frac{D_o - D_i}{2}$. It is obvious that in the same temperature difference condition, the convection in smaller cavity should be much more active than that in a larger cavity. Gr is usually evaluated together with Reynolds number [14] for a comparison. Gr can also be used to judge laminar/turbulent flow. (usually 10^9 associated with the transition to turbulence)

4. Rayleigh number (Ra) is the product of Grashof and Prandtl number. Due to density difference in the fluid, buoyancy force promotes the fluid motion and natural convection happens. Ra can be considered as a ratio of gravitational potential energy to the energy of viscous dissipation and thermal diffusion [15]. Equation eq. 2-27 and eq. 2-28 show two equation forms of Rayleigh number.

$$Ra_L = Pr * Gr \equiv \frac{c_p \mu}{k} * \frac{\rho^2 \beta g(T_i - T_o)L^3}{\mu^2} = \frac{c_p \rho^2 g\beta}{k \mu}(T_i - T_o)L^3 \qquad \text{2-27}$$

$$Ra_L = Pr * Gr \equiv \frac{v}{\propto} * \frac{\beta g(T_i - T_o)L^3}{v^2} = \frac{g\beta}{v \propto}(T_i - T_o)L^3 \qquad \text{2-28}$$

5. Reynolds number (Re) correlates well with flow characteristics. Re is a dimensionless quantity to measure how turbulent the flow is and describe the ratio of inertial force to viscous force, which was defined by Reynolds' experiment. In his experiment, dye was added into a tube with flowing water. In laminar flow regime, the dye flow maintained the pattern and moves synchronously with water. In turbulent flow regime, the dye spread out and mixed with water. In transitional case, the phenomena in the previous two regimes were both detected. The turbulent flow mainly focuses on the center while the laminar flow focuses on the boundary of the tube. For pipe flow, Reynolds number is defined as below:

$$Re = \frac{\rho u_{avg} L}{\mu} = \frac{u_{avg} L}{v} = \frac{\text{inertial force}}{\text{viscous force}} \qquad \text{2-29}$$

The u_{avg} represents the average fluid speed times. The inertial force drives the fluid to move and forms vortices or waves. The flow can be turbulent or chaotic if the inertial force is too large. The viscous force resists the movement of flow and as a result reduce the influence of inertial force. The natural convection of fluid with high viscosity is usually stable in low velocity.

The flow states can be divided into three main different types according to the value of Re:
- Laminar: predictable and mix slowly (Re<2100), viscous force dominates.
- Turbulent: unpredictable, rapid mixing (Re>4000), inertial force dominates.
- Transitional: turbulent outbursts (2100< Re<4000), a mixture of two forces exist.

The value of Reynolds numbers should be checked before simulation. The value determines whether the system is laminar, turbulent or transitional. Normally, the pipe flow with Re < 2100 is laminar flow (also known as viscous flow and linear flow) state, while the pipe flow with Re greater than 4000 is turbulent flow (also known as turbulence and turbulence) state. The pipe flow with Re between 2100 and 4000 is transitional flow.

6. Mach number (Ma) corresponds to the ratio of fluid velocity u to the speed of sound c in that fluid, which helps evaluate which mode (incompressible, weakly compressible or compressible) to choose to analyze the fluid motion.

2.5.2 Annular space between horizontal concentric cylinders

The flow generated between isothermal concentric horizontal cylinder at different temperature (T_i and T_o) has feature similar to the circulation in an enclosure heated from the side [1]. Due to temperature difference, the fluid near the inner cylinder is heated first and become less dense. The heated fluid rises due to buoyancy force until touching the outer cylinder boundary. Afterwards, the hot fluid moves along the boundary of outer cylinder, which forms a higher velocity and a higher temperature layer, until touches the cold fluid in the bottom region. The mixture fluid rises again due to buoyancy force and forms the symmetric vortices. As illustrated in Figure 2-1, two counterrotating kidney-shaped vortices form about the vertical plane in the laminar regime. The vortices are symmetric with regard to the annulus centre.
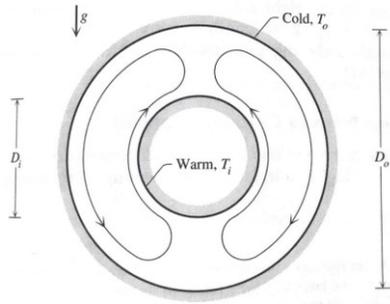
Figure 2-1: The path of laminar flow in the annulus [1].
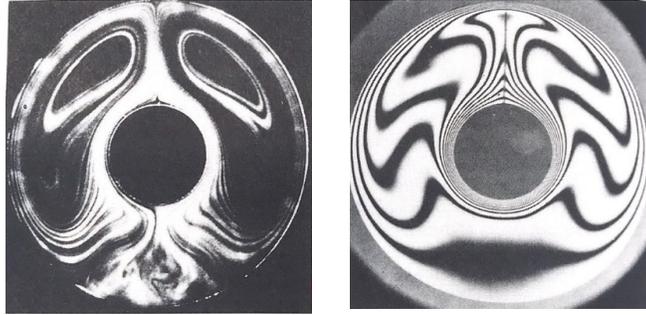
Figure 2-2: Experimental result of natural convection in the annulus (a) streamline pattern; (b) isotherms pattern [1].

Figure 2-2 (a) shows the flow pattern (streamlines) visualized with cigarette smoke. The interferometer photograph in Figure 2-2 (b) illustrates the temperature field or isotherms. The role of vertical dimension in this case can be played by either D_o or D_i, which depends on the annulus size. When $D_i < \frac{D_o}{2}$, the total heat transfer rate q' is more determined by D_i rather than D_o. The assumption above ia confirmed by the interpretation of a correlation developed in [16]:

$$q' \cong \frac{2.425k(T_i - T_o)}{\left(1 + \left(\frac{D_i}{D_o}\right)^{\frac{3}{5}}\right)^{\frac{5}{4}}} \left(\frac{PrRa_{D_i}}{0.861 + Pr}\right)^{\frac{1}{4}} \qquad \text{2-30}$$

where q' represents overall heat transfer rate between concentric cylinders per unit length in the longitudinal direction normal to the plane in Figure 2-1. The Rayleigh number Ra_{D_i} is calculated based on the film temperature $\frac{T_i + T_o}{2}$ and characteristic length D_i, $Ra_{D_i} = \frac{g\beta(T_i - T_o)D_i^3}{\alpha v}$. According to [16], Eq 2-30 agrees within $\pm 10\%$ of experimental data at moderate (laminar regime) Rayleigh numbers Ra_{D_i} as high as 10^7. The low Rayleigh number limit of the validity of Eq 2-30 occurs when:

$$D_o Ra_{D_o}^{-\frac{1}{4}} > D_o - D_i \qquad \text{2-31}$$

When the Rayleigh number (Ra_{D_o}) is small enough so that the inequality 2-31 is satisfied, the heat is transferred mainly by conduction. Instead of 2-30, a more suitable will be:

$$q = \frac{2\pi kl}{\ln\left(\left(\frac{r_i}{r_o}\right)\right)}(T_i - T_o) = h(T_i - T_o) \qquad \text{2-32}$$

$$q' = q'' * y, \qquad q = q' * z$$

$\dot{q}$: volumetric heat transfer rate in unit space (SI units: W/m^3)

q': heat transfer rate per unit length in the longitudinal direction normal to the transverse plane. (SI units: W/m)

q'': the wall heat flux averaged from $y = 0$ to y_{max} in the transverse plane. (SI units: W/m^2)

q : heat transfer rate (W)

y, z : the length in the transverse direction and in the longitudinal direction

An alternative to increase accuracy to make sure Ra_{D_o} is large enough is to calculate q' twice using 2-30 and 2-32. The larger of the two q' values is retained. This method relies on a conclusion that the true heat transfer rate q' should not be smaller than that in the pure conduction regime. The physical properties on the right- side of eq. 2-30 are evaluated at the average temperature $\frac{(T_i + T_o)}{2}$. To make it more appliable for natural convection analysis in different regimes (laminar and turbulent), Kuehn and Goldstein [11] developed further correlation equations for horizontal cylinders.

3 COMSOL ACCURACY VERIFICATION

This chapter applies the benchmark method in [3] to account for the buoyancy flow in free fluids. Temperature variation changes the density of fluid (e.g. water in heated pipes). The buoyancy flow is formed due to temperature change (which causes the density variation of fluid). All the simulations in this thesis are implemented to validate the modelling accuracy in COMSOL. The classical benchmark method is used to analyse the natural convection process in unit space. The result in COMSOL shows good agreement with that obtained by Fusegi [17] and Yang [18].

In Section 3.2 and 3.3, the movement of buoyant flow in a 2D differentially heated square cavity and in a 3D differentially heated cubical enclosure is analysed. By setting buoyancy force with dimensionless parameters, a general solution can be derived efficiently. A "volume force" term, which represents the buoyant-driven force, is set in COMSOL to couple the "Laminar flow" and the "Heat transfer in solids and fluids" modules. Temperature distributions and convective flow patterns due to variations in fluid properties, cavity size and temperature drops are exported and discussed.

Note: Boussinesq approximation function in nonisothermal flow module in COMSOL can only be chosen when the fluid is chosen as incompressible flow in the laminar flow module, otherwise it is not appliable for the other two types of flow (compressible and weakly compressible flow).

3.1 COMSOL Setting

3.1.1 Mesh setting

COMSOL Multiphysics is a general-purpose simulation software. This software can be used for modelling physical processes for engineering and scientific research. With this software, cases regarding to electromagnetics, structural mechanics, fluid flow, heat transfer and chemical engineering can be simulated. One significant step in the simulation, which will be explained in detail below, is how to build the mesh.

The mesh setting is considered after the geometry is built and the boundary conditions are assigned to different part. The mesh setting plays an instrumental role in how to analyse and solve the model. The influenced parameters include the time it takes for a computation to be completed, the amount of memory it requires to compute and the accuracy of the solution. The element size ranges from extremely fine to extremely coarse. It should be considered carefully which mesh size to be set.

3.1.2 Boundary condition

The momentum, continunity and energy equations are usually solved together with extra boundary conditions, such as isothermal layers, thermal-insulated walls and pressure point constraint to predict the temperature distribution and fluid velocity in the given model. Due to the high nonlinearity of the equations, only a limited number of analytical solutions can be derived. Hence, the accuracy of natural convection analysis in COMSOL maintains at high level for relatively simple geometries such as flow between paralled plates or concenctric cylinders. For more complex geometries, optimized boundary conditions should be set appropriately.

For turbulent flow, since small vortices or eddies might form in the flow, extremely fine mesh should be used. The Table I − IV in [19] shows that high Rayleigh number solutions are useless with coarse mesh. Finer and adjustable meshes are compulsory to main accuracy of solutions with high Ra value. It is important to pick the appropriate turbulence model since the primary condition of saving simulation time is to set correct boundary conditions.

Inlet: This boundary condition is used when a external flow is entered through the boundary into the analysed domain. An "outlet" condition should be set simultaneously when using "inlet". Usually, if inlet boundary is used to set the pressure, then

the outlet boundary should be used to set the velocity. Defining inlets or outlets simultaneously on both ends of the domain is not suggested since it might cause convergence difficulties.

Pressure point constraint: In COMSOL, for a cavity, a fixed pressure should be defined at a point of the geometry if it is not possible to define the pressure level on a surface or in a domain. If none pressure point is defined, it means there is no basic value and position in the model to be used for the pressure drop calculation, thus there will be infinite solutions and it can hardly converge. Hence, a pressure point constraint can be added to derive a particular solution. For incompressible flow, $\rho = \rho(p_{ref}, T_{ref})$ and $\mu = \mu(p_{ref}, T_{ref})$. For weakly compressible option, the fluid properties are functions of temperature T (preferably taken from a heat transfer interface), but independent of pressure. Hence, $\rho = \rho(p_{ref}, T)$ and $\mu = \mu(p_{ref}, T)$. For the compressible flow (Ma<0.3), both p and T are used to evaluate the fluid property, $\rho = \rho(p, T)$ and $\mu = \mu(p, T)$.

Hence, in the pipeline with two open-ends in the following Section 5.2, it is not necessary to set the pressure point constraint since outlet has already set the relative pressure p_0 for the selected surface. Normally, the relative pressure p_0 means the pressure drop value. Usually an inlet (u_0) and an outlet ($p_0 = 0\ atm$) is set in many cases. Actually, if the $p_{ref} = 1\ atm$, the real pressure value in the pipe should be the $p_{ref} + p_{measured}$.

3.1.3 Model correction in cut-line selection:

The heat flux of domain can be calculated by chooseing all the boundary lines of the seleted domain. However, one thing should be noticed that the boundary heat flux calculated in COMSOL equals to the average value of heat fluxe in the domains adjacent to the boundary. For instance, for a concentric cylinder, if the temperature of the inner cylinder is set as constant, the calculated boundary heat flux between inner cylinder and outer cylinder is half of the actual value since the domain heat flux of the inner cylinder is zero.

3.1.4 Dimensionless parameter

Parameters with values at reference temperature and pressure can be used to derive the non-dimensional equations for fluid motion analysis.

$\bar{v}$ = kinematic viscosity (momentum diffusivity), $\bar{v} = \mu/\rho$, m^2/s
x = displacement in x-axis direction
y = displacement in y-axis direction
T_{ref} = reference temperature
u_{ref} = fluid velocity in x-axis direction, $u_{ref} = \bar{v}/L$
v_{ref} = fluid velocity in x-axis direction, $v_{ref} = \bar{v}/L$
p_{ref} = pressure inside cavity at reference temperature, $p_{ref} = u_{ref}\mu/L = \mu\bar{v}/L^2$

The non-dimensional parameters in the equations can be derived as followed:

$X = \frac{x}{L}; Y = \frac{y}{L};$
$U = \frac{u}{u_{ref}} = \frac{u\,L}{\bar{v}}; V = \frac{v}{v_{ref}} = \frac{v\,L}{\bar{v}}; P = \frac{p}{p_{ref}} = \frac{pL^2}{\mu\bar{v}}; \theta = \frac{T-T_{ref}}{T_H-T_{ref}} = \frac{T-T_{ref}}{\Delta T};$
$u = u_{ref}U = \frac{U\bar{v}}{L}; v = v_{ref}V = \frac{V\bar{v}}{L}; p = p_{ref}; P = \frac{P\mu\bar{v}}{L^2};$
$T = \Delta T\theta + T_{ref};$

Continuity Equation: only effective for imcompressible flow (ρ is constant except in buoyancy force term)

$$\frac{\partial u}{\partial x} + \frac{\partial v}{\partial y} = \frac{\partial \frac{\bar{v}\,U}{L}}{\partial LX} + \frac{\partial \frac{\bar{v}V}{L}}{\partial LY} = \frac{\bar{v}}{L^2}\left(\frac{\partial U}{\partial X} + \frac{\partial V}{\partial Y}\right) = 0 \longrightarrow \frac{\partial U}{\partial X} + \frac{\partial V}{\partial Y} = 0 \qquad \text{3-1}$$

Momentum equation (the pressure force is assumed only in vertical (y-axis) direction):

$$\rho\left(u\frac{\partial u}{\partial x}+v\frac{\partial v}{\partial y}\right)=-\frac{\partial p}{\partial y}+\mu\left(\frac{\partial^2 u}{\partial x^2}+\frac{\partial^2 v}{\partial y^2}\right)+F$$

$$\rho\left(u\frac{\partial u}{\partial x}+v\frac{\partial v}{\partial y}\right)=-\frac{\partial p}{\partial y}+\mu\left(\frac{\partial^2 u}{\partial x^2}+\frac{\partial^2 v}{\partial y^2}\right)+\rho g\beta(T-T_{ref})$$

$$\rho\left((\frac{\bar{v}U}{L})\frac{\partial(\frac{\bar{v}U}{L})}{\partial(LX)}+(\frac{\bar{v}V}{L})\frac{\partial(\frac{\bar{v}V}{L})}{\partial(LY)}\right)=-\frac{\partial\frac{P\mu\bar{v}}{L^2}}{\partial(LY)}+\mu\left(\frac{\partial^2(\frac{\bar{v}U}{L})}{\partial(LX)^2}+\frac{\partial^2(\frac{\bar{v}V}{L})}{\partial(LY)^2}\right)+\rho g\beta\Delta T\theta$$

$$\rho\frac{\bar{v}}{L^3}\left(U\frac{\partial U}{\partial X}+V\frac{\partial V}{\partial Y}\right)=-\frac{\mu\bar{v}}{L^3}\frac{\partial P}{\partial Y}+\frac{\mu\bar{v}}{L^3}\left(\frac{\partial^2 U}{\partial X^2}+\frac{\partial^2 V}{\partial Y^2}\right)+\rho g\beta\Delta T\theta$$

$$\rho\left(U\frac{\partial U}{\partial X}+V\frac{\partial V}{\partial Y}\right)=-\mu\frac{\partial P}{\partial Y}+\mu\left(\frac{\partial^2 U}{\partial X^2}+\frac{\partial^2 V}{\partial Y^2}\right)+\frac{\rho g\beta\Delta T\theta L^3}{\bar{v}}$$

If $\mu=k=\rho=L=1$:

$$U\frac{\partial U}{\partial X}+V\frac{\partial V}{\partial Y}=-\frac{\partial P}{\partial Y}+\frac{\partial^2 U}{\partial X^2}+\frac{\partial^2 V}{\partial Y^2}+F_y,\qquad F_y=g\beta\Delta T\theta=Gr*\theta=\frac{Ra}{Pr}*\theta \qquad\text{3-2}$$

Energy equation:

$$\rho C_p\left(u\frac{\partial T}{\partial x}+v\frac{\partial T}{\partial y}\right)=k(\frac{\partial^2 T}{\partial x^2}+\frac{\partial^2 T}{\partial y^2})$$

$$\left(\frac{\bar{v}U}{L}\right)\frac{\partial(\Delta T\theta+T_{ref})}{\partial(LX)}+\left(\frac{\bar{v}V}{L}\right)\frac{\partial(\Delta T\theta+T_{ref})}{\partial(LY)}=\frac{k}{\rho C_p}(\frac{\partial^2(\Delta T\theta+T_0)}{\partial(LX)^2}+\frac{\partial^2(\Delta T\theta+T_0)}{\partial(LY)^2})$$

$$\left(\frac{\bar{v}U}{L^2}\right)\frac{\partial(\Delta T\theta)}{\partial(X)}+\left(\frac{\bar{v}V}{L^2}\right)\frac{\partial(\Delta T\theta)}{\partial(Y)}=\frac{\propto}{L^2}(\frac{\partial^2(\Delta T\theta)}{\partial(X)^2}+\frac{\partial^2(\Delta T\theta)}{\partial(Y)^2})$$

$$\bar{v}\left(U\frac{\partial\theta}{\partial X}+V\frac{\partial\theta}{\partial Y}\right)=\propto\left(\frac{\partial^2\theta}{\partial X^2}+\frac{\partial^2\theta}{\partial Y^2}\right)\rightarrow\frac{\bar{v}}{\propto}\left(U\frac{\partial\theta}{\partial X}+V\frac{\partial\theta}{\partial Y}\right)=\left(\frac{\partial^2\theta}{\partial X^2}+\frac{\partial^2\theta}{\partial Y^2}\right)$$

Since $Pr=\frac{C_p\mu}{k}=\frac{\bar{v}}{\propto}$

$$Pr\left(U\frac{\partial\theta}{\partial X}+V\frac{\partial\theta}{\partial Y}\right)=\left(\frac{\partial^2\theta}{\partial X^2}+\frac{\partial^2\theta}{\partial Y^2}\right) \qquad\text{3-3}$$

3.2 2D square case (de Vahl Davis)

The first step to verify COMSOL simulation accuracy is to build a square 2D cavity to compare the exported result with the benchmark solutions derived by de Vahl Davis et al. [19]. The fluid fills into a square cavity with no-slip walls. The Boussinesq fluid flows freely inside the enclosure without leakage. The temperature difference between the differential heated walls causes density variation of fluid, which drives the buoyant flow. The laminar flow and heat transfer module are coupled in COMSOL. The buoyancy-driven term defines a force F in the y-axis direction (vertical direction) to represent buoyancy force.
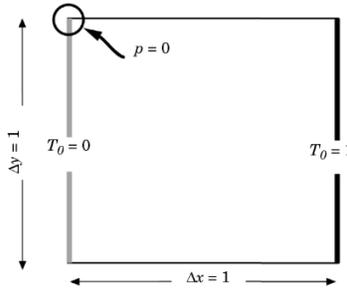
Figure 3-1: Boundary conditions in square cavity geometry

Material properties in COMSOL are set up with unit value or dimensionless parameters such as Rayleigh and Prandtl number. As shown in Figure 3-1, the temperatures are fixed at $T_C=0$ and $T_H=1$ respectively on the left and right isothermal walls, with remaining walls set as adiabatic. L is the length of a side wall and $L=1$. The fluid properties are set with unit value: $\mu=$

$k = \rho = 1$. The value of Prandtl number Pr is fixed at 0.71 and $Pr \equiv \frac{C_p \mu}{k} = \frac{v}{\propto} = C_p = 0.71$. Since $T_H - T_c = 1$, the Rayleigh number, which accounts for the ratio between buoyant and viscous forces, can be simplified as:

$$Ra = \frac{g\beta}{v \propto}(T_H - T_C)L^3 = \frac{c_p\,\rho^2 g\beta}{k\mu}(T_H - T_C)L^3 = Prg\beta \qquad \text{3-4}$$

For Rayleigh number, only value in $[10^3, 10^6]$ is analysed in this section. After using Boussinesq approximation, buoyancy term $\boldsymbol{F}$ is defined to represent the lifting force due to thermal expansion in the incompressible Navier-Stokes equations. For incompressible flow, the continunity equations is $\nabla \cdot \boldsymbol{u} = 0$. The momentum equation is:

$$\rho(\frac{\partial u}{\partial t} + \boldsymbol{u} \cdot \nabla \boldsymbol{u}) = -\nabla P + \nabla \cdot \mu(\nabla \boldsymbol{u} + (\nabla \boldsymbol{u})^T) + \boldsymbol{F} \qquad \text{3-5}$$

According to eq. 2-17,

$$\boldsymbol{F} = \underset{(Bouyancy)}{\rho g\beta \Delta T} = g\beta(T - T_c) = \left(\frac{Ra}{Pr}\right)(T - T_c) \qquad \text{3-6}$$

and eq. 3-5 can be simplified as:

$$\frac{\partial \boldsymbol{u}}{\partial t} + \boldsymbol{u} \cdot \nabla \boldsymbol{u} = -\nabla P + \mu \nabla^2 u + \left(\frac{Ra}{Pr}\right)(T - T_c) \qquad \text{3-7}$$

where $\boldsymbol{u}$ (the vector of fluid velocity) and p (pressure) are time-dependent variables. T accounts for the temperature at detected area. $\boldsymbol{g}$ denotes gravity acceleration and ρ_0 gives the reference density of medium at corresponding reference temperature T_0. μ is dynamic viscosity and β equals the coefficient of volumetric thermal expansion. The heat balance correlation is a simplified format of eq. 2-9 by using $\rho = 1$:

$$\boldsymbol{u} \cdot \nabla T - \frac{1}{C_P}\nabla \cdot (k\nabla T) = 0 \qquad \text{3-8}$$

where C_p is the specific heat capacity of the fluid. The boundary condtion of no-slip thermal insulation wall is set on the upside and downside of the cavity, which results in zero velocity on these boundaries. The refrence pressure within the domain is defined by a pressure constraint point.

Figure 3-2 and Figure 3-3 shows the isothermal contours in COMSOL modelling and in [19], which shows a similar distribution.
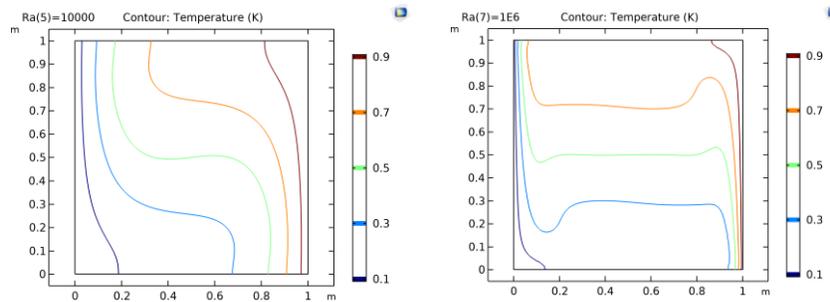
Figure 3-2: Isothermal contours in COMSOL ($T_H = 1$, $T_C = 0$) (a) $Ra = 10^4$; (b) $Ra = 10^6$
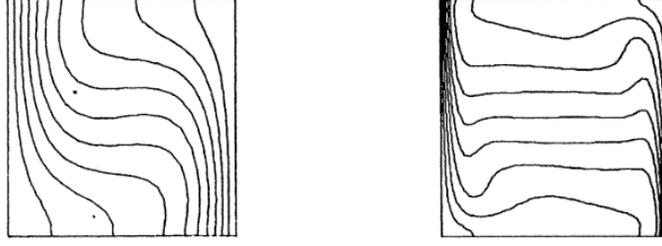
Figure 3-3: Isothermal contours from [19] (a) $Ra = 10^4$; (b) $Ra = 10^6$

It can be seen that when $Ra = 10^4$, the isothermal contour still shows a distribution similar to pure heat conductive transfer. However, when $Ra = 10^6$, the isothermal lines are rotated and become parallel with the horizontal side. The heat transfer rate can be evaluated by Nusselt numbers, which are defined as follows:

1. Maximum and minimum local Nusselt number at a fixed x-axis coordinate: Nu_{max} and Nu_{min}

2. The Nusselt number at a fixed x-axis coordinate: $Nu_x = \int_0^1 Nu_{(x,y)}\, \mathrm{d}y = \int_0^1 (\frac{dT}{dx})\, \mathrm{d}y$

3. The average value of Nusselt number throughout the cavity: $\overline{Nu} = \int_0^1 Nu_x\, \mathrm{d}x$

As suggested in [19], $Nu_{1/2}$ is easier to calculate compared with $\overline{Nu}$. The result in COMSOL is compared with that in [19] and show good agreement (with difference less than 5%).

Table 3-1: Result comparison between COMSOL and Bench mark method in [19]

	Ra			
	10^3	10^4	10^5	10^6
$Nu_{1/2}$(De Vahl. Davis)	1.118	2.243	4.519	8.799
$Nu_{1/2}$(COMSOL)	1.118	2.246	4.527	8.838
Nu_{max}(De Vahl. Davis)	1.505	3.528	7.717	17.925
Z-coordinate (De Vahl. Davis)	0.092	0.143	0.081	0.0378
Nu_{max}(COMSOL)	1.51	3.531	7.72	17.505
Z-coordinate (COMSOL)	0.094	0.146	0.08	0.0379

3.3 3D cubical case (Fugesi & Wang)

3.3.1 Setting of a three-dimensional cubical model

The analysis of natural convection flow (NCF) has wide application such as cooling of electrical equipments [20]. A study of NCF in a differentially heated cavity is implemented in [17] and [20]. The velocity in z-direction exists, although not dominant in magnitude. The simulation result is cross-checked with that of two-dimensional solutions in [19] and experimental result in [21]. At high Rayleigh number, better mesh setting is necessary to help get more accurate simulation result, which can describe clearly the dynamic features of fluid neat the boundary or at the corner [17]. The natural convection flow with high Ra requires much finer mesh near the joint edge of adjacent faces [20].
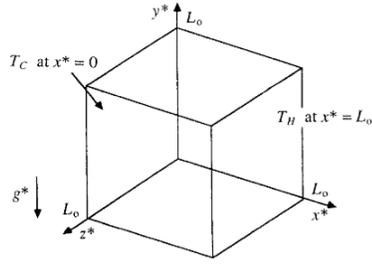
Figure 3-4: A cube with length L_o (T_H>T_C) [17]   Figure 3-5: Mesh schematic demonstration in COMSOL
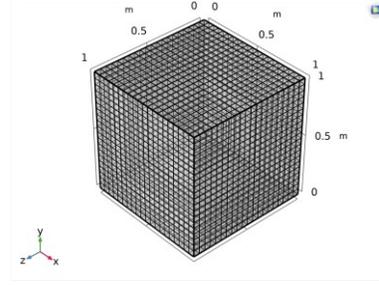
The model to study steady-state NFC in an air-filled cubical enclosure is shown in Figure 3-4. The length of the cube $L_0 = 1$ and the fluid density $\rho^* = \mu^* = k^* = 1$.The Rayleigh number Ra is defined as $Ra = \frac{g^*\beta^*c_p^*\rho^{*2}g(T_H-T_C)L_0{}^3}{\mu^*k^*} = g^*\beta^*c_p^*(T_H - T_C)$ and the value of Ra in this simulation varies from 10^3 to 10^6. The Prandtl number Pr is fixed at $Pr = \frac{c_p^*\mu^*}{k^*} = c_p^* = 0.71$. The overheat ratio $\delta = \frac{T_H-T_C}{T_0}$ is introduced to set the temperature of the isothermal layer. The temperature of the right (at $x = L_0$) and left vertical side wall (at $x = 0$) is set respectively as $T_H = \frac{2+\delta}{2}$ and $T_C = \frac{2-\delta}{2}$ ($\delta = 0.1$). The lateral walls are set as adiabatic walls. The hydrostatic pressure $p_0 = 1$ atm and the film temperature $T_0 = \frac{T_H+T_C}{2} = 1$.The Reynolds number $Re = \frac{\rho^*u_0L_0}{\mu^*} = u_0$. In this nondimensional simulation, the typical fluid velocity [17] due to buoyancy force is defined as $u_0 = \sqrt{g^*\beta^*L_0\Delta T} = [g^*\beta^*L_0(T_H - T_C)]^{\frac{1}{2}} = \sqrt{\frac{Ra}{Pr}}$. u_0 is used here as reference velocity for velocity normalization. The magnitude of velocity contour figures in COMSOL should be normalized for comparison with result in [17]. Hence, the dimensionless quantites Ra, Pr and Re are related as $Ra = Re^2Pr$ since $Re = u_0$ as derived above.

The flow field is depicted by the incompressible Navier-Stokes equations. The Boussinesq approximation is applied for the fluid properties. The viscous dissipation energy is neglected. According to equation eq. 3-6, a volum force is also set in the y-axis direction:

$$\underset{(Bouyancy)}{\boldsymbol{F} = \rho^*g^*\beta^*\Delta T} = g^*\beta^*T_0(T - T_C) = g^*\beta^*\frac{(T_H - T_C)}{\delta}(T - T_C) = \left(\frac{Ra}{Pr}\right)\frac{(T - T_c)}{\delta}$$

The boundary conditions are set as :

$$\boldsymbol{u} = 0 \text{ on all the walls}$$
$$T = \frac{2-\delta}{2} \text{ at } x = 0, T = \frac{2+\delta}{2} \text{ at } x = 1(\delta = 0.1)$$
$$\frac{\partial T}{\partial n} = 0 \text{ at } y = 0, y =, z = 0 \text{ and } z = 1$$

According to [17], the Boussinesq approximation is used in the field of buoyancy-driven flow. Results for two Rayleigh numbers $(Ra = 10^4 \text{ and } 10^6)$ are inspected.

3.3.2 Case 1: Low Rayleigh number
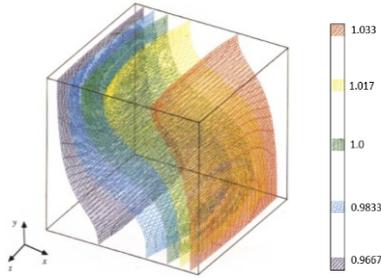
Figure 3-6: The temperature field at Ra =10^4 [17] for comparison
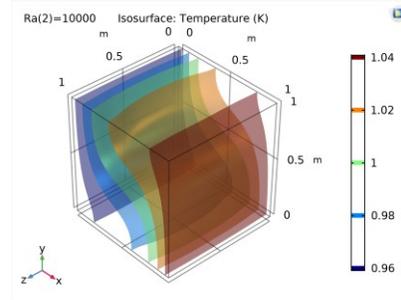
Figure 3-7: Isothermal contours in COMSOL ($T_H = \frac{2+\delta}{2}$, $T_C = \frac{2-\delta}{2}$, $\delta = 0.1$)

The distribution of isothemal layers in Figure 3-7 shows a flow field in which convection is not salient. The isothermal contours from the view of x-y plane are similar to Figure 3-2 in square cavity case. However, the difference is that, in 3D model, the variations in the z-direction are also discernible. The isothermal layers in the right half domain (0.5<z<1) is symmetric to that in the left half domain (0<z<0.5) about the plane (z=0.5). Besides, the isothermal contour on each constant x-y plane is centro-symmetric about the centre (x=0.5, y=0.5).

Figure 3-9 is representative of the iso-surface patterns of constant velocities in each direction (u, v, w). As can be deduced from Figure 3-9, the main flow, which is comprised by the velocity component u in the x-axis direction and v in the y-axis direction, focuses on the area near the isothermal walls ($x = 0$ and $x = 1$) and thermal insulation walls ($y = 0$ and $y = 1$) separately.

As shown in Figure 3-9, the u and v components of velcotiy fields in the core region is too small and can almost be ignored. Figure 3-9 (3) displays also the velocity layer distribution of component w. It can be found that the magnitude of u and v is about one-order magnitude larger than that of component w. Here, the velocities are normalized by the reference velocity: $u_0 = \sqrt{Ra/Pr} = 118.67 \approx 100$ and the normalized velocity $U = \frac{u}{u_0} = \frac{u}{\sqrt{Ra/Pr}}$.
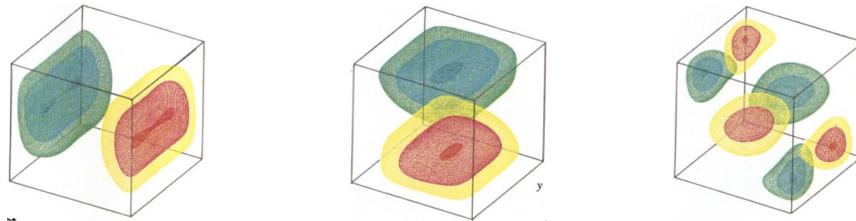
Figure 3-8: Iso-velocity contours from [17] for comparison (1) v component; (2) u component; (3) w component;
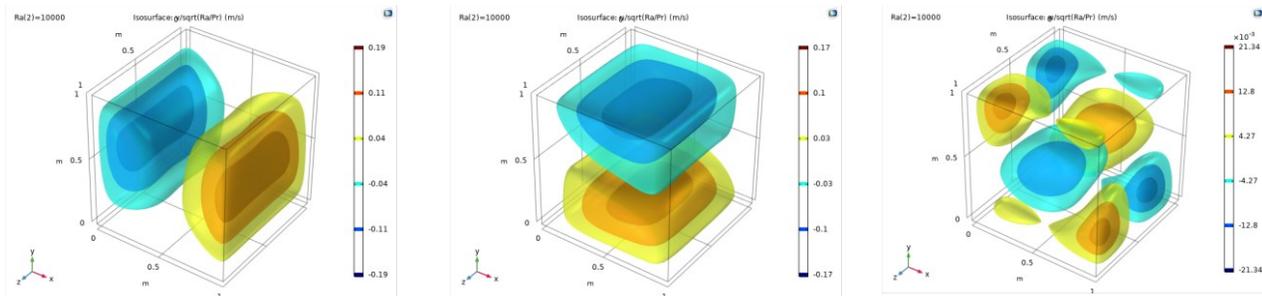
Figure 3-9: Iso-velocity contours in COMSOL at Ra =10^4 (1) v: velocity in y-axis direction (2) u: velocity in x-axis direction (3) w : velocity in z-axis direction

The gross flow field characteristics is reflected by vorticity as well. Figure 3-11 illustrates the distribution of the vorticity absolute value in COMSOL and Figure 3-10 is referred from [17] for comparison. The high vorticity layers focus mainly on the vertical isothermal walls ($x = 0$ and $x = 1$) and the horizontal walls ($y = 0$ and $y = 1$). The interior core is nearly stagnant. Figure 3-11 proves that when $Ra = 10^4$, a dominant large vortex exists in the cubical cavity, which maintains the path of natural convection flow.
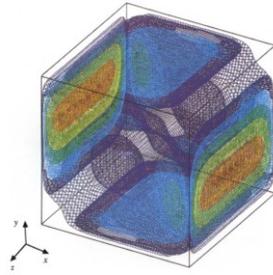
Figure 3-10: Iso-surfaces of vorticity (absolute values) at Ra =10^4 in [17] for comparison
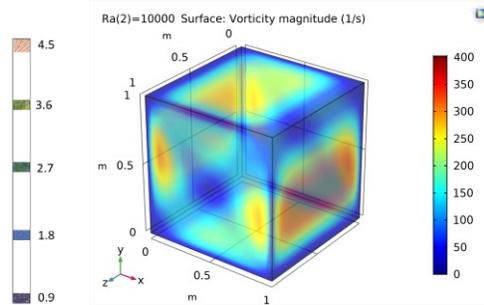
Figure 3-11: Vorticity distribution at Ra =10^4 in COMSOL ($T_H = \frac{2+\delta}{2}$, $T_C = \frac{2-\delta}{2}$, $\delta = 0.1$)

3.3.3 Case 2: High Rayleigh number

In the high Rayleigh number case ($Ra = 10^6$), a distinct isothermal layer distribution exists near the side walls (z=0 and z=1) with an almost stagnant interior core. Convection is dominant when $Ra = 10^6$. Hence, distorted isothermal layers can be observed close to the thermal insulation walls ($z = 0$ and $z = 1$). An approixmate linear temperature stratification can be observed in the core region along the x-axis direction in Figure 3-13.
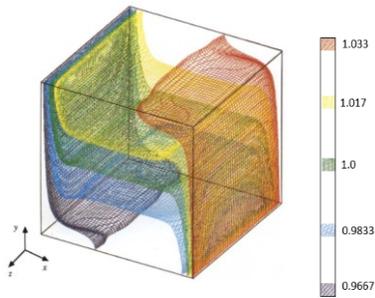
Figure 3-12: The isothermal layer when Ra =10^6 in [17] for comparison
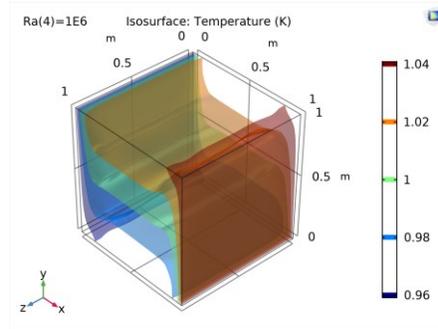
Figure 3-13: Isothermal contours in COMSOL ($T_H = \frac{2+\delta}{2}$, $T_C = \frac{2-\delta}{2}$, $\delta = 0.1$)

For the case with Ra =10^6, large velocity components (u, v) are restricted in the regions closed to the walls. The thermal and velocity layer at Ra =10^6 is much thinner compared to that at Ra =10^4. The variation of velocity in z-axis direction is conspicuous near the corners of the cavity. The magnitude of u and v component is much larger than that of the w component in z-direction [17]. Here, the velocities are normalized by the reference velocity: $u_0 = \sqrt{Ra/Pr} = 1118.78 \approx 1000$ and the normalized velocity $U = \frac{u}{u_0} = \frac{u}{\sqrt{Ra/Pr}}$.
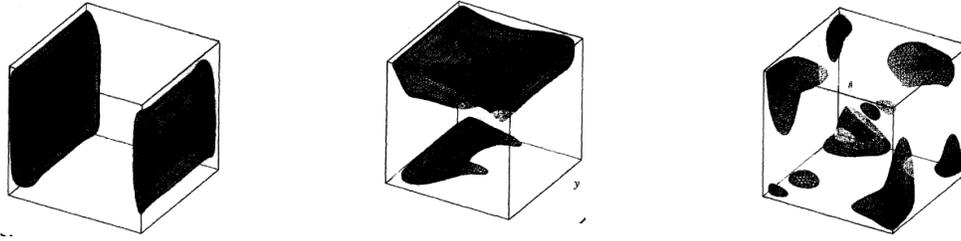
Figure 3-14: Iso-velocity contours from [17] for comparison (1) u: velocity component in x-axis direction (2) v: velocity component in y-axis direction (3) w : velocity component in z-axis direction
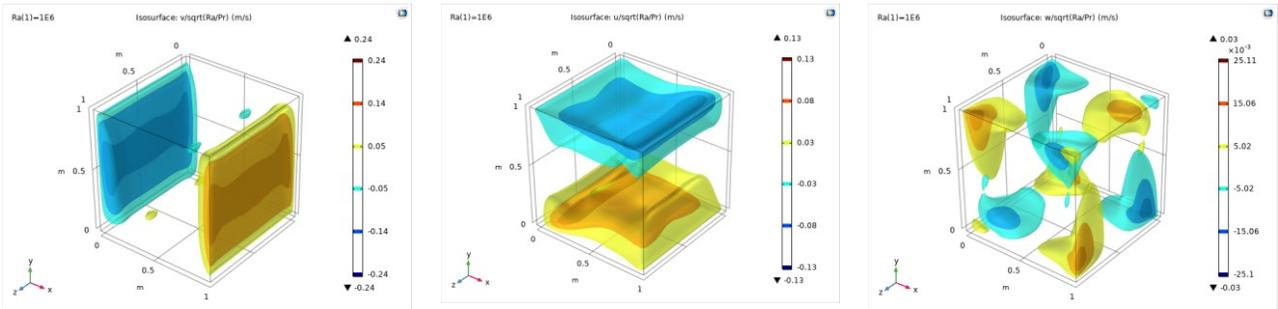

Figure 3-15: Iso-velocity contours in COMSOL at Ra $=10^6$ (1) v: velocity component in y-axis direction (2) u: velocity component in x-axis direction (3) w : velocity component in z-axis direction ($T_H = \frac{2+\delta}{2}$, $T_C = \frac{2-\delta}{2}$, $\delta = 0.1$)

Vorticity reflects the gross flow field characteristics. Figure 3-17 illustrates the comparison of the vorticity absolute value. Compared with Figure 3-11, the interior core is still nearly stagnant. The high vorticity layers only focus on the vertical isothermal walls ($x = 0$ and $x = 1$) and the area that vorticity layeres cover extend to the whole wall. The original vorticity layers close to thermal insulation walls ($y = 0$ and $y = 1$) in case Ra $=10^4$ disapper in this case with Ra $=10^6$.
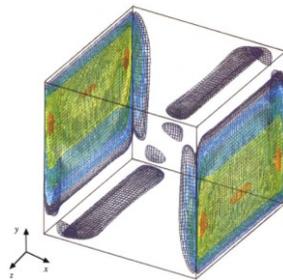
Figure 3-16: Iso-surfaces of vorticity (absolute values) at Ra $=10^6$ from [17] for comparison
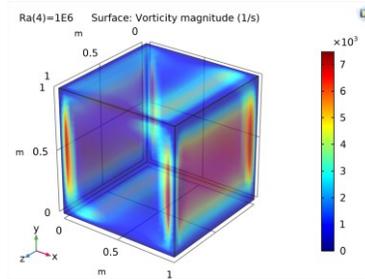
Figure 3-17: Vorticity distribution at Ra $=10^6$ in COMSOL ($T_H = (2 + \delta)/2$, $T_C = (2 - \delta)/2$, $\delta = 0.1$)

3.3.4 Convection analysis with dimensionless quantities

Nusselt number (Nu) can be used to calculate the heat dissipation rate through the vertical wall (x=1).This parameter evaluates the relative strengths between heat convective and conductive transfer process. The average Nusselt number throughout the cavity: $Nu_{mean}(z) = \int_0^1 \frac{\partial T(y,z)}{\partial x}\Big|_{x=0 \ or \ 1} \, dy = \int_0^1 Nu_{local}(y, z) \, dy$.
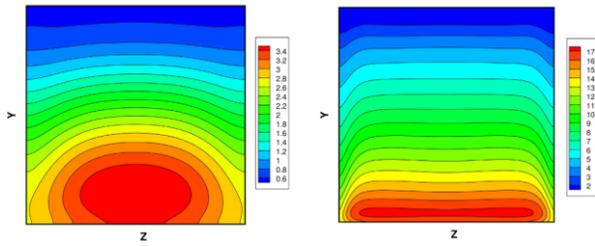
Figure 3-18: Distributions of Nu_{local} at x=1 in [20] (a) Ra $=10^4$;(b) Ra $=10^6$ from [17] for comparison
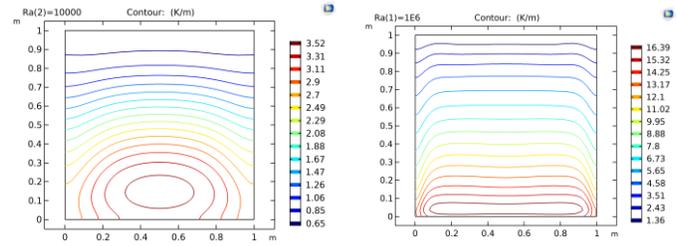
Figure 3-19: Distributions of Nu_{local} in COMSOL at x=1 (a) Ra $=10^4$;(b) Ra $=10^6$

Figure 3-19 displays variation of the local Nusselt number in COMSOL. The patterns have been compared with those from [20] [17] and the plots show similar distribution and legend. When Ra $=10^6$, the distribution of Nu_{local} illustrates noticeable prominent convection activities ($Nu_{local}>1$). Nu_{local} varies fast in the y-direction compared with z-direction (transverse direction). It can be observed that the peak value of Nu on each contour level is located at z=0.5 and the value drops in the region close to the thermal insulation walls ($y = 1$). It can be considered that the thermal insulation wall (y=1) in the cubical enclosure reduces the heat convective transfer. It is found that higher Nu_{local} always appears at the bottom region of the heated wall (x=1), which indicates a leading convection phenomenon. This is because from the view of heated wall, due to vortex rotating, the cold fluid near the bottom of enclosure is closer to the hot wall than that in the vicinity of upper region.The cold fluid near the top area of the enclosure is farther from the hot wall compared with the cold fluid close to the bottom region of the enclosure. This deduction can be reflected from isotherms plots in Figure 3-23 as well, which indicates that convection is more intensive than conduction in the bottom region.
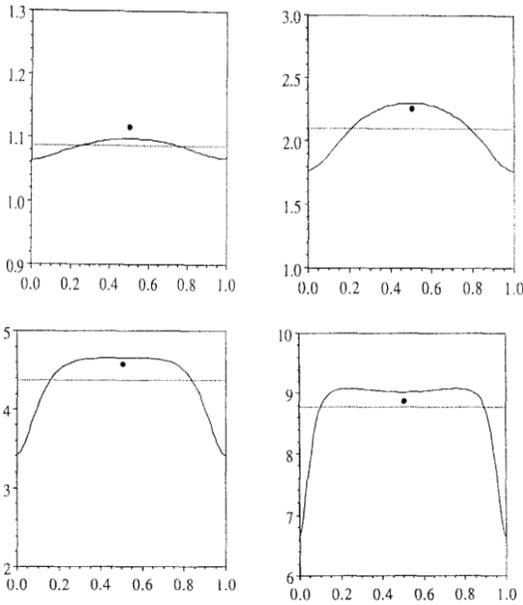
Figure 3-20: Variation of Nu_{mean} and $Nu_{overall}$ in [17] for comparison(a) Ra $=10^3$ (b) Ra $=10^4$ (c) Ra $=10^5$ (d) Ra $=10^6$
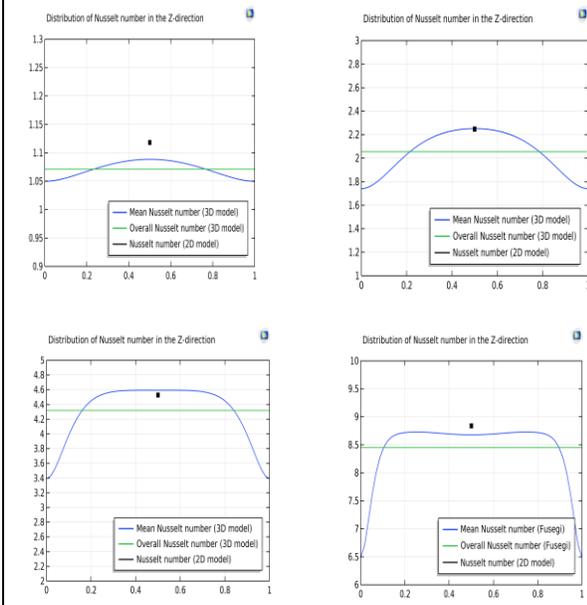
Figure 3-21: Variation of Nu_{mean} and $Nu_{overall}$ in COMSOL (a) Ra $=10^3$ (b) Ra $=10^4$ (c) Ra $=10^5$ (d) Ra $=10^6$

Figure 3-21 demonstrates the variation of Nu_{mean} along the z-axis direction. When $Ra < 10^6$, the maximum Nu_{mean} appears at $z = 0.5$. When $Ra = 10^6$, two maximum values occur at $z = 0.2, z = 0.8$ separately. This indicates a dominant convective flow at high Rayleigh number, which enhances the heat transfer. The $Nu_{overall}$ in COMSOL simulation is relatively smaller than that in [17], especially when Ra $=10^6$, even the plots still illustrates a similar profile. With higher

Rayleigh number, the plot of Nu_{mean} becomes more flat in the z-axis direction in the core region. However, no matter how high the rayleigh number is, the value of Nu_{mean} drops steeply close to the region of adiabatic walls ($z = 0$ and $z = 1$).

The isotherms on the symmetry planes in [20] are compared with results in COMSOL, which are shown as below:
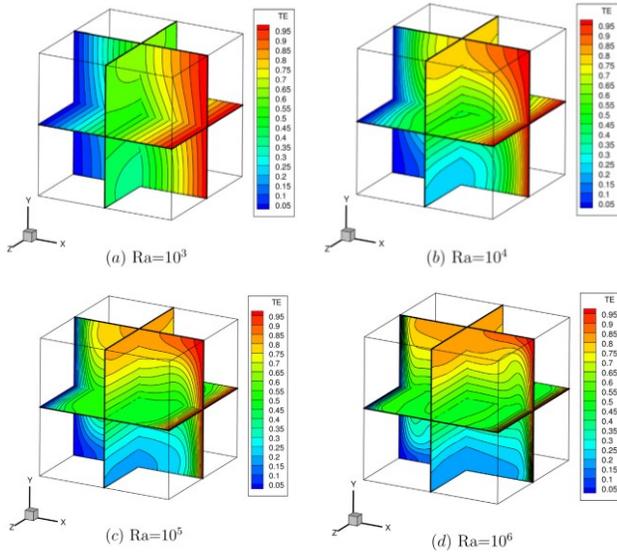
Figure 3-22: Isotherms on the symmetry planes in [20] for comparison (a) Ra =10^3 (b) Ra =10^4 (c) Ra =10^5 (d) Ra =10^6
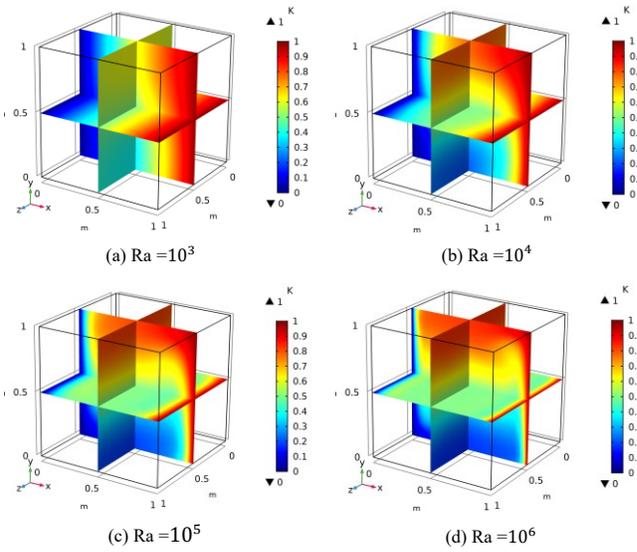
Figure 3-23: Isotherms on the symmetry planes in COMSOL (a) Ra =10^3 (b) Ra =10^4 (c) Ra =10^5 (d) Ra =10^6

Figure 3-22 and Figure 3-23 shows similar patterns. It can be seen that with the increase of Rayleigh number, the isotherms variation changes from along the horizontal direction (x-axis) to along the vertical direction (y-axis), which indicate the process of heat transfer from conduction to convection state. Besides, the thermal boundary layers are becoming thinner next to the isothermal walls with the increase of Ra, which does not appear near the adiabatic walls. The isotherm contours in [17][40] are similar to the isothermal plot at plane z=0.5 in this 3D cubical case.

Figure 3-24 and Figure 3-25 shows comparison of velocity magnitude contours in cavity between [20] and COMSOL results.
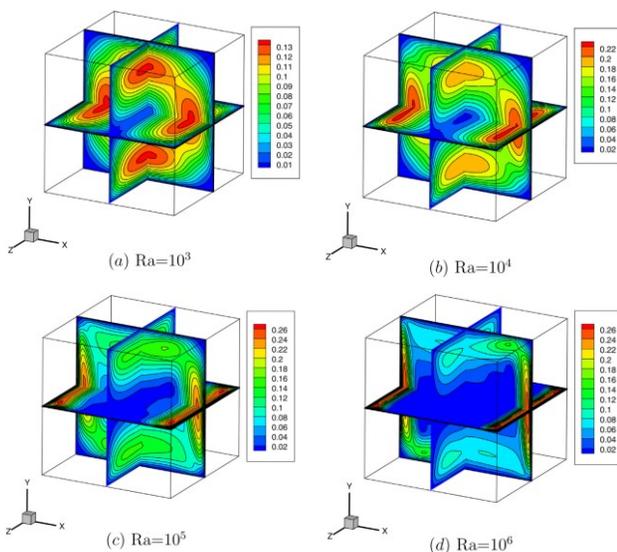
Figure 3-24: Velocity magnitude contours on the symmetric planes in [20] for comparison (a) Ra =10^3 (b) Ra =10^4 (c) Ra =10^5 (d) Ra =10^6
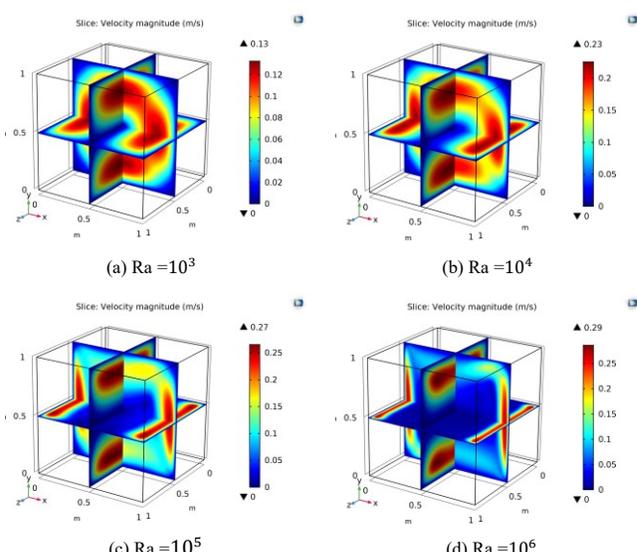
Figure 3-25: Velocity magnitude contours on the symmetric planes in COMSOL (a) Ra =10^3 (b) Ra =10^4 (c) Ra =10^5 (d) Ra =10^6

The high velocity layers are developed near the interior core of the cavity at low Rayleigh number while the layers move gradually adjacent to the isothermal walls and corners of the cavity with the increase of Ra. The thickness of velocity layer is also reduced with higher Ra value. Also, there is no apparent velocity layer formed closed to the adiabatic walls, which means that the adiabatic walls have an inhibition effect in heat transfer process.

Hence, It can be concluded that with the increase of Ra, the thermal and velocity layers gets closer to the isothermal walls. During the process, the layers become thinner due to the expansion of interior stationary space. Due to the inhibiting effect of thermal insulation walls to the natural convection, there is no obvious boundary layer forming close to these walls.

3.3.5 Comparison of temperature distribution

(a) y = 0.5 (b) x = 0.5
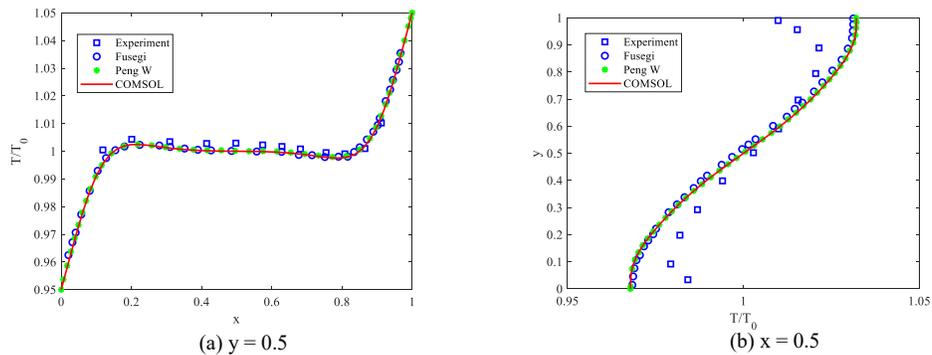
Figure 3-26: Temperature distribution at plane z=0.5 for Ra =10^5. Experimental results (Ra =$1.89 * 10^5$) in [22] and finite-difference results (Ra =10^5) in [20] and [17] are included for comparison.

The experimental results with Ra =$1.89 * 10^5$ in [22] is introduced to compare with the numerical result exported from COMSOL. It should be emphasized that one of the reason causing experimental error is due to the difficulty of achieving perfect adiabatic walls in experiments. The problem that heat transfer from supposed thermal-insulated walls is inescapable. The results from COMSOL show good agreement with those in [20] and [17] at $y = 0.5$. However, there is a noticeable difference discrepancy between experimental and three numerical results in Figure 3-26 (b) and the value deviation is salient adjacent to the vertical walls. As is mentioned before, it might because of the imperfect thermal insulation condition in real cases [22].The velocity profiles in COMSOL are compared with two sets of experimental data from [22] and [23].

(a) x = 0.5 (b) y = 0.5
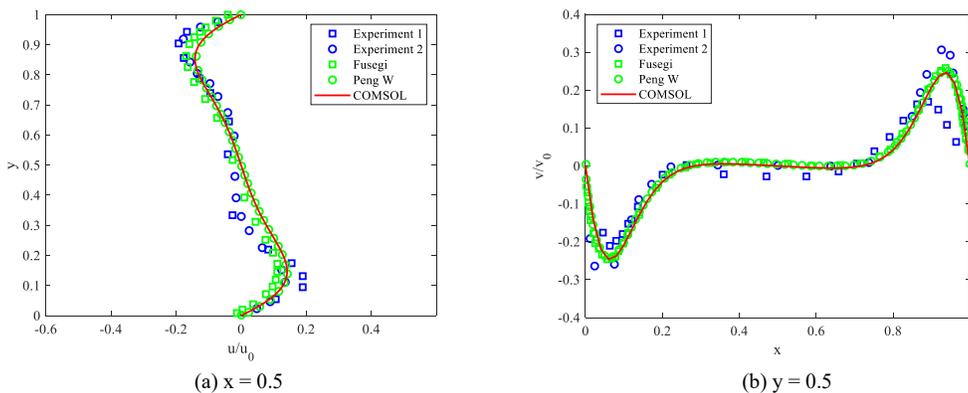
Figure 3-27: Velocity distribution at plane z=0.5 for Ra =10^5. The experimental results from (Exp1) [23] and (Exp2) [22] are compared with numerical results from Fusegi [20], Peng W [17] and COMSOL;

As shown in Figure 3-26 and Figure 3-27, the numerical result is verified by comparison with experimental data. The symbol u indicates velocity in x-axis direciton and v indicates velocity in y-axis direction. The sets of lab data measured by laser Doppler techniques (for $Ra = 1.89 * 10^5$ in [22] and $Ra = 1.03 * 10^5$ in [23]) are compared with numerical predictions.

The result of Krane and Jessee [22] agrees well with the numerical result while discrepancy exists at the peak value of v/v_0 adjacent to isothermal walls in (b), although the deviation of u/u_0 is relatively slight in (a). This may indicate intensified convection with the increase of Ra, especially near the walls compared with the interior core.
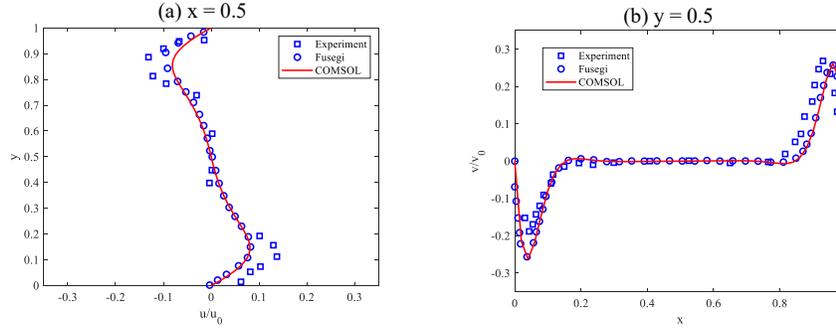
Figure 3-28: Velocity distribution at z=0.5 for $Ra = 10^6$. The experimental results from [23] with $Ra = 1.13 * 10^6$ and numerical results from Fusegi [20] are compared with exported results in COMSOL

The velocity (u) of experimental data in Figure 3-27 and Figure 3-28 indicate a region with extremely low velocities near the interior core of cavity, which is not obvious reflected in the numerical simulation. The numerical result from [17] and COMSOL shows a relatively linear curve from positive to negative peak value of velocity along the path of y-axis. The reason might because, as mentioned before, the perfect adiabatic boundary is difficult to achieve in experiment while in simulation the adiabatic walls are set as perfect thermal insulation in the absence of external physical influence.

The experimental results of Bilski et al. [23] in Figure 3-27 and Figure 3-28 show a considerable asymmetry with those of numerical predictions, even δ is small, $\delta = \frac{T_H - T_C}{T_0} = 2 * \frac{T_H - T_C}{T_H + T_C} < 0.03$. If δ is large ($\delta > 0.2$), the fluid properties might become more inhomogeneous in the geometry and it will cause larger error, which can be noticed in the later annulus case study. The asymmetry is more prominent in lower Rayleigh number case $Ra = 10^5$. The asymmetry phenomenon is not noticeable in profiles of velocity conponent u, which corresponds to the isothermal layer in the x-axis direction. Hence, it can be concluded that the external temperature has not obvious impact on the isothermal walls in the experiment.

3.4 Chapter conclusion

In conclusion, the convective forces intensify with higher Ra in the unit space. Besides, with higher Ra, the variations of velocity and thermal layer become more prominent in the horizontal direction (x-axis direction) and these layers are inclined to be constrained in thinner areas near the isothermal surface. The velocity components u and v in the x-axis and y-axis direction are noticed to be much larger than that in the z-axis direction (w) in $10^4 < Ra < 10^6$. The secondary vortices close to the vertical walls at high Rayleigh number influence the distribution of Nu_{mean}, which is shown in Figure 3-21 (d).

The $Nu_{overall}$ in cubical model is different from the value Nu_{mean} in Table 3-1 from 2D square model in COMSOL, especially noticeable in case $Ra = 10^6$. This might due to the geometry difference in the longitudinal direction betweeen 2D and 3D model. The value of Nu_{mean} and $Nu_{overall}$ in 3D COMSOL modelling is slightly lower compared to that in [17], which might be due to the mesh setting. A extremely fine mesh setting is compulsory for high Rayleigh number cases.

Generally, the 3D modelling data in COMOSL is in fair consistency with the present experimental and numerical result. The thermal insulation condition at the adiabatic walls has a considerable influence on the vertical profiles of flow variables [17]. The result accuracy of the 3D cubical model analysed in Section 3.3 has proved that COMSOL can couple heat transfer module and flow dynamic module well and shows performances as well as other computational flow dynamics (CFD) softwares such as ANSYS, FLOW-3D, PowerFLOW and OpenFOAM.

4 DIMENISONLESS MODEL

In this chapter, dimensionless models are continued to be used to observe the influence of dimensionless parameters, such as Rayleigh number and Prandtl number, to the motion of free fluid in annulus. After converting Navier-Stokes equations and energy equation to dimensionless form, a general solution can be derived to describe many relevant scenario cases.

Several papers have provided considerable discussion of concentric/eccentric cylinder model in horizontal and vertical direction. Dimensionless models are built in COMSOL based on the boundary conditions used in these papers to set boundary conditions with dimensionless parameters. Section 4.1 illustrates the plots of thermal and velocity boundary layers with different combination of Ra and Pr. In the same approach, a dimensionless vertical cylinder is built in Section 4.2 to study the relationship between radius ratio of inner/outer cylinder, height of the annulus and Ra. The exported results from COMSOL can be compared and verified with relevant papers to build an initial dimensionless model for the scenario model simulation in the following chapter. Numerical simulations are implemented with the new combination of Ra and Pr, which has not been covered in the previous papers, to make further prediction of the free fluid motion.

4.1 Horizontal Concentric Cylinders

The parameters used in this section is referred from [18]. The body force due to density change is defined by Boussinesq approximation (as derive in Section 3.2, $F = -g\beta(T - T_r)$ in y-direction. The numerical results in COMSOL and experimental results in [4] show good agreement. The natural convection is characterized by varying combination of Ra ($10^2 \le Ra_L \le 10^8$) and Pr ($0.01 \le Pr \le 100$). It was generally considered that the flow becomes gradually unstable (turbulent) with the increase of Ra_L and Pr. Plume (which is named according to the shape of ascending heated fluid) is used as a reference to judge the stability of flow. The simulation difference between this thesis and [18] is that the smoothed particle hydrodynamics (SPH) method was applied in [18], which is a mesh-free method. Since COMSOL is mesh-based simulation software, this method is not appliable and a mesh-based model is built instead for analysis.

For viscous flow with natural convection heat transfer, the continuity and momentum equations are the same as 2-7 and 2-8 seperately. Regarding to conservation of energy, the following equation is used:

$$\rho C_P \frac{\partial T}{\partial t} + \rho C_P \, \boldsymbol{u} \cdot \nabla T + \frac{1}{d_z} \nabla \cdot \boldsymbol{q} = Q + \frac{1}{d_z} q_0 + Q_p + Q_{vd}, \qquad \boldsymbol{q} = -d_z k \nabla T \tag{4-1}$$

In eq. 4-1, energy Q_p due to pressure changes and energy Q_{vd} due to viscous dissipation is ignored. Besides, there is neither heat source q_0 nor initial energy Q. Hence eq. 4-1 can be simplified as：

$$\frac{\partial T}{\partial t} + \boldsymbol{u} \cdot \nabla T - \frac{1}{\rho C_P} \nabla \cdot (k \nabla T) = 0 \tag{4-2}$$

Where temperature T, density ρ and velocity $\boldsymbol{u}$ are time-dependent variables. μ is dynamic viscosity and k is thermal conductivity of the fluid and C_P is the specific heat at constant pressure. The body force $\boldsymbol{F}^B$, which is defined according to in the negative y-direction according to the fluid density variation, is set as:

$$\boldsymbol{F}^B = \boldsymbol{g}\beta(T - T_r) \tag{4-3}$$

where $\boldsymbol{g}$ is the gravitational acceleration, β is the thermal coefficient of fluid expansion and T_r is the reference temperature.

According to the numerical model data in [18], $\frac{L}{D_i} = 0.8$, $L = 1m$, $T - T_c = \Delta T \leq 1$ ($T_h = 1$ and $T_c = 0$), $\mu = 0.001 \frac{kg}{m \cdot s}$, $k = 1 \frac{W}{m \cdot K}$, $g = 1 \frac{m}{s^2}$, $\beta = 0.05\ K^{-1}$, $C_p = \frac{k\ Pr}{\mu}$, $\rho = (\frac{Ra\ k\mu}{g\beta L^3 \Delta T c_p})^{\frac{1}{2}}$. The buoyancy force term F_y is set as $F_y = \left(\frac{Ra}{Pr}\right)(T - T_c) = \frac{\rho^2 g \beta}{\mu^2}(T_h - T_c)L^3(T - T_c) = g\beta(T - T_c)$.
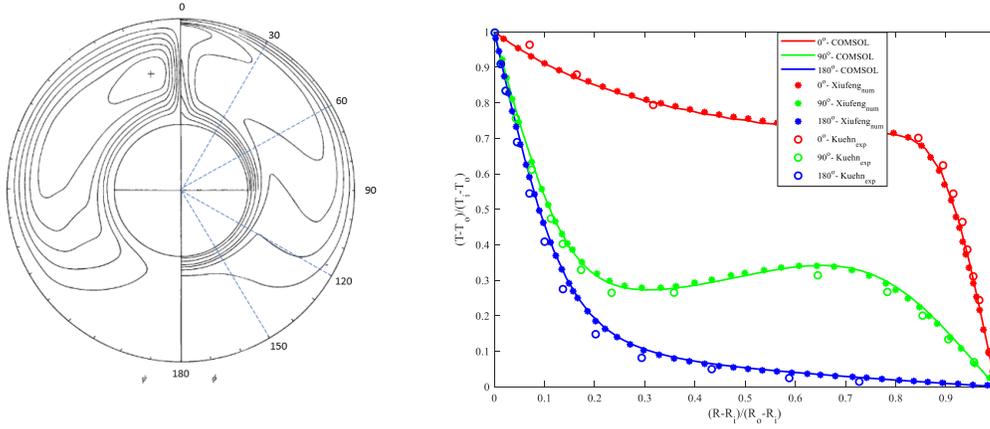
Figure 4-1: (a) Geometry illustration of cut-lines; (b) Dimensionless temperature profiles between experiment in [4], SPH simulation in [18] and COMSOL modelling ($Ra_L = 4.7 * 10^4, Pr = 0.706$)

A comparison of dimensionless temperature profiles between experiment in [4], SPH simulation in [18] and COMSOL modelling is shown in Figure 4-1, which shows good agreement.

The temperature and streamlines plots with $10^2 \leq Ra_L \leq 10^8$ and $0.01 \leq Pr \leq 10^2$ is shown in Table 4-1 and Table 4-2. Initially, the stationary model was applied but later it was found that the results always gave stable/linear result no matter the flow should actually be laminar or turbulent in the annulus. In other words, the stationary model profiles lose accuracy in turbulent state simulation. After modifying the study mode from "stationary" to "time-dependent" and set time as (0,1,1000)[s], some optimized results were exported. The exported profiles in Table 4-2 are similar to Figure 6 in [18]. A "(0,0.1,2000)[s]" time-dependent model was also tested, which did not export a much more optimized result than the first model (the relative steady-state arrives at around 400s). Hence, "(0,1,1000)[s]" is set as the simulation period to export a relative accurate but economical result in this model.

The Prandtl number is the ratio of momentum diffusivity to thermal diffusivity. The viscosity of fluid can be understood as a force to resist the fluid flow and usually it can be considered as thickness of the fluid. For instance, honey is much more thicker and difficult to flow compared with water since it has larger viscosity compared with water. However, the stress put on the fluid is independent of the viscosity. It means the fluid viscosity never changes regardless of how much stress the fluid suffers. The viscous force is benefical to the stability of fluid flow and suppress the inertial force to promote the flow into turbulent state [24]. Generally, the natural convection is suppressed by the viscous force [18].

At $Pr = 0.01$, the thermal diffusivity $\propto$ is much larger than the momentum diffusivity v. According to definition of Reynolds number eq.2-29, when momentum diffusivity v is relatively small, the trend that inertial force dominates heat transfer process while viscious force is weak becomes progressively obvious when Ra_L increases from 10^2 to 10^8. For $Pr = 0.01$, the viscosity of fluid is low and the fluid has low resistance to deformation in the annulus. For instance, in liquid mercury ($Pr = 0.015$), thermal transport is much more effective than momentum transport [25]. When $Ra_L = 10^2$, the isotherm contours are almost concentric circles, which indicates that heat conduction is significant compared to convection. However, the streamlines and velocity plots in Table 4-2 and Table 4-3 still reflect the existence of slight convection in lower part of the annulus. With Ra_L increase from 10^3 to 10^8, natural convection becomes stronger and the shape of isotherms changes. The rising flow is too quick to move along the boundary of outer cylinder in the limited space and breaks up into smaller

26

components, which causes the formation of multiple vortices. The locations of vortices are at random due to low viscosity of fluid.

There are few common fluids with Prandtl numbers in the order of 0.1 [25]. A nearest example is molten lithium at 975K (with Pr = 0.065) [26]. At Pr = 0.1, the ratio of momentum diffusivity to thermal diffusivity increases a bit compared to the case of Pr = 0.01, which changes the original conduction dominant state by forming symmetric vortices with the increase of Ra_L from 10^2 to 10^8. The velocity plots show a upward movement of vortices, which is due to the increase of Rayleigh number Ra. With larger value of Ra, buoyancy force becomes more dominant compared to viscous force, which causes heated fluid to move upwards to the top region. It is also the reason why the flow has a transitional period and transfers from turbulent (unstable) to laminar (stable) state when Ra_L increases from 10^4 to 10^5. Combined with the streamlines in Table 4-2, this phenomenon can be explained by vortex interactions. When $Ra_L = 10^5$, the rotation of each two adjacent vortices are stable since their movement directions are counter-rotating (one is clockwise while the other is counterclockwise). A plume forms between these two vortices. However, if these two adjacent vortices are co-rotating (both are clockwise or both are anticlockwise), they are in collision with each other and the conflict between them results in unstable flow. The unstable state maintains until the relative weaker vortex is eliminated due to the crash with the adjacent stronger vortex. An analogous pattern was found by Luo et al. in [27].

The prandtl numbers of most gases are about one ($Pr = 1$), which means both momentum and heat dissipate at almost the same rate through the fluid. The hot fluid rises from the hot fluid layer near the inner cylinder and forms plumes in the enclosure. Only single plume remains when $Pr = 1$. The plume rises until touches the boundary of outer cylinder. The heat convection is predominant and the plume region shrinks with the increase of Ra_L. With the increase of Ra_L from 10^2 to 10^7, both the plume width and the thickness of isothermal layers decrease. The height of vortex center rises marginally and the boundary layer of vortex profiles is getting thinner.

The case of $Pr = 10$ is similar to that of $Pr = 1$ while the region of plume shrinks faster with the change of Ra_L. An unstable plume can be found when $Ra_L = 10^7$, which indicates a turbulent flow. Seawater at room temperature is a typical example of fluid with $Pr = 10$.

For fluid with $Pr = 100$, engine oil is a common example since the main purpose of using it is to reduce friction and wear on moving parts. The high viscosity allows the flow movement to be slow and stable.

According to classification standard set in [18], the convection states can be divided accroding to the number of plumes (vortices). Only one plume forms when $1 \leq Pr \leq 10$ and $10^2 \leq Ra_L \leq 10^7$. This conclusion can be inferred further that, at low Prandtl number ($Pr = 0.01$ and $Pr = 0.1$), the high thermal diffusivity forces heat conduction to implement in low-viscosity fluid, which promotes instability of heat transfer and forms vortices.

Generally ,the flow is stable when the value of Ra_L is small and becomes turbulent with the increase of Ra_L . The transition value of Ra_L, which indicates the transitory stage from laminar to turbulent flow, varies with different Prandtl number Pr. For low Pr, the thermal diffusivity is high, which leads to asymmetry and complexity of streamline distribution. In the case with Pr $\geq$ 10, the turbulent flow occurs and focuses mainly on the top region of the annulus.

Table 4-1: Isotherms at different Prandtl and Rayleigh number

| $Pr = 0.01$ | $Pr = 0.1$ | $Pr = 1$ | $Pr = 10$ | $Pr = 100$ |

$Ra_L = 10^7$

$Ra_L = 10^6$

$Ra_L = 10^5$

$Ra_L = 10^4$

$Ra_L = 10^3$

$Ra_L = 10^2$
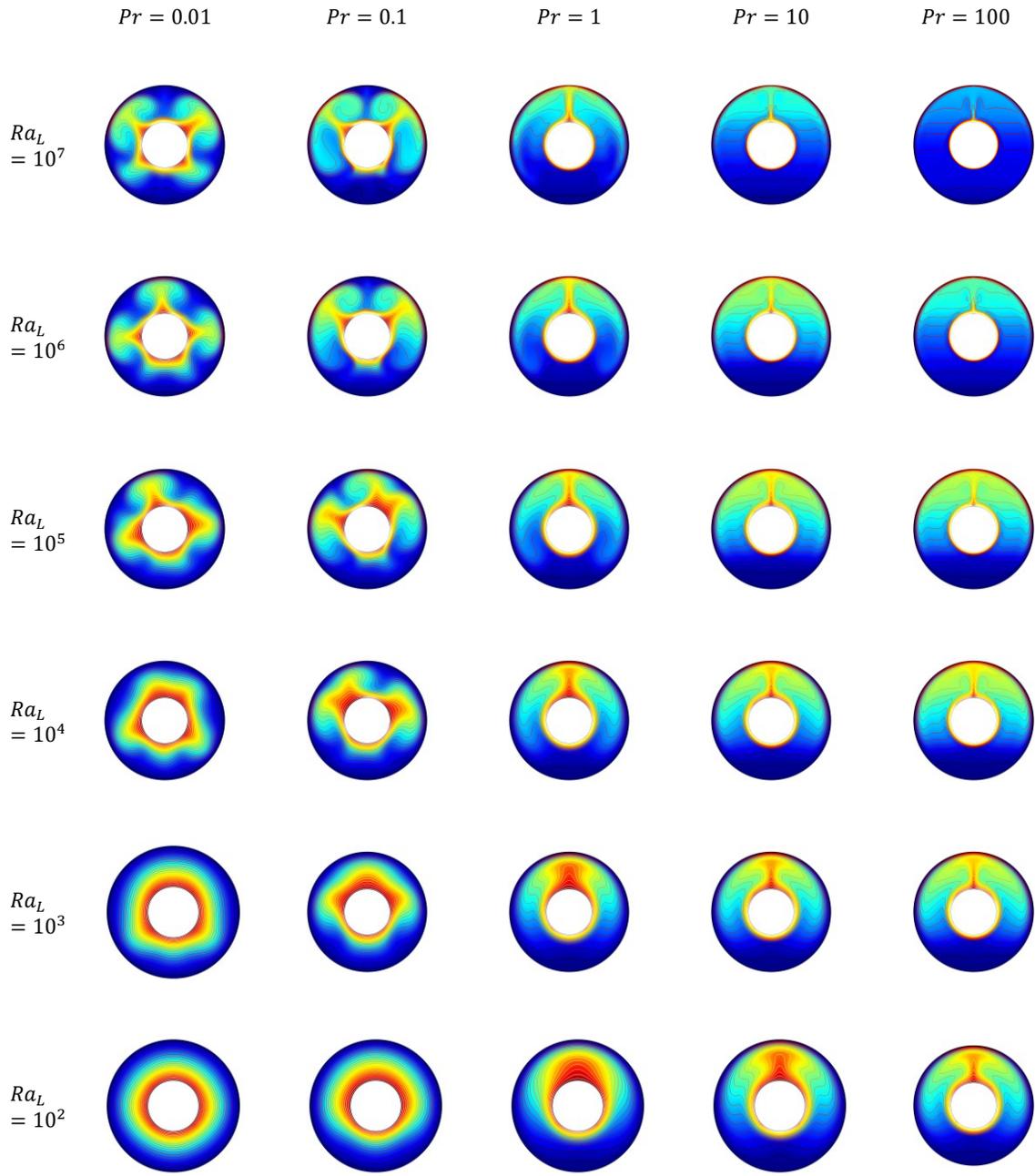
Table 4-2: Streamlines at different Prandtl and Rayleigh numbers

| $Pr = 0.01$ | $Pr = 0.1$ | $Pr = 1$ | $Pr = 10$ | $Pr = 100$ |

$Ra_L = 10^7$
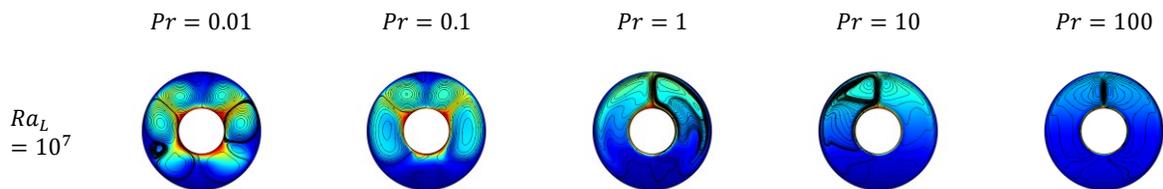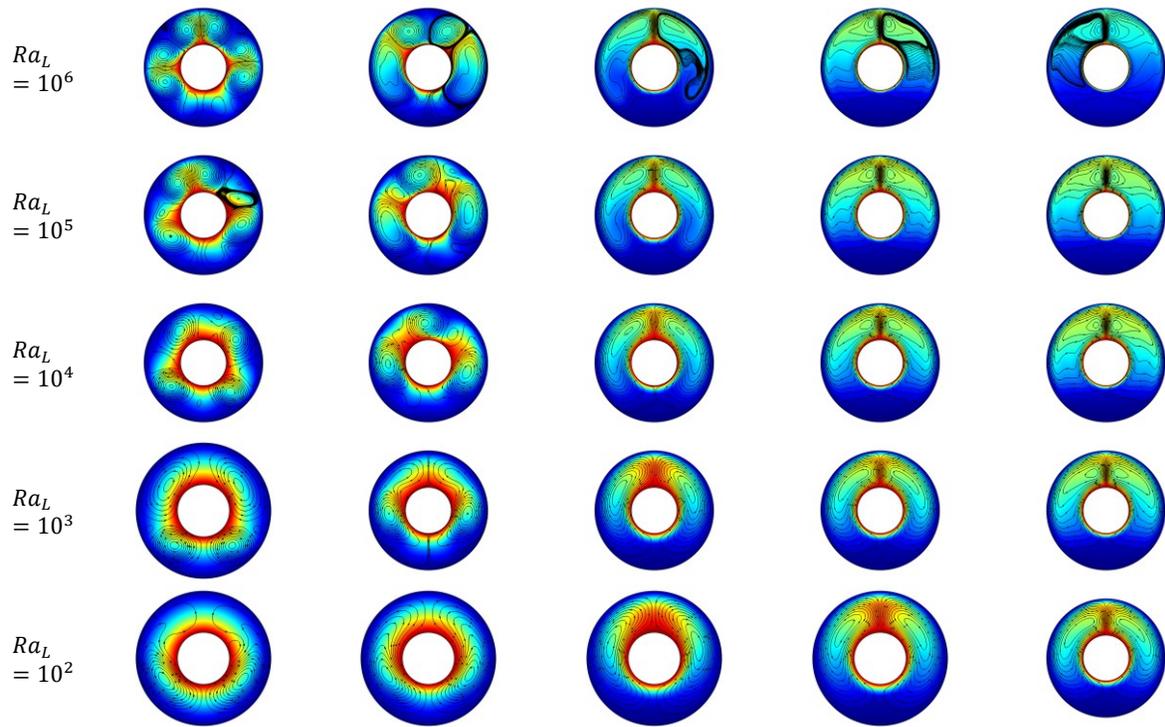
Table 4-3: Velocity at different Prandtl and Rayleigh numbers

$Ra_L = 10^3$

$Ra_L = 10^2$
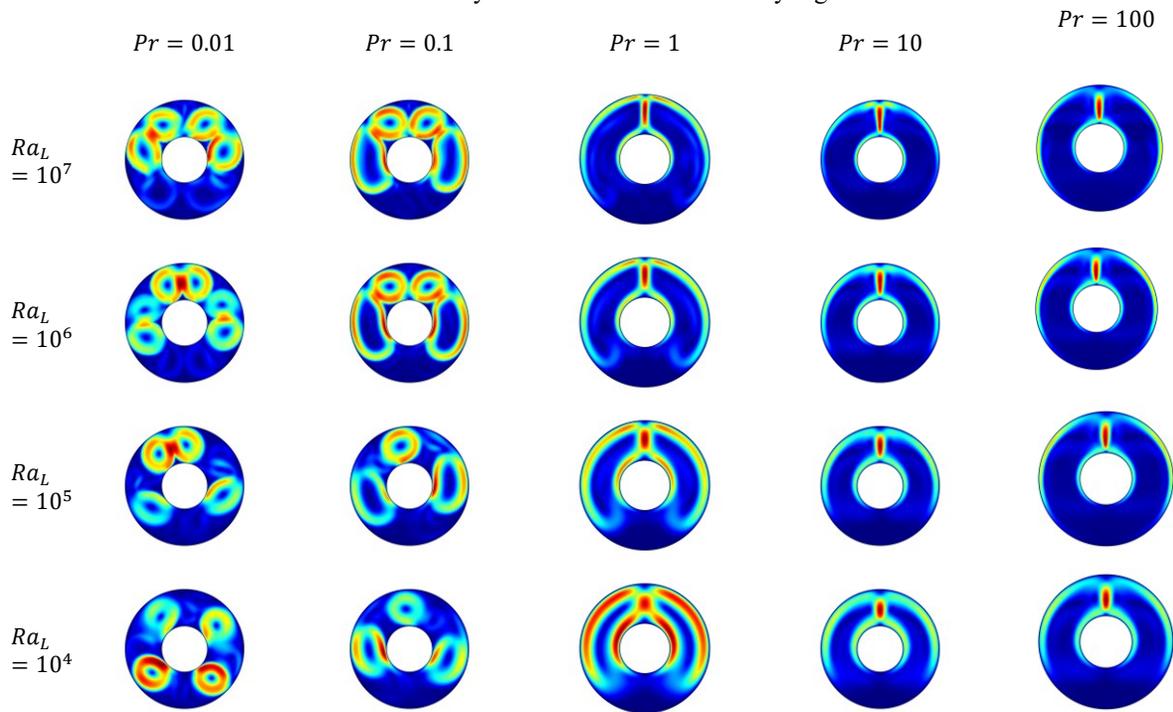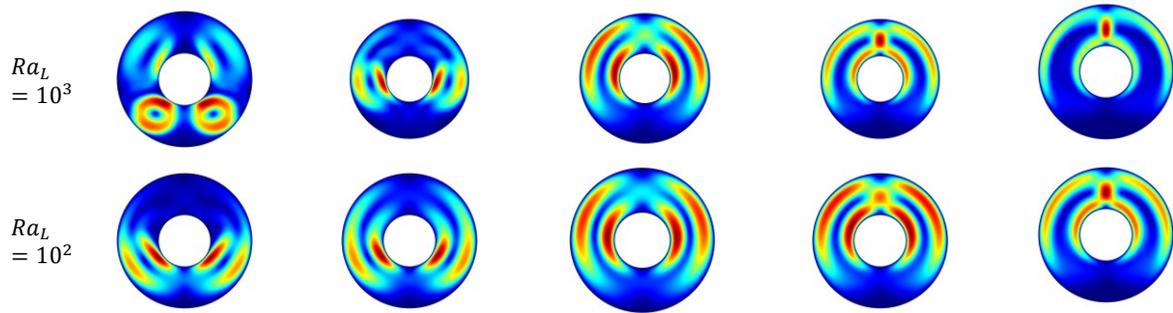
The influence of inner cylinder position should be also analysed. After setting an eccentric cylinder with an eccentricity of 0.652 and -0.623 seperately, the following tablets can be derived:

Table 4-4: Isotherms at different Prandtl and Rayleigh number (left: 0.652, right: -0.623)

| | $Pr = 0.1$ | $Pr = 1$ | $Pr = 10$ | $Pr = 0.1$ | $Pr = 1$ | $Pr = 10$ |

$Ra_L = 10^7$

$Ra_L = 10^6$

$Ra_L = 10^5$

$Ra_L = 10^4$

$Ra_L = 10^3$

$Ra_L = 10^2$
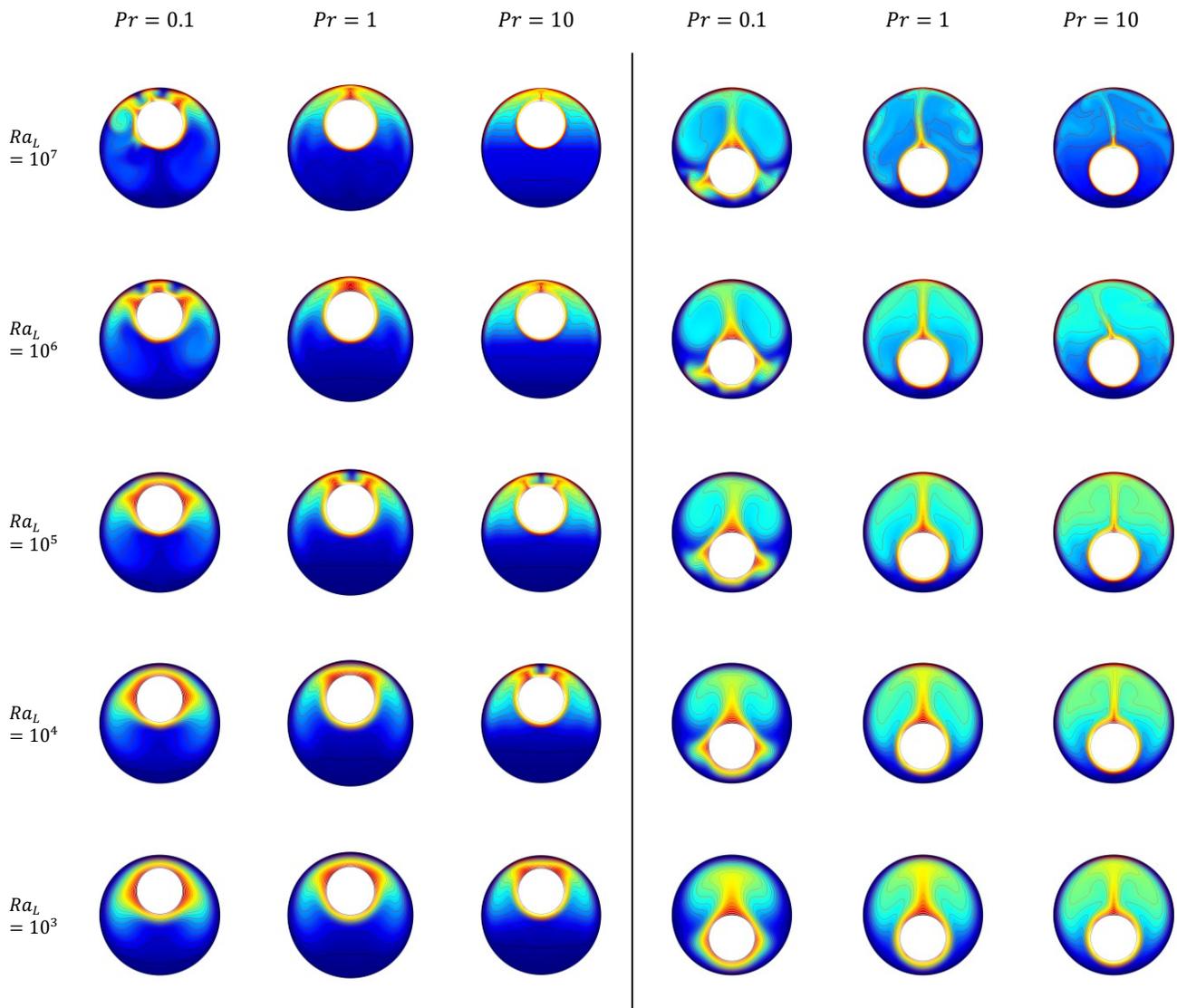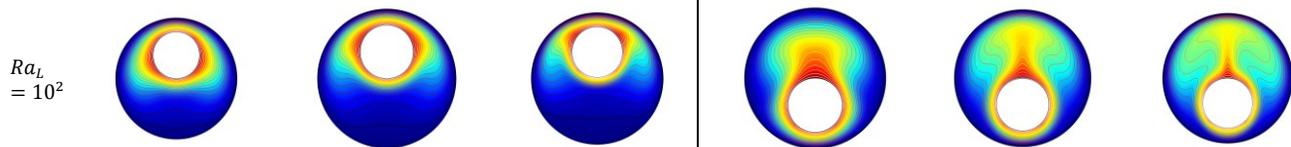
The streamlines is shown as below:

Table 4-5: Streamlines at different Prandtl and Rayleigh number (left: 0.652, right: -0.623)

| $Pr = 0.1$ | $Pr = 1$ | $Pr = 10$ | $Pr = 0.1$ | $Pr = 1$ | $Pr = 10$ |

$Ra_L = 10^7$

$Ra_L = 10^6$

$Ra_L = 10^5$

$Ra_L = 10^4$

$Ra_L = 10^3$

$Ra_L = 10^2$
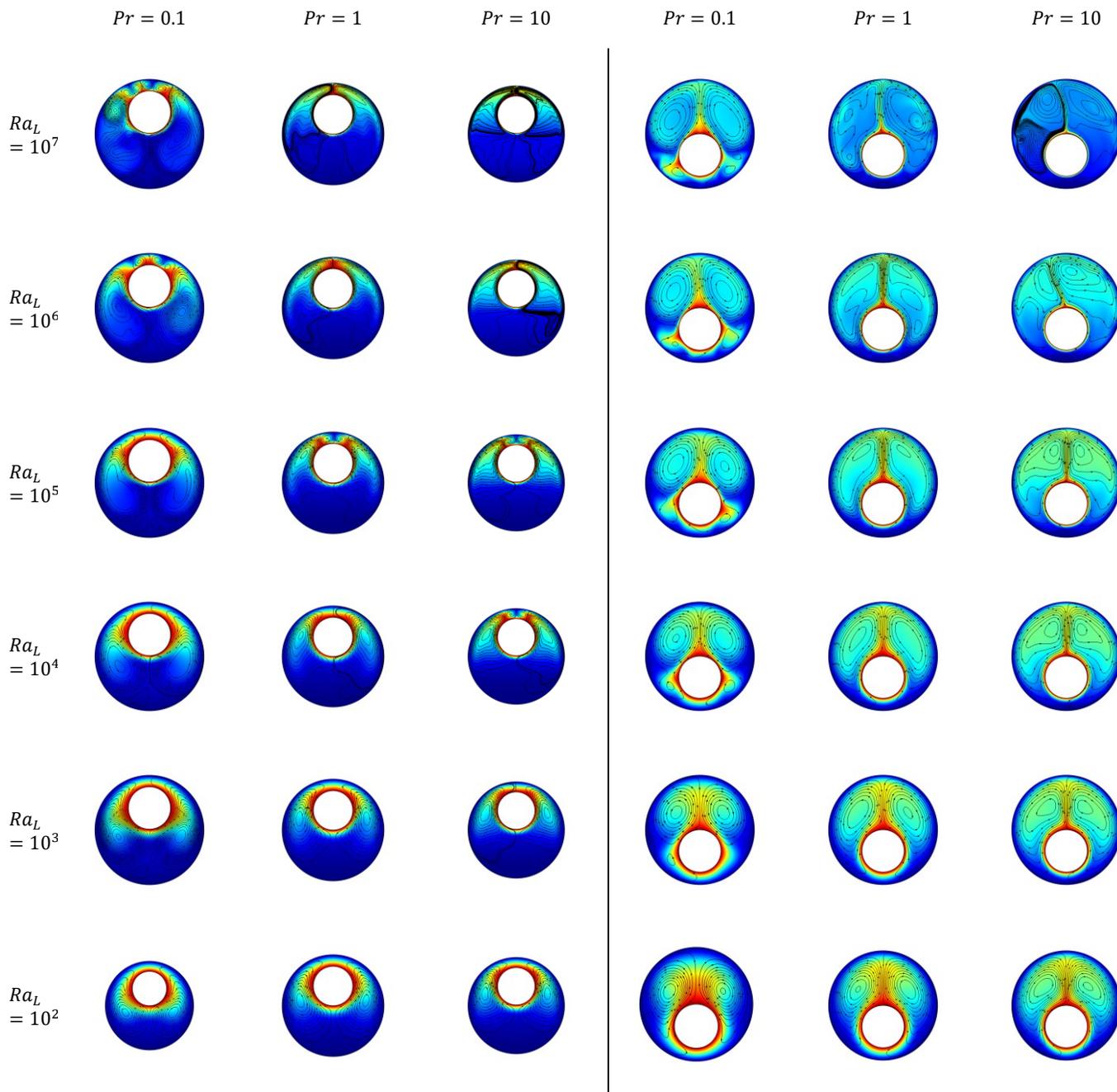
The velocity plots are shown as below:

Table 4-6: Velocity at different Prandtl and Rayleigh number (left: 0.652, right: -0.623)

	$Pr = 0.1$	$Pr = 1$	$Pr = 10$	$Pr = 0.1$	$Pr = 1$	$Pr = 10$
$Ra_L = 10^7$						
$Ra_L = 10^6$						
$Ra_L = 10^5$						
$Ra_L = 10^4$						
$Ra_L = 10^3$						
$Ra_L = 10^2$						
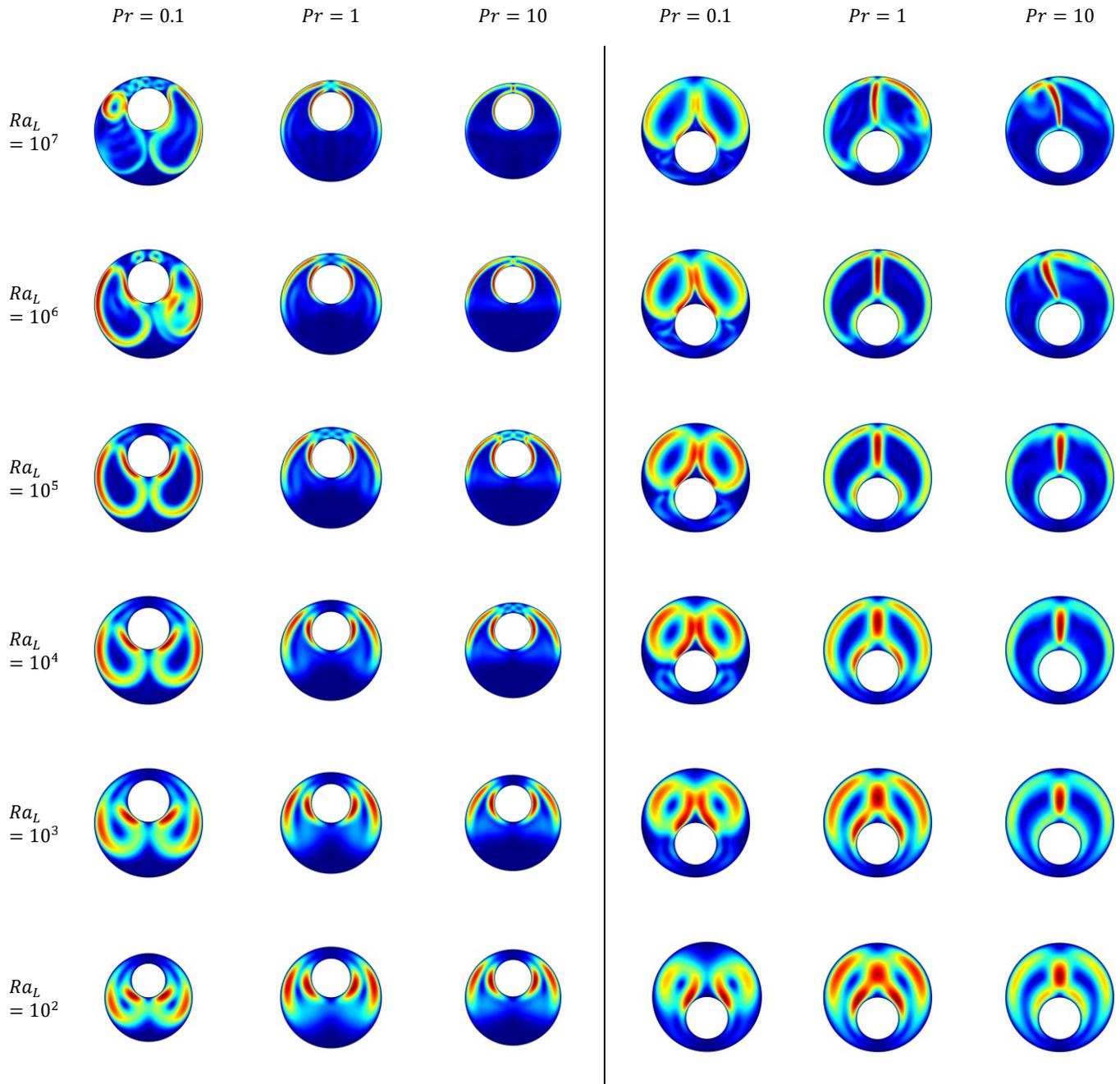
4.2 Vertical Concentric Cylinders

The dimensionless model of concentric cylinders is built in vertical direction to observe the temperature and velocity distribution. The thermal boundary conditions in COMSOL are as follows. The temperature is set as unit one on the vertical

32

boundary of inner cylinder while it is set as zero on that of outer cylinder. The horizontal top and bottom walls are set as adiabatic. Boussinesq approximation is used and the density is considered as constant in Navier-stokes equations except in the buoyancy froce term (the density is temperature dependent).

The analysis focuses on the free convection in a vertical annulus with $\Pr = 1$, radius ratio $2 \leq \frac{R_o}{R_i} \leq 4$ and aspect ratio $5 \leq K \leq 15$, $K = \frac{H}{R_o - R_i}$. The results are shown by laminar axisymmetric flow plots. The height of the cylinder is scaled down for plotting convenience. The figures of streamlines are as follows:

Table 4-7: Streamlines with different Rayleigh number and cavity size

	$\frac{R_o}{R_i} = 2$		$\frac{R_o}{R_i} = 3$		$\frac{R_o}{R_i} = 4$	
	$Ra = 10^4$	$Ra = 10^5$	$Ra = 10^4$	$Ra = 10^5$	$Ra = 10^4$	$Ra = 10^5$
$K = 5$						
$K = 15$						
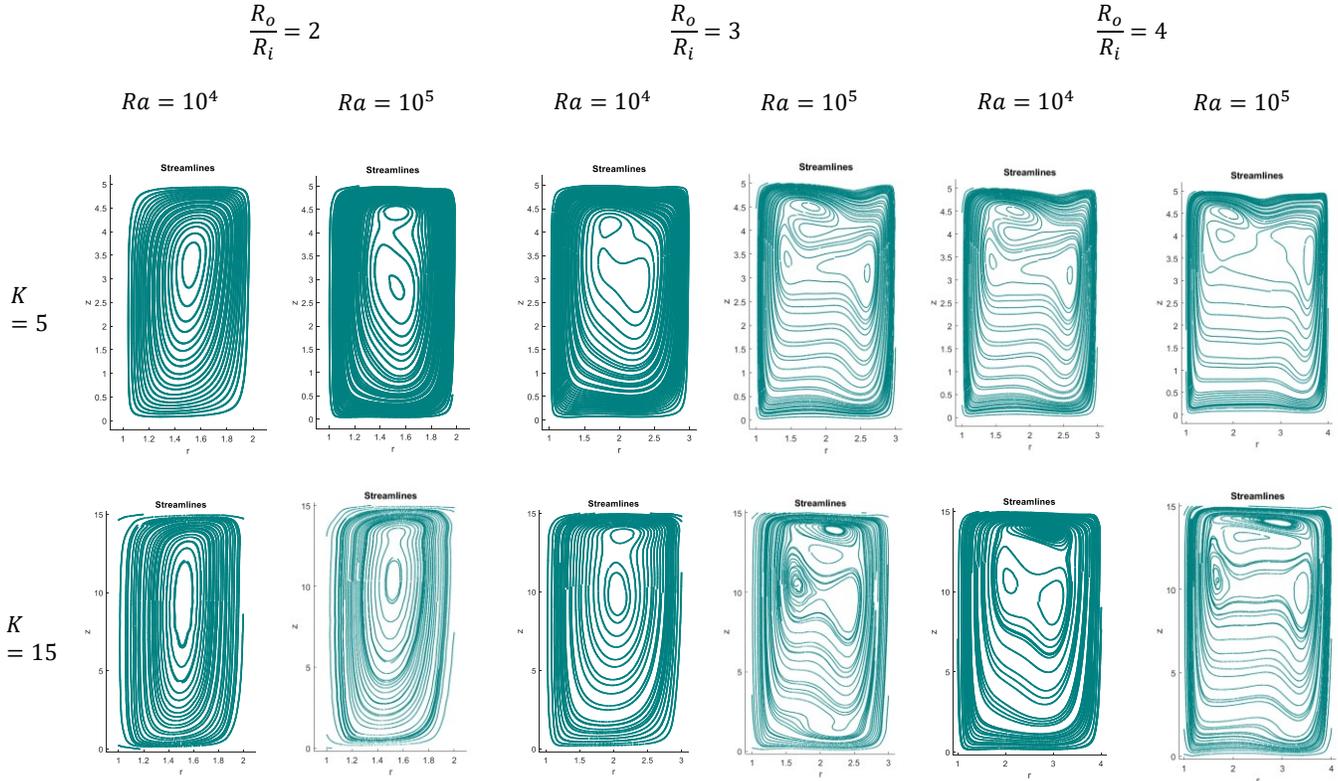
As is shown in Table 4-7, for $\frac{R_o}{R_i} = 2, K = 5$, single-cell flow forms at $Ra = 10^4$ while multicellular motion is apparent at $Ra = 10^5$. The number of cells increases with larger Rayleigh number. For $\frac{R_o}{R_i} = 2, K = 15$, the vortex center moves upwards to the top region of the annulus. In the numerical work of de Vahl Davis and Thomas [28], unicellular flow forms for low Rayleigh number $Ra < 10^5$ while multicellular flow exists for $Ra \geq 10^5$. $Ra = 2 * 10^5$ corresponds almost to a $10^o F$ temperature difference across a 3-in. cavity containing air at normal temperature and the limit to laminar flow in a cavity of $K = 15$. For K =15, the case of $\frac{R_o}{R_i} = 3, Ra = 10^4$ shows an extra vortex on top of the previous vortices, which is wired and does not appear in the case of $\frac{R_o}{R_i} = 2, Ra = 10^4$.

The figures of isotherms are as follows:

Table 4-8: Isotherms with different Rayleigh number and radius radio (aspect ratio =5)

	$\frac{R_o}{R_i} = 2$		$\frac{R_o}{R_i} = 3$		$\frac{R_o}{R_i} = 4$	
	$Ra = 10^4$	$Ra = 10^5$	$Ra = 10^4$	$Ra = 10^5$	$Ra = 10^4$	$Ra = 10^5$

33
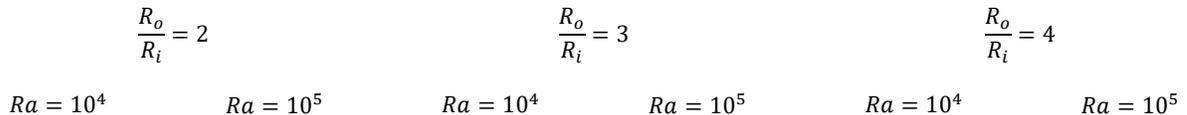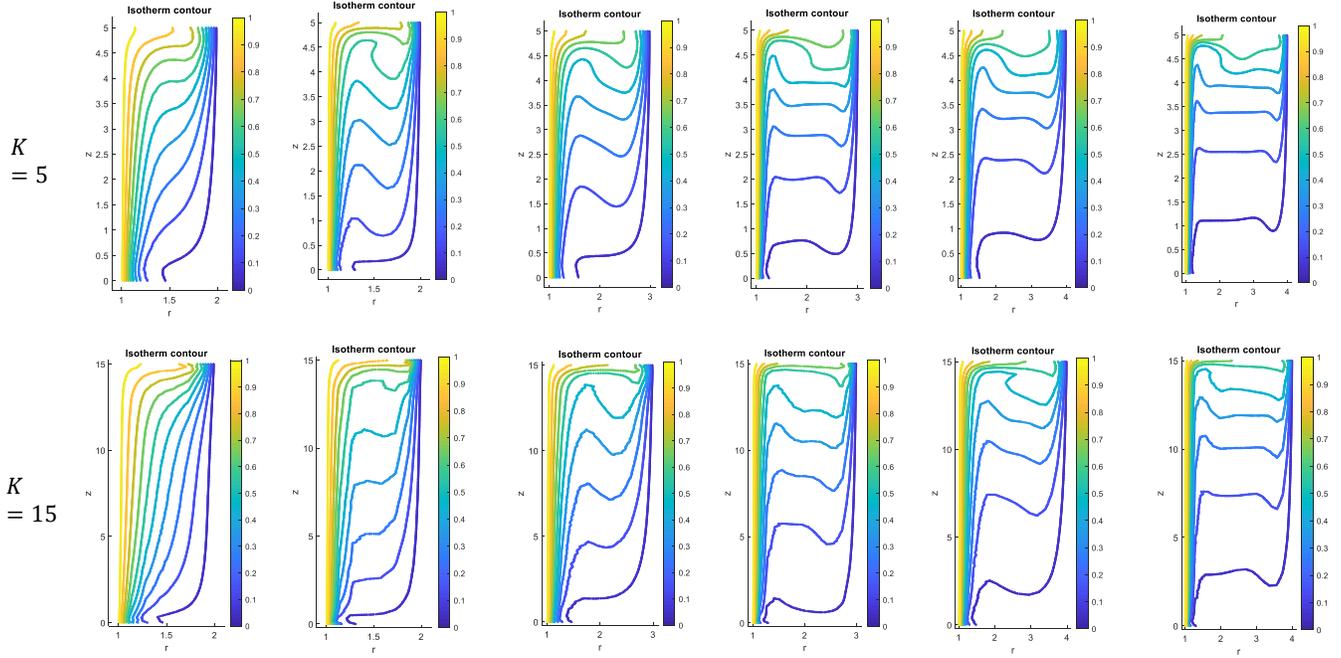
Comparing the isotherm contours in each figure, the following conclusion can be drawn. For low radius ratio ($\frac{R_o}{R_i} = 2$), the heat transfer is more close to conduction. For high radius ratio ($\frac{R_o}{R_i} \geq 3$) and low aspect ratio ($K = 5$), the heat transfer is similar to the 2D square case analysed in Section 3.2, in which the flow is convection dominant. The increase of radius ratio promotes the convection while the increase of aspect ratio suppresses it.

4.3 Conclusion

In Chapter 4, with dimensionless modeling of horizontal and vertical concentric/eccentric cylinders, the variation of flow state with different combinations of Ra and Pr is illustrated. For horizontal annulus, generally, the flow is stable within $10^2 \leq Ra_L \leq 10^6$ and becomes turbulent at high Rayleigh number $Ra_L \geq 10^7$. The transition Ra_L, which corresponds to the transitory stage from laminar to turbulent flow, varies with different Prandtl number Pr. For low Pr ($Pr \leq 0.1$), the thermal diffusivity is high, which leads to strong inertial force and complexity of vortices distribution. In this range, the flow can be turbulent even Ra_L is low. In the case with $Pr \geq 10$, the high viscosity of fluid (strong viscous force) resists the inertial force and the flow is normally in laminar regime. In vertical cylinder case, the height of the annulus was taken into consideration. The Rayleigh number was set in $10^4 \leq Ra_L \leq 10^6$ and The Prandtl number is fixed at $Pr = 1$. For low radius ratio ($R_o/R_i = 2$) and low aspect ratio ($K = 5$), the heat transfer is more close to conduction. For high radius ratio ($R_o/R_i \geq 3$) and higher aspect ratio ($K = 15$), the flow becomes convection dominant. The increase of radius ratio develops the convection flow while the increase of aspect ratio suppresses it. Besides, with the increase of aspect ratio, multi celluars (vortices) form in the vertical direction.

5 SIMULATION OF SCENARIO CASES

The numerical analysis in Chapter 4 has proven the feasibility of analysing natural convection problem in COMSOL. The dimensionless model gives general solution based on dimensionless parameters Ra, Pr and Re. In this Chapter, dimensional model is built in COMSOL to derive solution in a specific scenario case. The exported results from COMSOL are compared with experimental data in relevant papers to make further motification of the boundary condition setting to improve the simulation result quality. In Section 5.1, the dimensional models of 2D concentric and ecctric cylinders are compared to Kuehn's work in [4] and in [5]. Comparisons between experimental results and numerical results show good agreement. In Section 5.2, 3D horizontal concentric/eccentric cylinders are built to observe the impact of end effects to the heat transfer process. A vertical axisymmetric concentrical cylinder model is built in Section 5.3 based on scenario data to initially observe the influence of layed soil to the heat dissipation process. Finally, the model based on scenario data is built to detect the temperature and localization of hotspots along the pipeline.

5.1 Two-dimensional model of Horizontal Cylinders

5.1.1 Concentric cylinders

The study of heat convective transfer in an annulus occurs in several engineering applications. T.H.Kuehn and R.J.Goldstein did a great amount of study (experimental and theoretical) in this field. In their experiment, the temperature distribution in the annulus was visualized by an interferometer [4]. The experimental temperature variations was recorded by Interferograms. The test fluid (water/air) was filled in an annulus with a ratio of outer to inner cylinder diameter $D_o/D_i = 2.6$. The radius difference between concentric cylinders is defined as: $L = (D_o - D_i)/2$ and $L/D_i = 0.8$. A numerical model is built in COMSOL based on the geometry of experimental scenario.
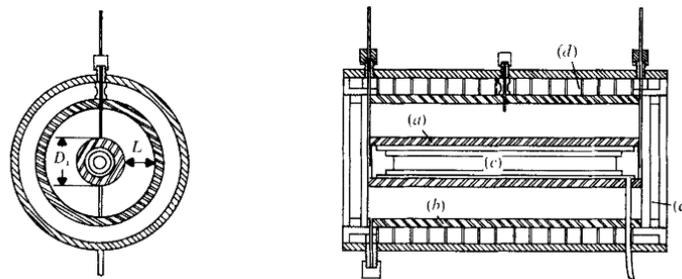
Figure 5-1: Experimental instruments (a) Inner cylinder, (b) Outer cylinder, (c) Heater, (d) Cooling water channels, (e) Window [4]

In Kuhen's experiment, copper tubes are chosen to build the concenric cylinder structure. The outside diamter and inside diamter of the outer cylinder was 9.7 cm and 9.25 cm seperately. The outside diameter and inner diameter of the inner cylinder is 3.56 cm and 3.05 cm seperately. The heat was generated by inducing regulated DC current throught a tubular resistor (about 100 ohms) in the center of the inner cylinder. The experimental result was recorded after the system reached a steady state and a steady temperature on the surface of the inner and outer cylinder T_i and T_o was recorded.

To verify Kuhen's experimental result, it is assumed in COMSOL that the steady laminar flow is invariant in the axial direction. Hence, the temperature distribution at any cross-section in horizontal direction can be considered the same in steady state. In this way, the local heat flux can be calculated based on a 2-D concentric circles. The inner and outer cylinder are set

as isothermal layers with constant temperature T_i and T_o. The arithmetic mean temperature $T_f = (T_i + T_o)/2$ is used to evaluate the physical properties of fluid.

An streamlines and isothermal contour from [4] in Figure 5-2 is compared to the COMSOL simulation result in Figure 5-3. These two figures show a similar distribution of isothermal contours.
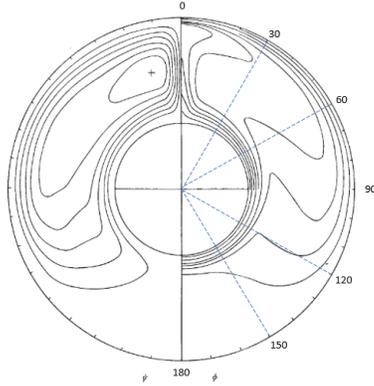
Figure 5-2: Streamlines and isothermal contour (water) for $Ra_L = 9.53 * 10^4$, $Pr = 6.34$ (adapted from [4])
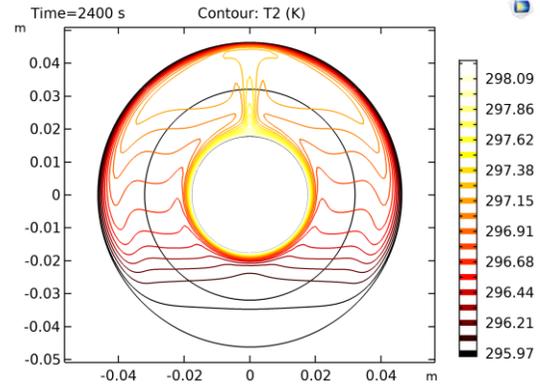
Figure 5-3: COMSOL isothermal contour with ($\Delta T = 2.356^0 C$, $\frac{T_i + T_o}{2} = 23.94^0 C$) and derived data $Ra_L = 9.47 * 10^4$, $Pr = 6.25$,

Due to temperature difference between inner and outer cylinder, the fluid near the inner cylinder is heated first and become less dense. The warm fluid rises due to buoyancy force and forms the buoyant plume. The plume keeps rising until touching the separation point of outer cylinder and splits into two heat flow in opposite direction. After that, the hot fluid moves along the boundary of outer layer towards the bottom and mixes up with the cold fluid there. The mixed fluid rises again due to buoyancy force.

The 2D isothermal contour in Figure 5-3 still cannot implement a clear comparision of temperature variation in different postion of the annulus. Hence, as shown in Figure 5-2, the temperature distribution in radial direction from 0^0 to 180^0 can be plotted instead for a better illustration. The dimensionless radial temperature distribution for the case $Ra_L = 2.09 * 10^5$ and $Pr = 5.45$ is shown in Figure 5-4 . After carrying out dimensionless parametrization, the temperature of the inner cylinder equals to one while it equals to zero of the outer cylinder. Each curve indicates the temperature distribution along the dashed line of the corresponding angle.
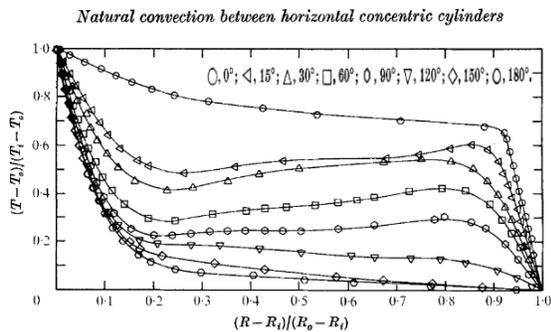
Figure 5-4: Temperature distribution of water in [4] for $Ra_L = 2.09 * 10^5$, $Pr = 5.45$.
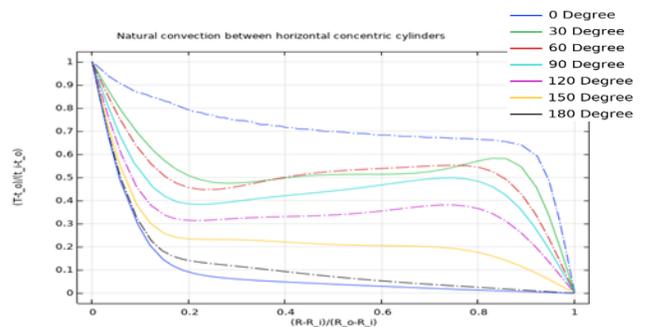
Figure 5-5: Temperature distribution of water in COMSOL ($\Delta T = 0.371^0 C$, $\frac{T_i + T_o}{2} = 30.03^0 C$)

The experimental result in [4] shows similar plot as the numerical result, except slight difference of curves at 30^0, 60^0 and 90^0. From an experimental point of view, it is speculated that the difference is because of the deficient isothermal condition

of inner and oute cylinder. From a simulation point of view, some errors might exist due to the assumption of some ideal boundary condtions or the coarse mesh size setting. Besides, the possiblity of transient turbulent flow in experiment cannot be excluded since the motion of turbulent flow cannot be reflected in simulation due to the application of laminar flow equations in COMSOL. Hence, the measurement value of table 1 in [4] may contain error. To verify this speculation, after changing the fillled medium from water to air, a simulation with the same geometry and setting is implemented to observe a more obvious variation.
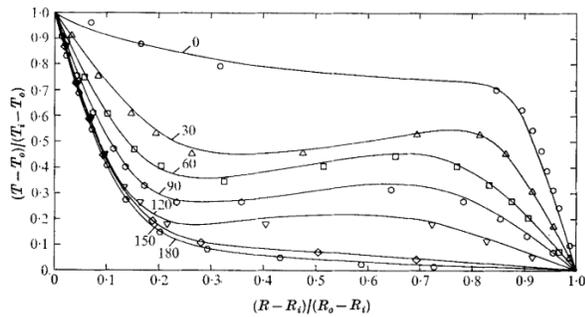

Figure 5-6: Temperature distribution of air in [4] for $Ra_L = 4.7 * 10^4, Pr = 0.706$.
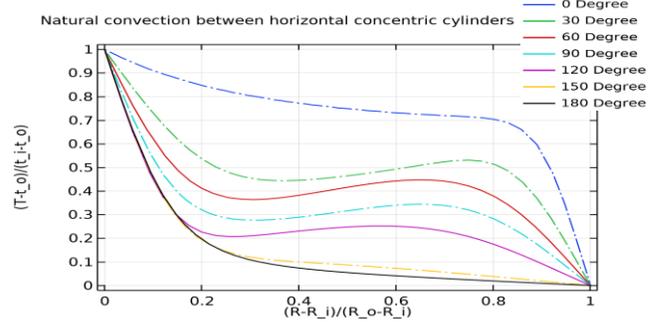
Figure 5-7: Temperature distribution of air in COMSOL ($\Delta T = 26.3^0 C$, $\frac{T_i + T_o}{2} = 35.23^0 C, Ra_L = 5 * 10^4, Pr = 0.7$)

The radial temperature plot of annulus filled with air in Figure 5-7 shows a good match between numerical and experimental result (which difference is within 10%). The temperature oscillation in the radial direction of $30^0, 60^0, 90^0, 120^0$ can be explained by the variation of thermal boundary layer. According to dimensionless model result in Section 4.1, when $Ra \geq 10^4$ and $Pr \geq 1$, the thermal boundary layer is divided into two parts, one close the inner cylinder, one close to the outer cylinder. The cross symbol in Figure 5-8 shows the center of the vortex.
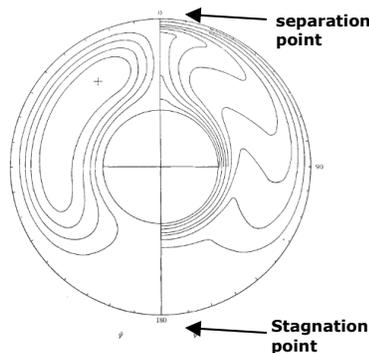
Figure 5-8: Streamlines and isotherm($Ra_L = 5 * 10^4, Pr = 0.7$ [4])
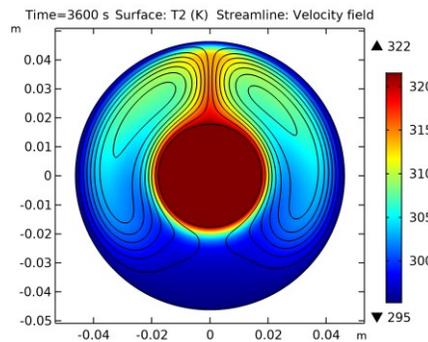
Figure 5-9: Streamlines and temperature distribution with $Ra_L = 5 * 10^4, Pr = 0.705$ in COMSOL
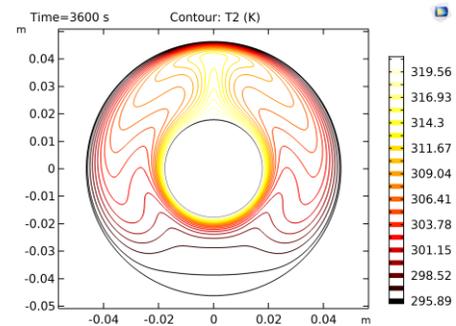
Figure 5-10: isothermal distributions with $Ra_L = 5 * 10^4, Pr = 0.705$ in COMSOL

As shown in Figure 5-9 and Figure 5-10, the upward moving hot fluid splits into two symmetric vortices rotating in opposite direction after touching the top region of outer cylinder boundary. A plume is formed in the upper region. The COMSOL result agrees well with the experiment in [4], the numerical result in [18] and CVFEM simulation result in [29].

As shown in Figure 5-11, the separrate velocity layers close to the boundary of inner and outer cylinder further proves the explanation of thermal boundary layer. As the fluid moves down past the 90" position, the outer boundary layer weakens, and disappears entirely near the bottom.
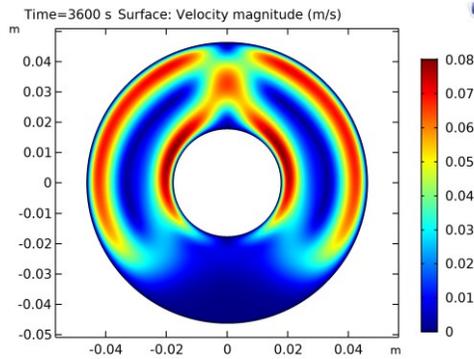
Figure 5-11: Velocity distributions ($Ra_L = 5 * 10^4$, $Pr = 0.705$ in COMSOL)
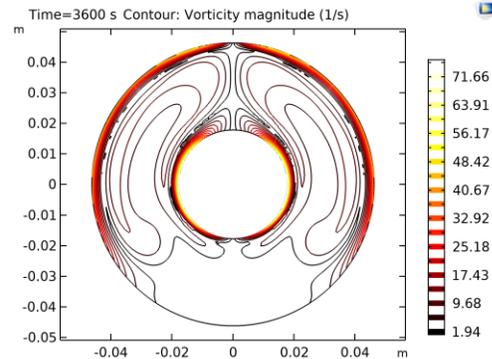
Figure 5-12: Vorticity contour ($Ra_L = 5 * 10^4$, $Pr = 0.705$ in COMSOL)

According to the figures of velocity layer and vorticity distribution, which are symmetric, it can be found that there is a region where the velocity is close to zero in the region from 20^0 to 120^0, which indicates a kidney-shaped stagnant region. To further comparing the accuracy of this numerical modelling, after changing the matches of $\varDelta T$ and $(T_i + T_o)/2$, the corresponding result are shown in Table 5-1. The value of Q is calculated by using line intergral function in COMSOL to calculate the normal heat flux through the inncer cylinder boundary in transver direction and multiplied by the length of tube (20.32cm) in longitindual direction. The value of Ra_L and Pr can be calculated based on eq. 2-27, eq. 2-25 and listed togther with Q in Table 5-1. The result shows a difference less than 5% to the value in Table 1 of [4].

Table 5-1: COMSOL results for $\frac{D_o}{D_i} = 2.6$ (air)

| $\varDelta T$	$(T_i + T_o)/2$	$Q(W)$	Ra_L	Pr
11.14	33.46	1.00	$2.23 * 10^4$	0.70499
14.37	35.03	1.33	$2.74 * 10^4$	0.70468
17.12	36.55	1.65	$3.19 * 10^4$	0.70438
20.02	36.11	2.01	$3.76 * 10^4$	0.70447
20.41	28.57	2.06	$4.3 * 10^4$	0.70597
26.30	35.23	2.82	$5.01 * 10^4$	0.70464
31.42	36.12	3.50	$5.90 * 10^4$	0.70447
41.65	41.28	4.94	$7.24 * 10^4$	0.70348
50.53	50.66	6.24	$7.67 * 10^4$	0.70178
60.16	50.57	7.73	$9.14 * 10^4$	0.70179
69.27	55.13	9.18	$9.86 * 10^4$	0.701

The intensity of mixing of fluid in natural convection and the heat dissipation rate can be reflected by the average equivalent conductivity $\overline{k_{eq}}$. The average equivalent conductivity is defined as the ratio of Nusselt number in the actual heat flux

condiction and in pure conduction condition, $\overline{k_{eq}} = \frac{\overline{Nu}}{Nu_{cond}}$ [4]. Bishop (1966) found that $\overline{k_{eq}}$ is basically a parameter which associates Ra with the gap size of the annulus [30]. Accroding to the simultion result, it can be concluded that on the outer cylidenr surface, the maximum $\overline{k_{eq}}$ locates at the separation point in the top region while the minimum $\overline{k_{eq}}$ locates at the stagnation point in the bottom region. Conversely, the inner cylinder surface shows an opposite distribution of $\overline{k_{eq}}$.
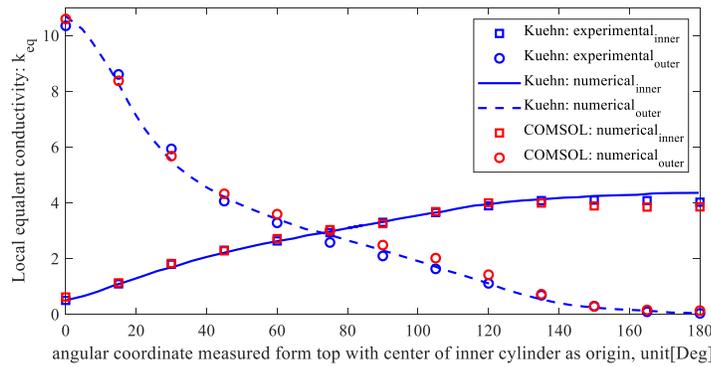
Figure 5-13: Comparison of local equivalent conductivity between experimental, numerical results of Figure 16 in [4] and those in COMSOL.

5.1.1 Eccentric cylinders

Optical methods were used to record the temperature distribution in the experiment [5]. After completing the analysis of concentric cylinder case, the inner cylinder was moved upwards and downwards in the vertical direction to observe the variation of temperature distribution with the change of inner cylinder position. A ratio between the distance of inner cylinder moving away from the center ε_v and the radius difference L is defined to represent the shift extent of the inner cylinder.

The eccentric case with $\frac{\varepsilon_v}{L} = 0.652$ is shown as below:
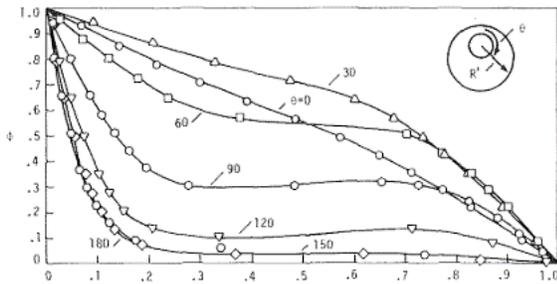
Figure 5-14: Temperature distribution in [5] ($\frac{\varepsilon_v}{L} = 0.652$, $Ra_L = 4.8 * 10^4$, $Pr = 0.706$)
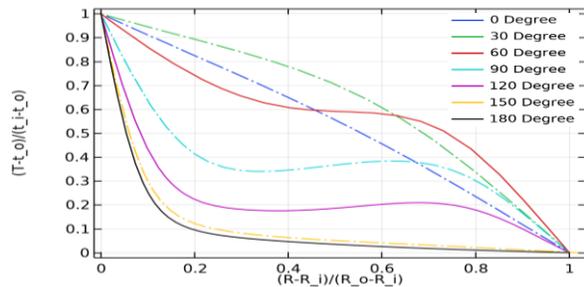
Figure 5-15: COMSOL modelling result ($\frac{\varepsilon_v}{L} = 0.652$, $\Delta T = 26.3^0C$, $\frac{T_i+T_o}{2} = 35.23^0C$, $Ra_L = 5 * 10^4$, $Pr = 0.70464$)

The eccentric case with $\frac{\varepsilon_v}{L} = -0.623$ is shown as below:
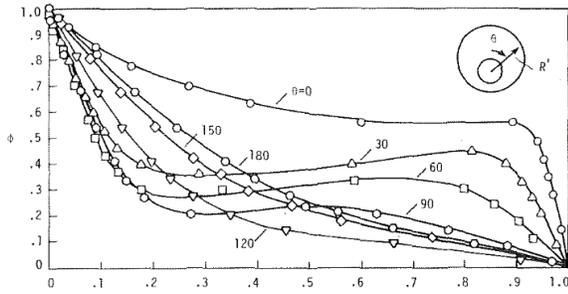
Figure 5-16: Temperature distribution in [5] ($\frac{\varepsilon_v}{L} = -0.623$, $Ra_L = 4.93 * 10^4$, $Pr = 0.706$)
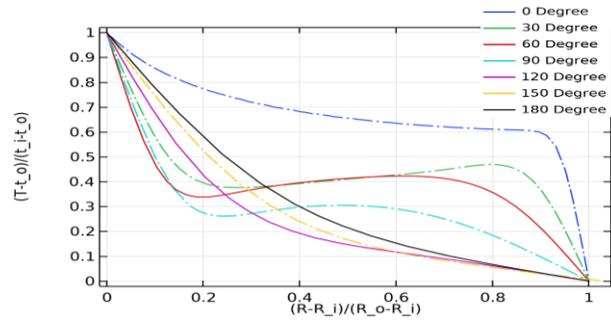
Figure 5-17: COMSOL modelling result ($\frac{\varepsilon_v}{L} = -0.623$, $\Delta T = 26.3^0 C$, $\frac{T_i + T_o}{2} = 35.23^0 C$, $Ra_L = 5 * 10^4$, $Pr = 0.70464$)

As it can be seen from the figures above, in the region where cylinders are far apart from each other, the radial temperature distribution curves of the corresponding angles (90^0, 120^0, 150^0 and 180^0) have a similar trend to those in the concentric case. However, in the top region where the two cylinders (inner and outter) are adjacent to each other, the curves show a totally different trend compared to the concentric case, especially in the angle of 0^0, 30^0 and 60^0. Instead of tempeature inversion in convection mode, the temperature distribution in these regions shows an approximately linear heat transfer, which is more close to conduction mode. Hence, it can be concluded that the distortion of curves in these regions is because of the space limitation of the narrow gap, which restricts the fluid motion and forces the heat to transfer in conducitve mode rathre than in convective mode.

A comparison is made between different eccentricity ($Ra_L = 5 * 10^4$, $Pr = 0.70464$):
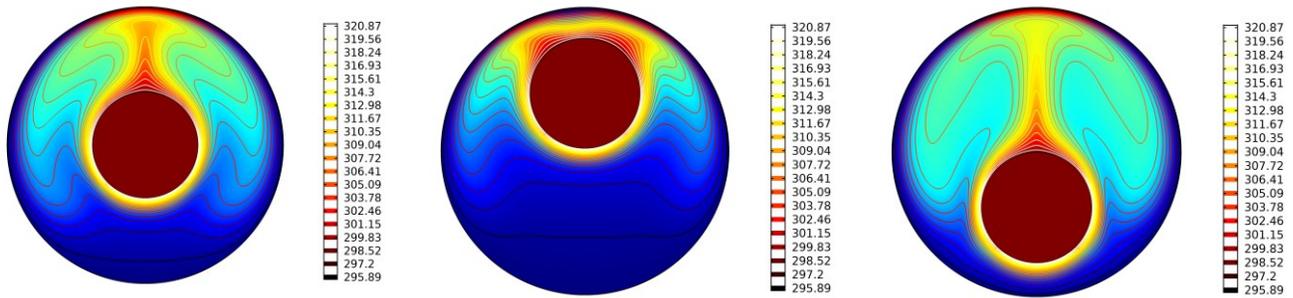
Figure 5-18: Isothermal contours in COMSOL (a) $\frac{\varepsilon_v}{L} = 0$, $\Delta T = 26.3^0 C$, $\frac{T_i + T_o}{2} = 35.23^0 C$; (b) $\frac{\varepsilon_v}{L} = 0.652$, $\Delta T = 26.3^0 C$, $\frac{T_i + T_o}{2} = 35.23^0 C$; (c) $\frac{\varepsilon_v}{L} = -0.623$, $\Delta T = 26.3^0 C$, $\frac{T_i + T_o}{2} = 35.23^0 C$;
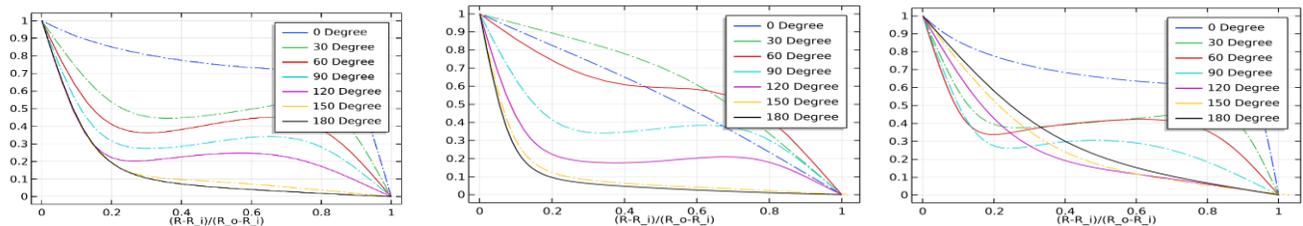
Figure 5-19: Dimensionless temperature distribution (a) $\frac{\varepsilon_v}{L} = 0$, $\Delta T = 26.3^0 C$, $\frac{T_i + T_o}{2} = 35.23^0 C$; (b) $\frac{\varepsilon_v}{L} = 0.652$, $\Delta T = 26.3^0 C$, $\frac{T_i + T_o}{2} = 35.23^0 C$; (c) $\frac{\varepsilon_v}{L} = -0.623$, $\Delta T = 26.3^0 C$, $\frac{T_i + T_o}{2} = 35.23^0 C$;

40

Heat-transfer coefficient at a particular point on the heat-transfer surface equals to the local heat flux at this point (q_w) divided by the local temperature drop (Δt):

$$h_i = \frac{q_{\omega i}}{(T_i - T_o)}, h_o = \frac{q_{\omega o}}{(T_i - T_o)}$$

Local equivalent conductiviy k_{eq} can be used to presented the heat transfer results. It is defined as the ratio of the thermal conductivity that a motionless fluid in the gap must have to transmit the same amount of heat as the test fluid to the actual thermal conductivity of the moving test fluid [31]. The local equivalent conductivity can be calculated based on the heat transfer coefficient equations [5]:

$$k_{eq(inner)} = \frac{h_i D_i \ln\left(\frac{D_o}{D_i}\right)/2}{k}, k_{eq(outer)} = \frac{h_o D_o \ln\left(\frac{D_o}{D_i}\right)/2}{k}$$

The local equivalent coefficients k_{eq} are plotted in Figure 5-20 and Figure 5-21 for the eccentric cylinder cases. When $\frac{\varepsilon_v}{L} = 0.652$ (the inner cylinder is moved up), k_{eq} at $\theta = 0^0$ shows a value far from that in the concentric case. The maximum and minimum value of k_{eq} for outer and inner cylinder appears separately at $\theta = 30^0$ instead of at $\theta = 0^0$. The profile of eccentric case with $\frac{\varepsilon_v}{L} = -0.623$ is similar to that of the concentric case but the uniformity of k_{eq} distribution increase on both cylinders. It can be concluded that k_{eq} relies heavily on the shift extent of the inner cylinder position. When the inner and outer cylinders get close to each other (either $\frac{\varepsilon_v}{L} > 0$ or $\frac{\varepsilon_v}{L} < 0$), due to heat conductive transfer in the stagnant fluid in the gap , k_{eq} will increase significantly in this region.
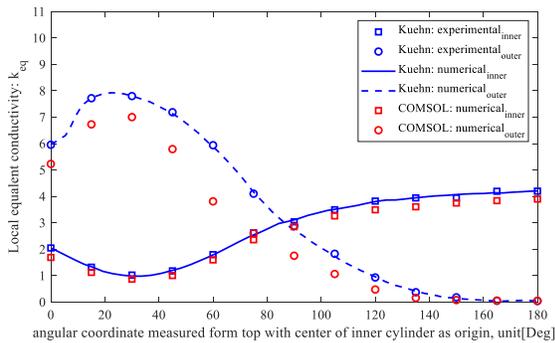
Figure 5-20: Comparison of k_{eq} between experimental, numerical results of Figure 5 in [5] and those in COMSOL ($\frac{\varepsilon_v}{L} = 0.652$).
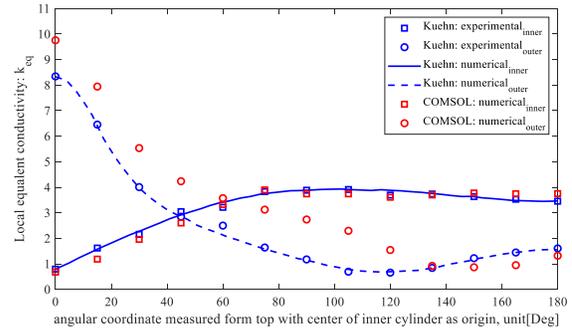
Figure 5-21: Comparison of k_{eq} between experimental, numerical results of Figure 5 in [5] and those in COMSOL ($\frac{\varepsilon_v}{L} = -0.623$).

5.2 Three-dimensional Model of Horizontal Cylinders with Open Ends

5.2.1 Concentric cylinders

Horizontal annulus is a classical geometry to be applied for industrial problem analysis such as gas insulated transmission lines (GIL). Heat is produced due to ohmic loss of the cable conductor, sheath loss as well as dielectric loss. The heat dissipation is implemented by heat convection of fluid and heat conduction through the wall of conduit, which penetrate onto the surface of conduit. Usually, an electrically heated wire installed on the surface of annulus which contains the fluid [28] is used to measure the thermal conductivity of the fluid.

The heat dissipation relies on the natural convection of air or water filled in the annulus. This engineering issue can be simplified as natural convection analysis in a 3D horizontal concentric cylinder. The issue of the outer surface should be set

as isothermal or adiabatic is investigated numerically. An adiabatic wall indicates that no heat is exchanged through it ($\Delta Q = 0$ and $\Delta T \neq 0$) while an isothermal wall indicates that $\Delta T = 0$ and therefore $\Delta U = 0$ (only for ideal gas) but $\Delta Q \neq 0$.

The annulus is filled with air. For isothermal case, an isothermal condition (T= 300K) is set on the outer cylinder surface while a constant heat flux (Q = 0.21W/m)is set on the inner cylinder, which in real case is due to heat generation of electrical resistance from the power cable. For adiabatic case, thermal insulation layer is set to the outer cylinder while the inner cylinder condition is the same as it in isothermal case. Since the flow field is symmetric with regard to the vertical plane through the center of the annulus, the model can be schematically built as shown in Figure 5-22 :
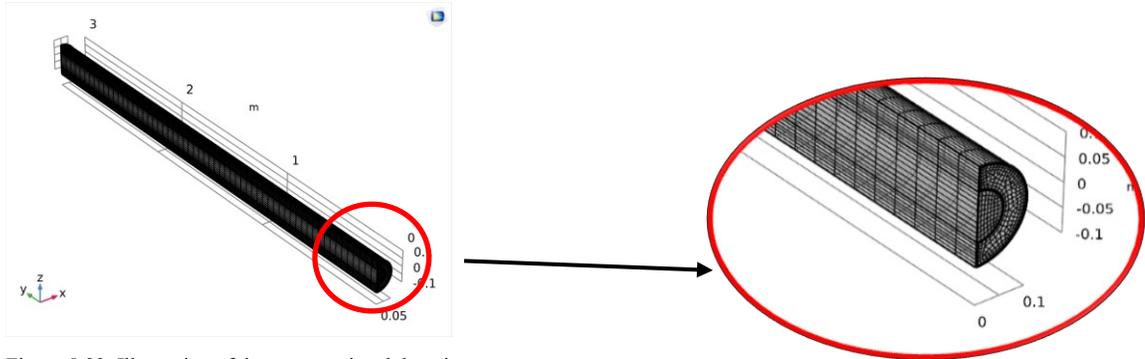
Figure 5-22: Illustration of the computational domain

The boundary conditions used in COMSOL are as follows. An isothermal surface $T_0 = 300K$ is set on the outer cylinder surface ($R_{outer} = 0.2m$) in isothermal case. In adiabatic case, thermal insulation condition is set on the outer cylinder surface. A constant heat flux ($q_w = 31.72$ W/m) is given to the inner cylinder ($R_{inner} = 0.1m$). The angular velocity which crosses the longitudinal symmetric plane vanishes. An inlet ($u_0 = 0$ m/s) and an outlet ($P_0 = 0$ Pa) is set separately on two open ends of the pipeline. Considering the heat dissipation path in the pipeline, an inflow (fresh flowing fluid, $T_{upstream} = 300K$, $P_{upstream} = 1$ atm) and an outflow (heated flowing fluid) is set on the two open ends of the conduit. The medium filled in the annulus is air ($Pr = 0.7$). The longitudinal length is 3m.

A modified Rayleigh number, which adapted from [32], is defined for this case with a constant heat flux of the inner cylinder:

$$Ra_L = Pr * Gr \equiv \frac{v}{\propto} * \frac{\beta g (T_i - T_o) L^3}{v^2} = \frac{g \beta D_h^3}{v \propto} \left(\frac{q_w D_h}{k_{ref}} \right), D_h = D_o - D_i$$

As stated in [32], a transition from laminar to turbulent flow state occurs at $Ra = 10^7$. In this case, $Ra = 2 * 10^5$ is defined in the simulation as a relatively steady temperature variation. Boussinesq approximation is not adopted in this simulation due to relatively high temperature difference. Instead, the ideal gas law is used for density determination. The cut planes of velocity and temperature distribution in the transverse and longitudinal direction are shown separately from the view of (a) and (b) in Figure 5-23.
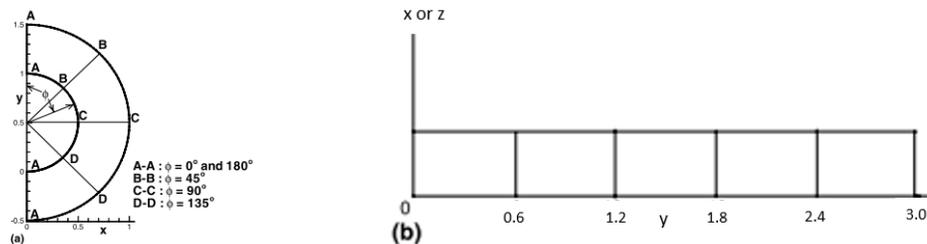
Figure 5-23: Illustration of cross section (a) transverse direction; (b) longitudinal direction (adapted from [32])

The following figures show the velocity vector plots at selected sections in longitudinal directions.
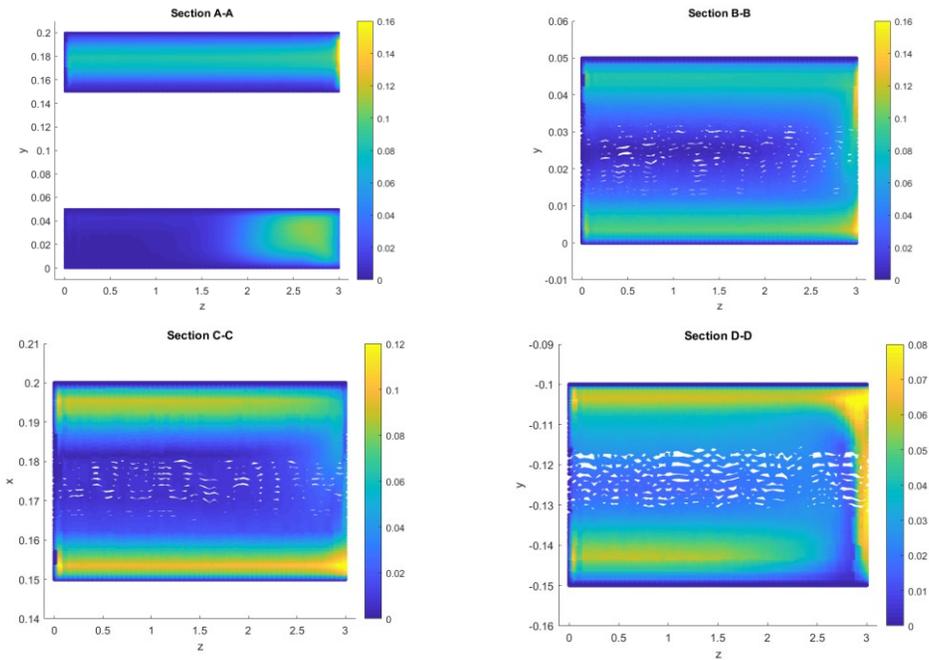
Figure 5-24: Velocity vector plots (white area is due to low-size mesh) in longitudinal direction

Figure 5-24 shows the velocity vector plots on the longitudinal sections. It is clearly seen that the main high velocity flow concentrate close to the boundary walls from "Section B-B", "Section C-C" and "Section D-D". To achiever a detailed observation, the velocity vectot plots of cross sections in transverse direction are shown as below:
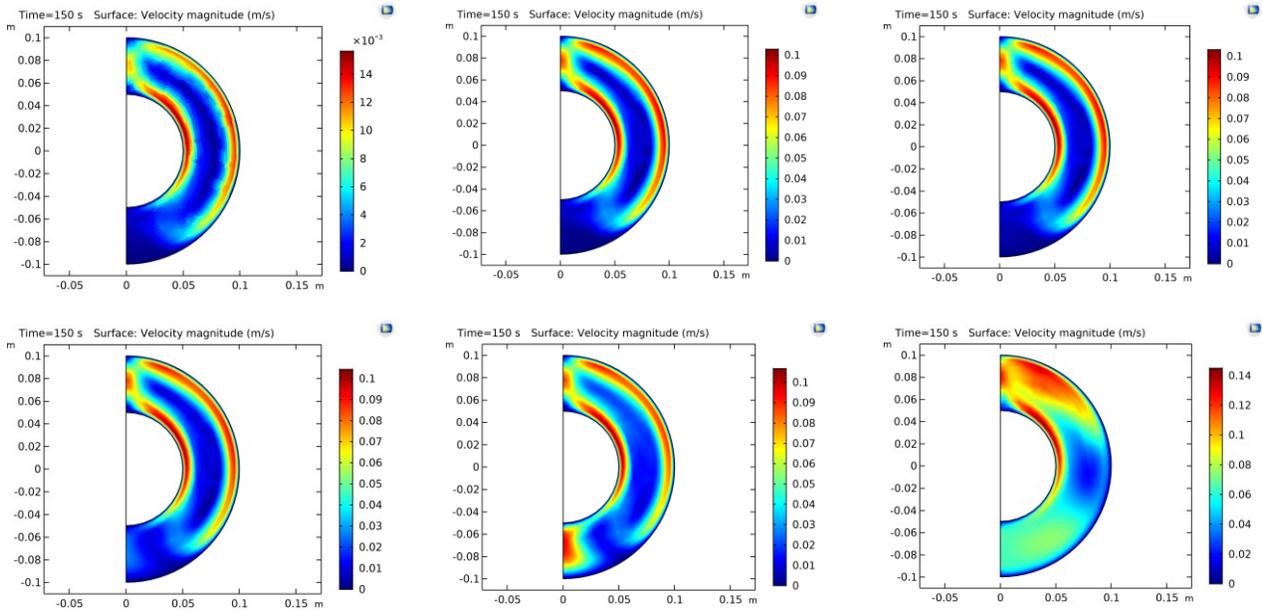
Figure 5-25: Velocity layer at selected cross sections (a) y=0; (b) y=0.6; (c) y=1.2; (d) y=1.8; (e) y=2.4; (f) y=3.0;

To further prove the conclusion found in Figure 5-24, the velocity plots at selected transverse sections are shown in Figure 5-25. It can be observed that the higher velocity regions locate around the upper portion of the annulus and the velocity layer focus close to the boundary of walls. The velocity close to the outer cylinder shows a stable and flat curve from y=0.6 to y=2.4. From y=2.4 to y=3.0, the velocity shows an increase in the bottom region since the area near the outlet plane consists of inflow (imported cold fluid) and outflow (exported heated fluid).

Besides, the 3D streamline plots in Figure 5-26 shows that the main high velocity regions locate around the upper portion of the annulus while also locate around the bottom region near the outlet plane, which indicates heat exchange in this area.
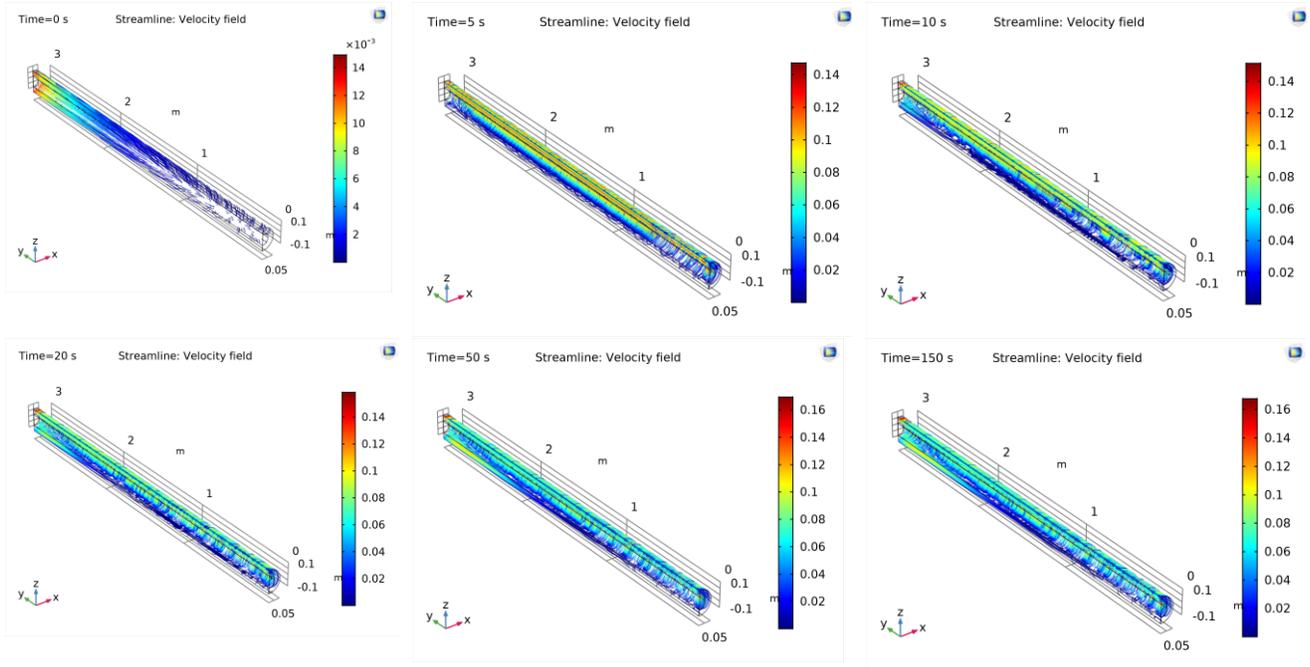
Figure 5-26: Streamlines of the vector field (isothermal)

Figure 5-27 shows the temperature distribution at selected longitudinal directions. It can be observed that the higher temperature region focuses mainly on the "Section A-A" and "Section B-B", which is in the portion above the inner cylinder.
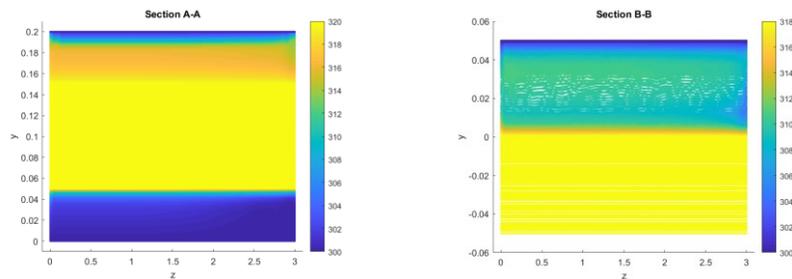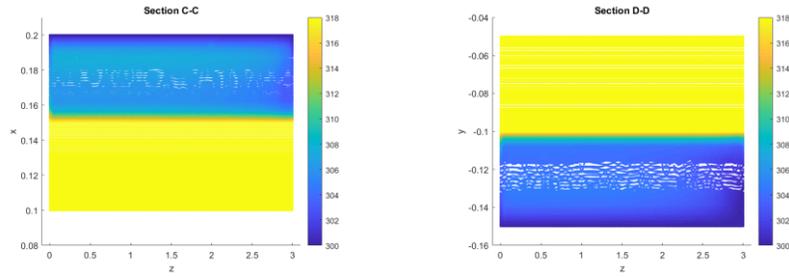
Figure 5-27: Temperature distribution (isothermal) at selected longitudinal sections

For heat source as inner cylinder and isothermal outer cylinder, the change of temperature with regard to time on the inner cylinder surface is shown as below:
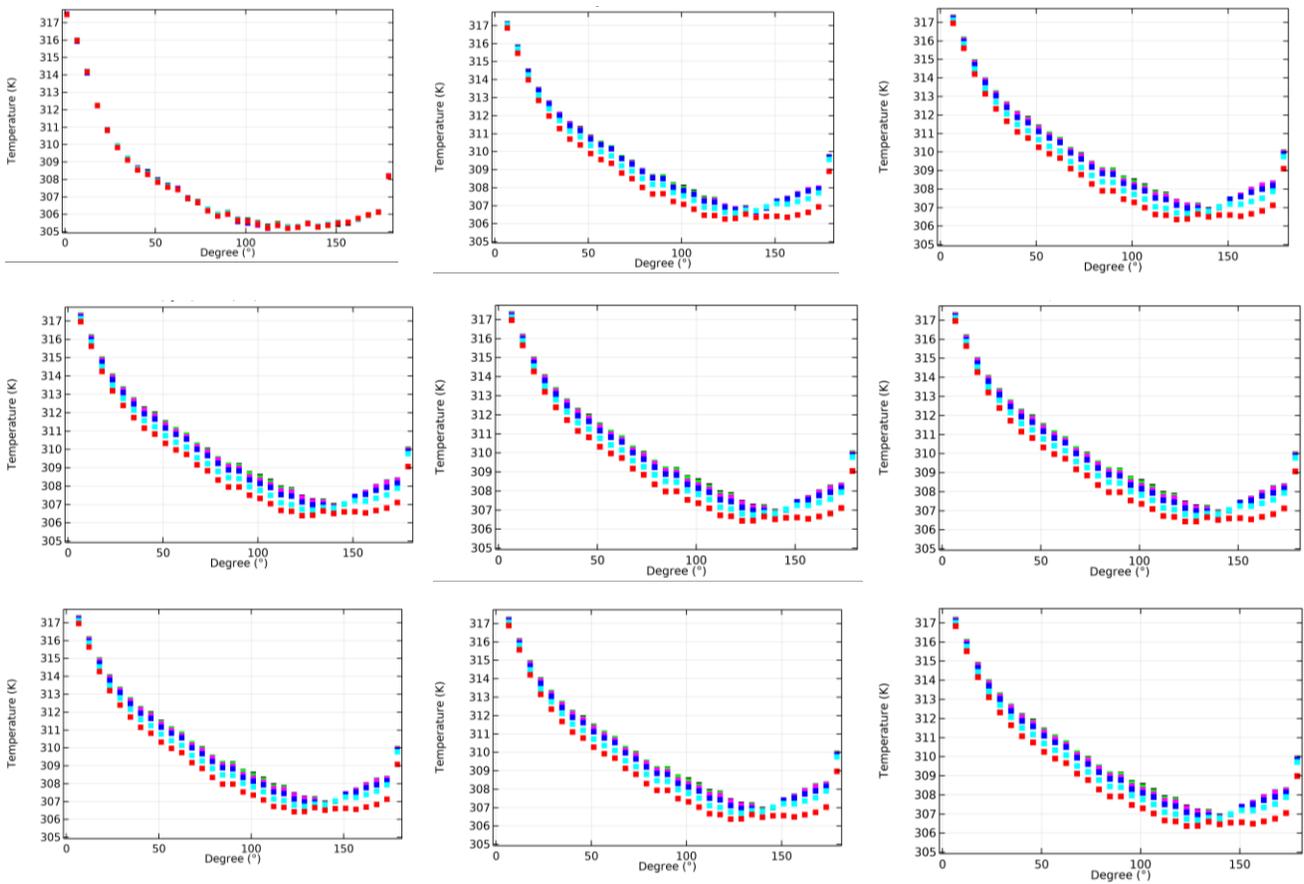
Figure 5-28: Azimuthal temperature distribution (isothermal) along the inner cylinder surface (T=5, 20, 40, 70, 110, 120, 130,200,300) [y=0 (black), y=0.6 (green), y=1.2 (magenta), y=1.8 (blue), y=2.4 (cyan), y=3.0 (red)]

By contrast, for heat source as inner cylinder and adiabatic outer pipeline, the change of temperature with regard to time on the inner cylinder surface is shown as below:
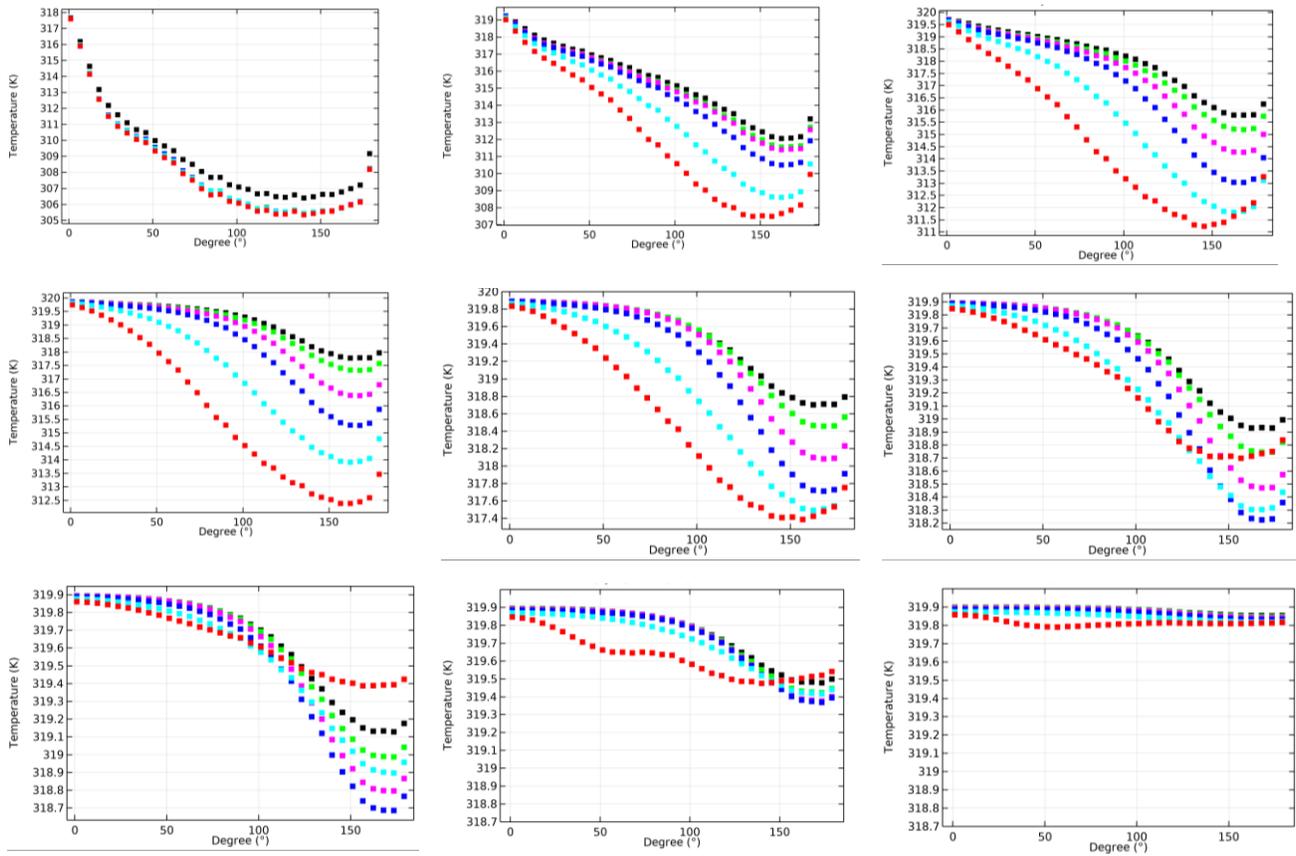
Figure 5-29: Azimuthal temperature distribution (adiabatic) along the inner cylinder surface (T=5, 20, 40, 70, 110, 120, 130,200,300) [y=0 (black), y=0.6 (green), y=1.2 (magenta), y=1.8 (blue), y=2.4 (cyan), y=3.0 (red)]

Figure 5-28 and Figure 5-29 shows the radial temperature distributions along the radial line of the inner cylinder at selected transverse sections with regard to time in isothermal and adiabatic cases. Compared these two cases, it is clearly seen that the isothermal case reaches steady state faster than the adiabatic case. In steady-state, the isothermal model remains a temperature difference between inner and outer cylinder while the adiabatic model reaches an uniform temperature everywhere and the temperature continues to increase. It can be observed that for both cases, the highest temperature in each transverse section occurs right at the top of the inner cylinder (i.e., $\emptyset = 0^o$). In adiabatic cases, the temperature on the inner cylinder surface decrease along the pipeline path towards the outlet plane. In isothermal cases, the temperature on the inner cylinder surface remains almost the same on each selected transverse section.
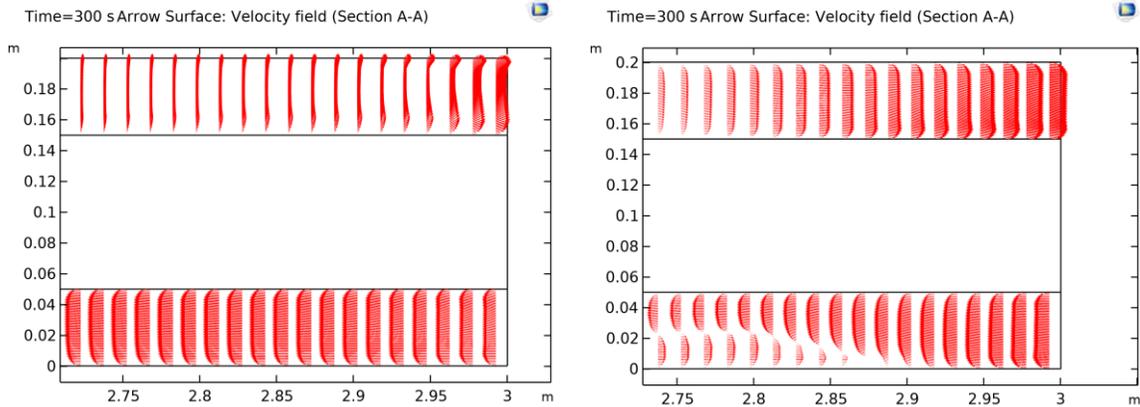
Figure 5-30: The velocity field near the outlet plane (a) isothermal case; (b) adiabatic case.

It is clearly seen in Figure 5-30 that there exists two directional flows near the region closed to the outlet plane (inflow and outflow). For both cases, the outflow is observed in the portion above the inner cylinder while the inflow is observed in the portion below. Such flow patterns are due to the buoyancy effect, which can be explained by the thermal plume phenomenon as mentioned in Section 4.1.

Figure 5-31 shows the temperature distribution at selected transverse sections. The isothermal case is shown as below:
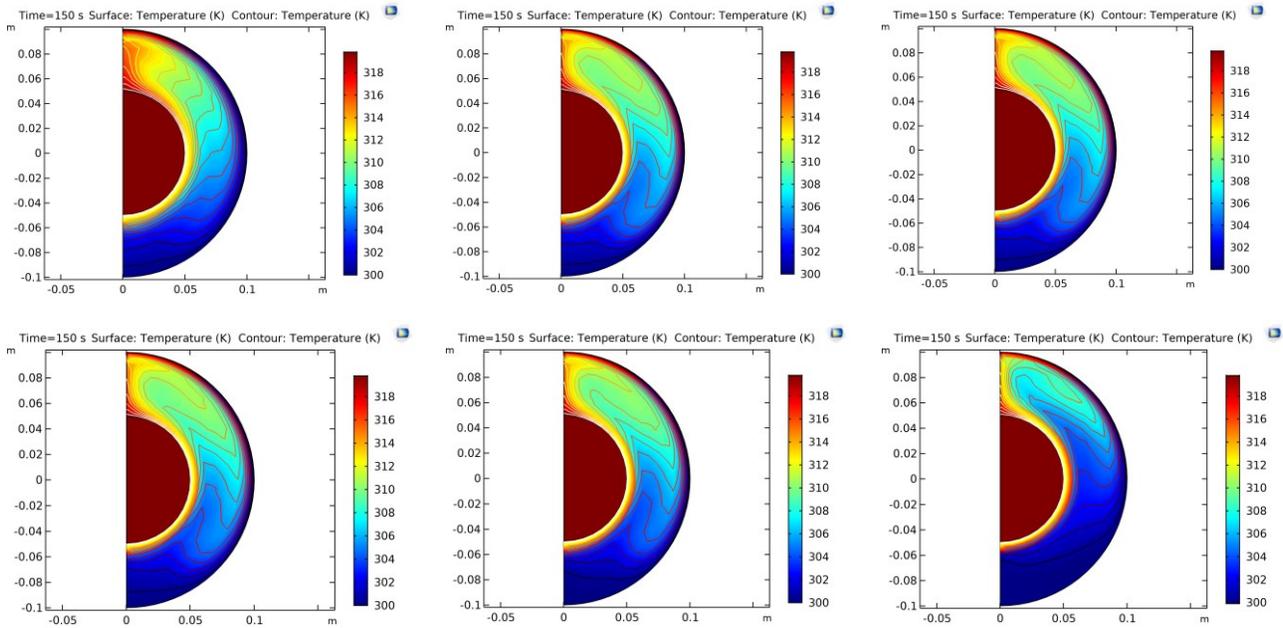
Figure 5-31: Temperature distribution (isothermal, t=150s) at selected transverse sections (a) y=0; (b) y=0.6; (c) y=1.2; (d) y=1.8; (e) y=2.4; (f) y=3.0;

By contrast, the temperature distribution for the adiabatic case is shown in Figure 5-32:
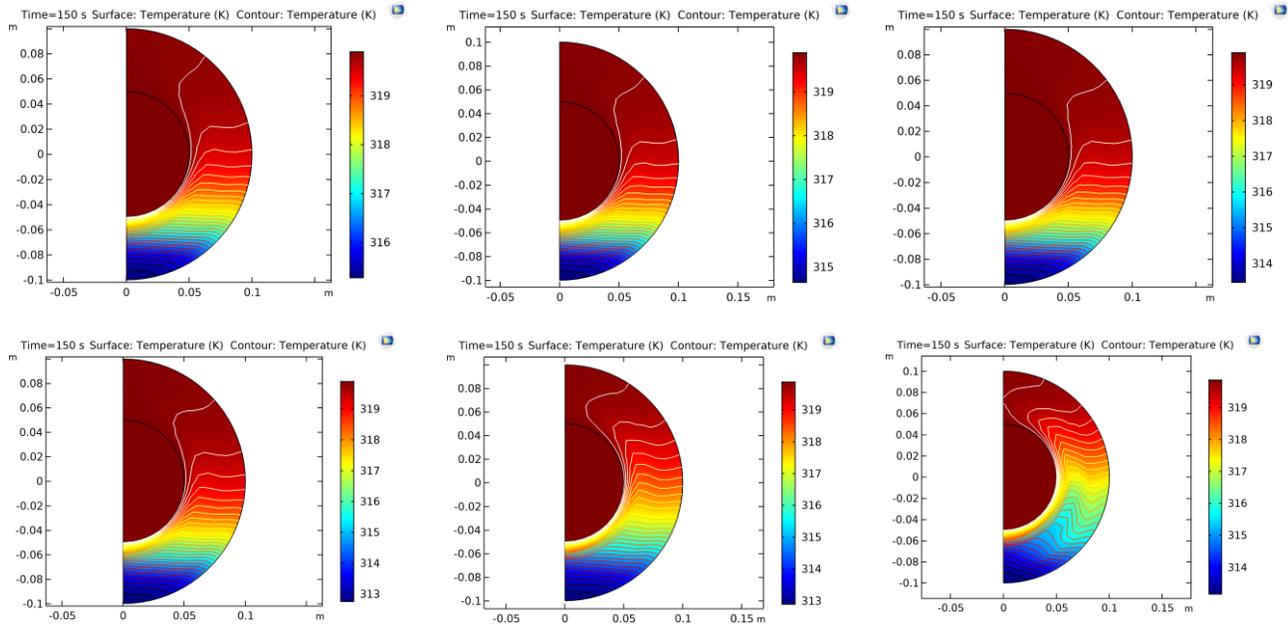
Figure 5-32: Temperature distribution (isothermal, t=150s) at selected transverse sections (a) y=0; (b) y=0.6; (c) y=1.2; (d) y=1.8; (e) y=2.4; (f) y=3.0;

It is clearly seen that the higher temperature region locate in the upper portion of the inner cylinder surface while the cold flow is observed in the portion below. This can also be seen from the plots of azimuthal temperature distribution in Figure 5-28 and Figure 5-29.

Based on the COMSOL simulation result, it is found that for concentric cylinder, the maximum temperature occurs in the top region of the annulus above the inner cylinder. The "zonal grid" method suggested in [32] is different from the "inlet" or "outlet" function in COMSOL. This "zonal grid" approach is suitable for non-cavity model with buoyancy-induced flow. This method extends the open end to a large cubical space filled with fluid, which physical properties are set according to ambient environment. This method is not appliable in COMSOL and hence the "inlet" or "outlet" function is used instead.

In conclusion, cases with adiabatic and isothermal outer cylinder surface are tested. It is found that for both cases, the maximum temperature occurs in the top region of the annulus above the inner cylinder. For the adiabatic case, in the direction along the pipeline path from inlet to outlet, the general temperature at selected transverse sections decreasees. Oppositely, for the isothermal case, the temperature distribution remains almost similar for each selected transverse section.

Since the isothermal/adiabatic condtion needs to be used in the final scenario as well, a prediction is given that the isothermal condition might influence the simulation accuracy if it is not set appropriately. Given that the whole HDD path is coverd by the soil space, the geometry of the soil should be large enough to reduce the influnce of isothermal boundry condition to the HDD path. The computation of heat convective transfer in the region close to the isothermal boundary will be suppressed since the temperature will be the same, which causes result distortion.

5.2.1 Eccentric cylinders

Based on the drawback of isothermal condition found in the previous section, analysis of the eccentric cylinder model is continued only in adiabatic condition. As it is shown at selected transverse sections of annulus in Figure 5-33, even the temperature in the top regio of the annulus is still high, but the maximum temperature on the surface of inner cylinder occurs right at the bottom region (near the contacting point between outer and inner cylinders). The general temperature at selected transverse sections decreases along the path of pipeline from inlet to outlet plane.
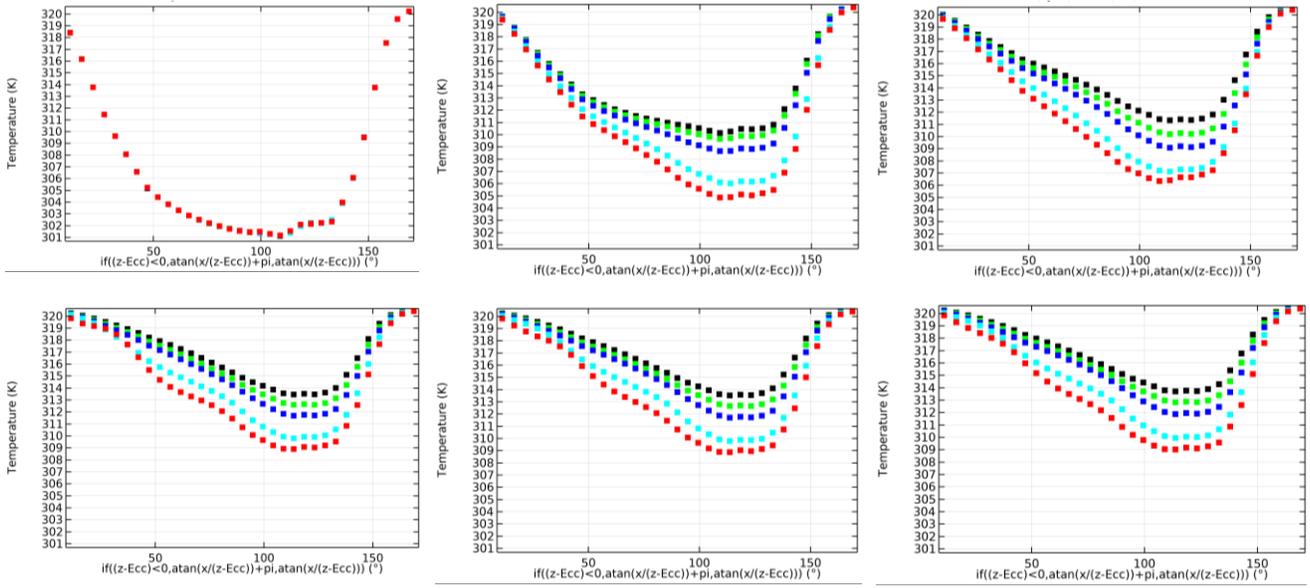
Figure 5-33: Azimuthal temperature distribution (adiabatic) along the inner cylinder surface from y=2.4 to y=3.0 (T= 5, 20, 40, 80, 150, 200) [y=0 (black), y=0.6 (green), y=1.2 (magenta), y=1.8 (blue), y=2.4 (cyan), y=3.0 (red)]

Besides, the velocity vector plots at selected transverse sections are plotted as well:
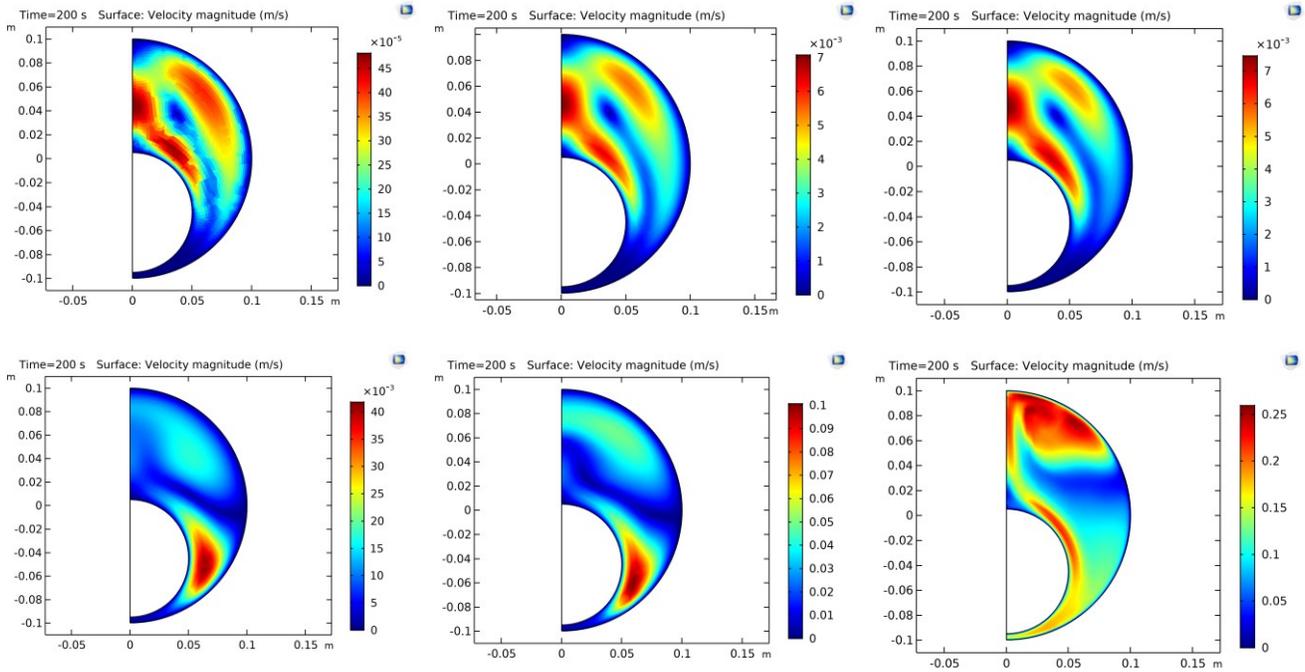
Figure 5-34: Velocity layer at selected cross sections (a) y=0; (b) y=0.6; (c) y=1.2; (d) y=1.8; (e) y=2.4; (f) y=3.0;

It can be observed in Figure 5-34 that high velocity layers still locate around the upper portion of the annulus and focus close to the boundary of walls from y=0 to y=1.2. However, at selected transverse sections from y=1.8 to y=2.4, the velocity distribution extends to the bottom portion of the annulus and the peak velocity in the eccentric case is lower than that in the

concentric case. Near the open end (which is outlet plane), the velocity layer shows an abnormal change due to the crash of inflow (cold fluid flow) and outflow (hot fluid flow).

Figure 5-35 shows the temperature distributions at selected transverse sections. Compared to the concentric case, it can be observed that instead of $\emptyset = 0^o$, the maximum temperature occurs near the bottom of the inner cylinder (i.e., $\emptyset = 180^o$). The inner cylinder temperature surface decrease slightly along the pipeline path towards the outlet plane.
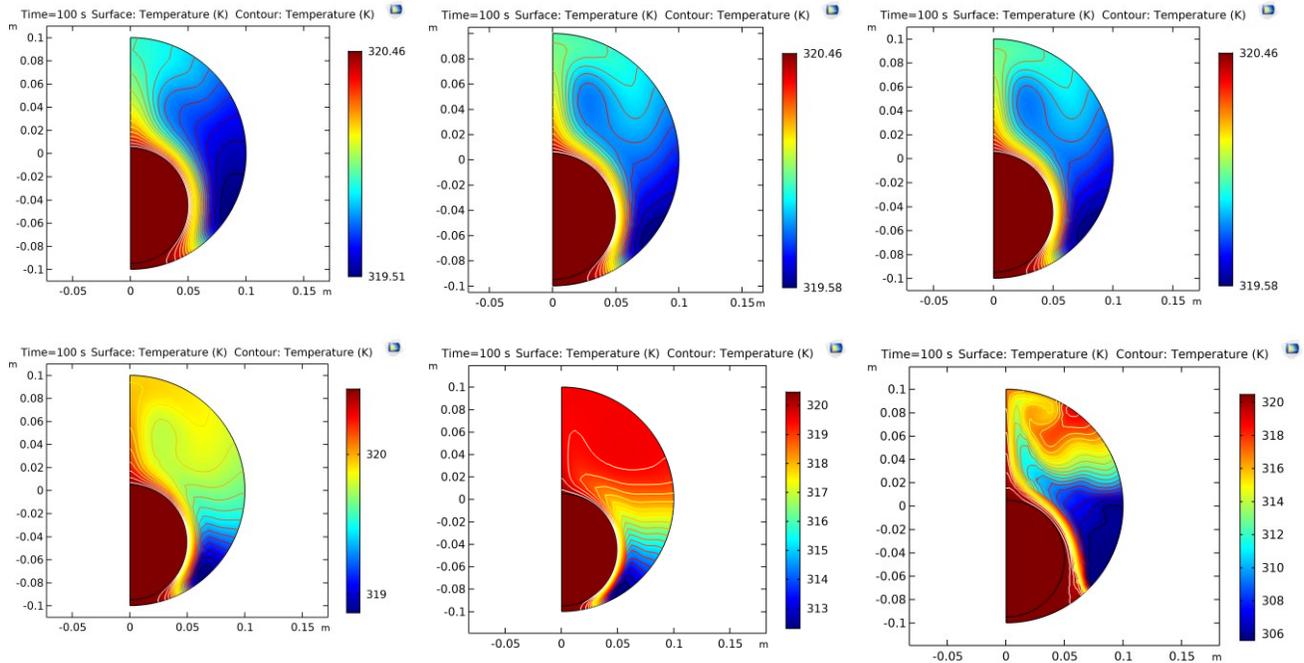
Figure 5-35: Temperature distribution at selected transverse sections (a) y=0; (b) y=0.6; (c) y=1.2; (d) y=1.8; (e) y=2.4; (f) y=3.0;

In conlcusion, the eccentric annulus has a worse heat dissipation rate compared with the concentric annulus. The temperature still shows a decrease tendency from the inlet to outlet plane. Compared to the maximum temperature of inner cylinder surface occuring at the top region in concentric annulus case, the higher temperature occurs in the region near the bottom of the eccentric annulus.

5.3 Axisymmetric Model of Vertical Concentric Cylinders

5.3.1 Conduction case (cable radius: 0.05 m)

It is necessary to discuss which mode is more suitable to use for thiss simulation: stationary or time-dependent mode. Hence, a conduction case in a vertical annulus is tested first to distinguish the better option. The height of the vertical concentrical cylinder is 1m. The radii of cable and soil are $r_c = 0.05m$ and $r_s = 0.55m$ seperately. The soil thickness is $t_1 = r_s - r_c = 0.5m$. As shown in Figure 5-37, two cut points are set to observe the temperature. (0.05, 0.5) indicates a point on the interface between cable and soil and (0.3, 0.5) indicates a position in the center of the soil region. The thermal conductivity of soil is $1 \text{ W/m} \cdot \text{K}$.
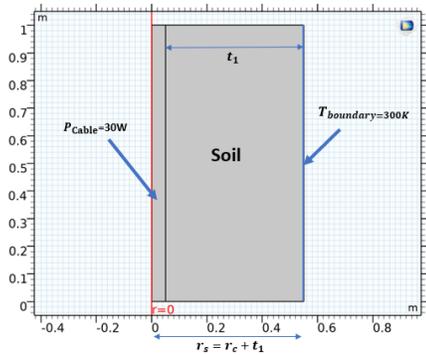
Figure 5-36: Model geometry
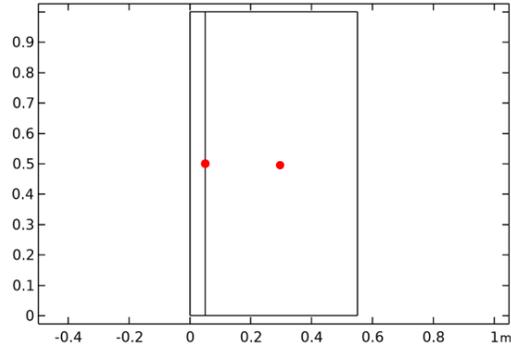
Figure 5-37: Cut points chosen for temperature measurement: left: (0.05, 0.5), right: (0.3, 0.5)

The equation from [33] can be used to initially evaluate the temperature increase at the cutpoint (0.05, 0.5):

$$R_{general} = ln\left(1 + \frac{2t_1}{d_c}\right) * \frac{1/k}{2\pi} \qquad \text{5-1}$$

$$R_{general} = ln\left(1 + \frac{2 * 0.5}{0.1}\right) * \frac{1}{2\pi} \approx 0.38 \text{ K/W}$$

$$\Delta T = P * R_{general} = 30 * 0.38 = 11.45 \text{ K}$$

$$T_{cable} = T_{boundary} + \Delta T = 311.45 \text{ K}$$

Firstly, a stationary simulation is implemented and the temperature distribution is shown as below. As it can be seen, the temperature at (0.05, 0.5) is the same as the calculation result with eq. 5-1.
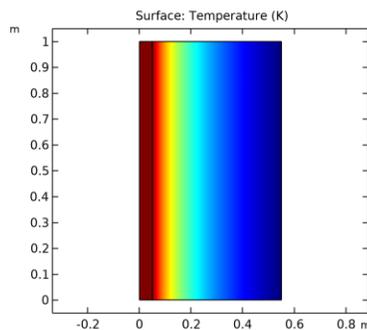
Figure 5-38: Temperature distribution in stationary mode
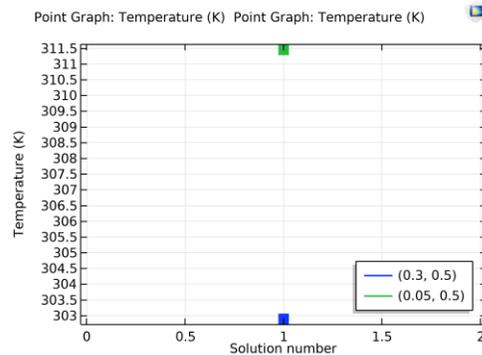
Figure 5-39: Temperature variations at selected cut points

Next, a time-dependent model with the same boundary conditions is implemented and the temperature distribution is shown as below:
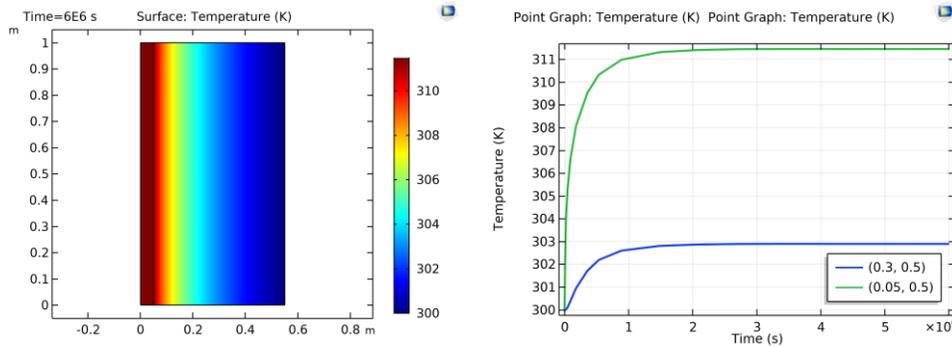
Figure 5-40: Temperature distribution in time dependent mode   Figure 5-41: Temperature variations at selected cut points

As it can be seen, it takes about $1.5 * 10^6$ seconds for the time-dependent model to reach a stead state as the stationary model. The time cost is high for the heat source model to heat up the geometry totally. Hence, the following simulations in this chapter are implemented in stationary mode.

5.3.2 Conduction case (cable radius: 0.1m)

In this section, the area influence of heat source domain is discussed. Based on the previous model, the cable radius is extended to 0.1m and other settings are kept the same.

The height of the vertical concentrical cylinder is 1m. The radii of cable and soil are $r_c = 0.1m$ and $r_s = 0.6m$ seperately. The soil thickness is $t_1 = r_s - r_c = 0.5m$. The thermal conductivity of soil is $1 \text{ W/m} \cdot \text{K}$. The equation from [33] can be used to initially evaluate temperature increase:

$$R_{general} = ln\left(1 + \frac{2 * 0.5}{0.2}\right) * \frac{1/1}{2\pi} \approx 0.285 \text{ K/W}$$
$$\Delta T = P * R_{general} = 30 * 0.38 = 8.55 \text{ K}$$
$$T_{cable} = T_{boundary} + \Delta T = 308.55 \text{ K}$$

A stationary simulation is implemented and the temperature distribution is shown as below. (0.1, 0.5) indicates a point on the interface between cable and soil and (0.35, 0.5) indicates a position in the center of the soil region.
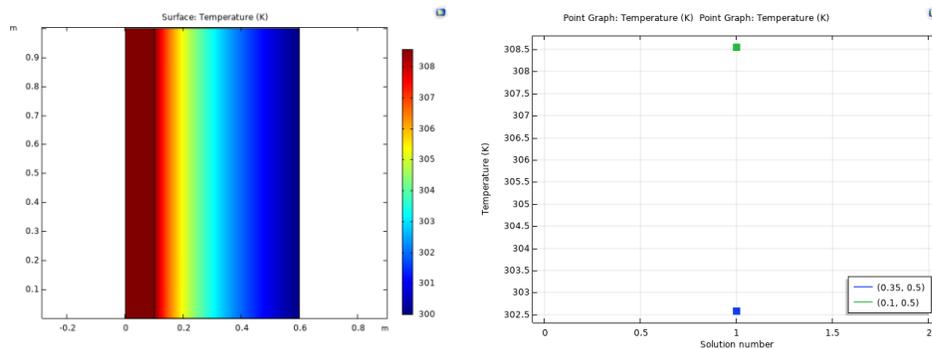
Figure 5-42: Temperature distribution in stationary mode   Figure 5-43: Temperature variations at selected cut points

As it can be seen, the temperature on the surface of cable is 308.55K, which is the same as calculation result.

5.3.3 Convection case (water with fixed thermal conductivity)

Considering the scenario environment, a annulus filled with water is added between soil and cable. The thermal conductivtiy is fixed at 0.6056 W/m · K to observe the temperature distribution in stationary water first. Since in stationary state, heat transfer in water can be considered in pure conductive mode.Hence, eq. 5-1 can still be used to evaluate the temperature increase on the interface between water and soil:

$$R_{general} = ln\left(1 + \frac{2t_1}{d_c}\right) * \frac{\frac{1}{k}}{2\pi} = ln\left(1 + \frac{2*0.5}{0.2}\right) * \frac{\frac{1}{1}}{2\pi} \approx 0.285 \ K/W$$
$$\Delta T = P * R_{general} = 30 * 0.285 = 8.55 \ K$$
$$T_{pipe} = T_{boundary} + \Delta T = 308.55 \ K$$

A stationary simulation is implemented and the temperature distribution is shown as below.
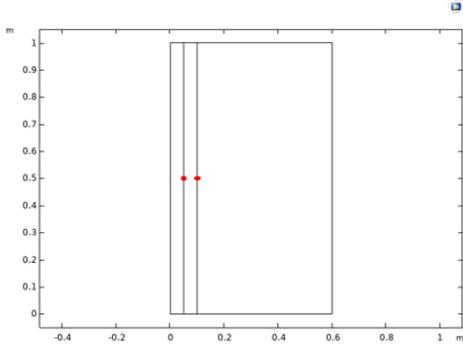
Figure 5-44: cut points for temperature measure   Figure 5-45: Temperature variations at selected cut points
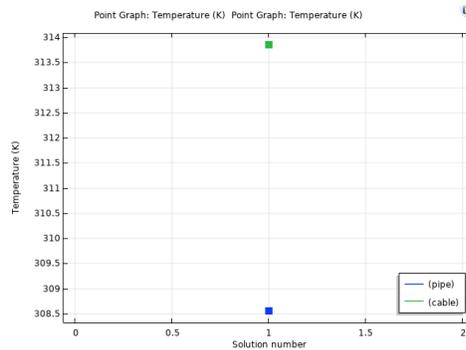
As it can be seen, the temperature increase on the surface of pipe is the same as calculation result.

5.3.4 Convection case (water with variable thermal conductivity)

Considering the scenario environment, the thermal conductivity of water is temperature dependent. After changing the thermal conductivity of water from constant to temperature dependent, the temperature cut points on the interface between pipe and soil is shown as below:
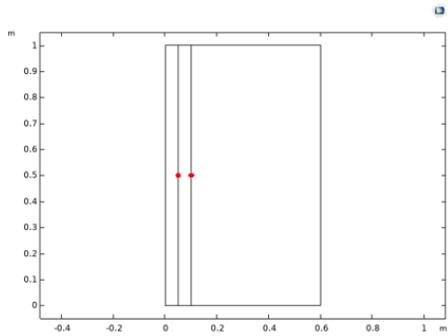
Figure 5-46: cut points for temperature measure   Figure 5-47: Temperature variations at selected cut points
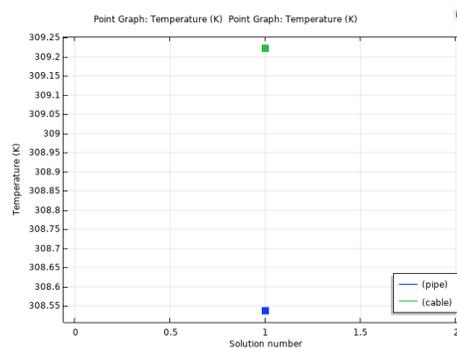
Comparing the two cases of heat conductive and convective transfer in water in Section 5.3.3 and Section 5.3.4, it is found that natural convection in the new added water layer suppresses the temperature increase on the cable surface. However, the temperature increase on the pipe surface is the same for both cases according to Figure 5-45 and Figure 5-47. Three cutlines

are set to cross the the top, middle and bottom regions of the geometry and a clear comparision of temperature distribution is shown as below:
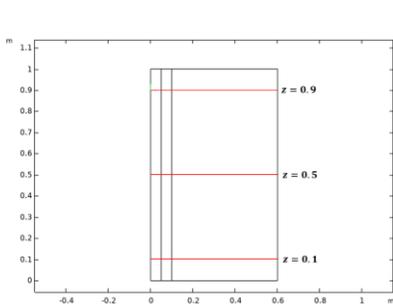
Figure 5-48: The cut-lines defined for temperature measure (z=0.9, 0.5 and 0.1)
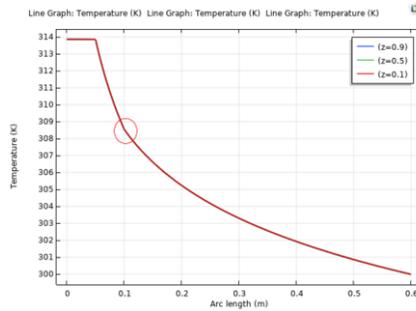
Figure 5-49: Temperature distribution along the cut-lines in stationary (conductive) water case
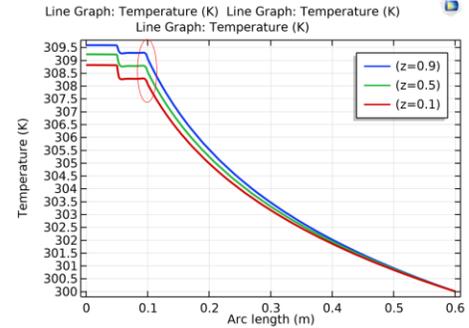
Figure 5-50: Temperature distribution along the cut-lines in convective water case

As it can be seen, in the red circle area, the temperature distribution in different regions in Figure 5-49 is the same from left to right since in this state heat transfers by pure conduction in water. However, the temperature distribution varies in different region in Figure 5-50 due to natual convection of water. The heated fluid flow upwards and the energy accumulates in the top region. Hence, the general temperature along cut line z = 0.9 is higher than that along cutline z=0.5 and z=0.1.

5.3.5 Scenario vertical annulus set with heat source condition

Now, the original single soil layer is replaced by four layers of soil with different thermal conductivities, which are 1 W/m · K, 2 W/m · K, 0.9 W/m · K and 1.5 W/m · K seperately from the top to the bottom layer. Vertical annulus models with different aspect ratio ($K = \dfrac{H}{R_o - R_i}$) are simulated to see the influence of height to the temperature distribution. The figure below shows the isothermal and temperature distributions of case with 0.1 meter height, $K = \dfrac{H}{R_o - R_i} = \dfrac{0.1}{0.05} = 2$.
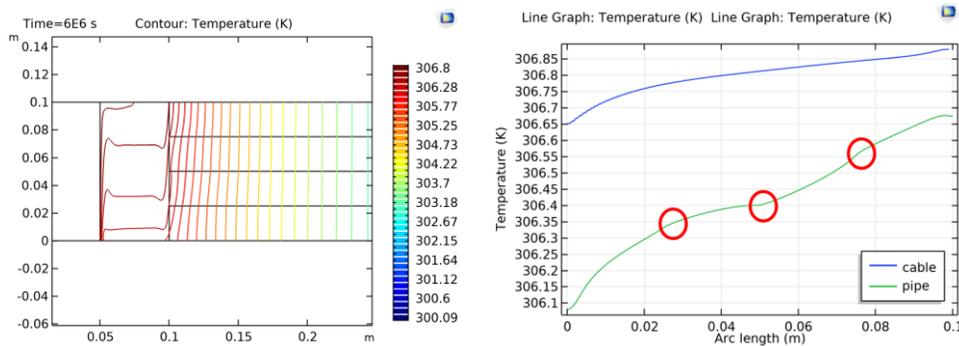
Figure 5-51: Temperature distribution of annulus with constant heat source [0.1m] (a) isothermal contours; (b) temperature along the boundary of inner cylinder and outer cylinder.

It can be found that the temperature rises along the positive y-axis direction from the bottom to the top end due to the buoyancy effect. The heated fluid becomes less dense and flows upwards to the top region of the annulus. Some bulges can be detected in the red-circle region, which are in the corresponding position of joint edge of adjacent soil layers. To see a morr apparent result, a model with the same setting is built but changing the height to 1 meter, $K = \dfrac{H}{R_o - R_i} = \dfrac{1}{0.05} = 20$. The result is shown as below:

54
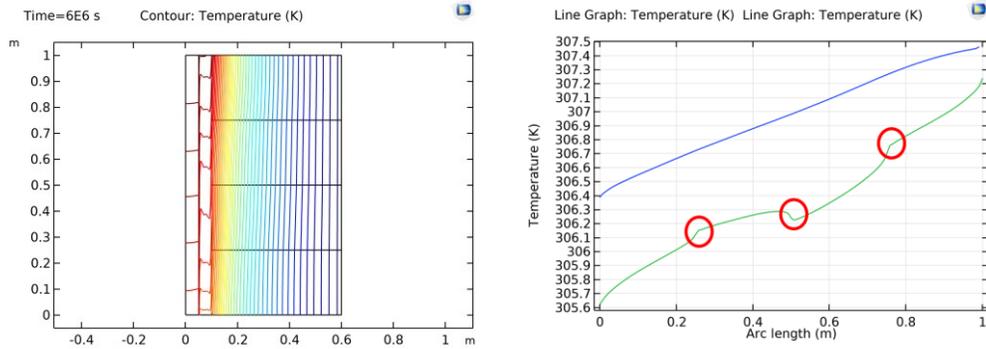
Figure 5-52: Temperature distribution of annulus with constant heat source [1m] (a) isothermal contours; (b) temperature along the boundary of inner cylinder and outer cylinder.

It can be found that due to the height extension, the bulges on the temperature plots become more apparent. These bulges indicate that the forming of hotspots is due to the influence of joint edge between each two adjacent soil layers with different thermal conductivities in the heat convectice transfer process. To verify this conclusion, heat source is replaced by isothermal layer to see if a similar result can be exported.

5.3.6 Isothermal layer versus Heat source

For a quicker temperature variation and a more efficient simulation, a constant temperature layer is used to replace heat source to set the inner cable domain for the heat transfer process. After replacing the original inner cylinder setting (heat source) with an isothermal layer (constant temperature on the boundary of cable, T_{cable} = 343.15K), the following temperature distribution plots are achieved and shown in Figure 5-53 and Figure 5-54.
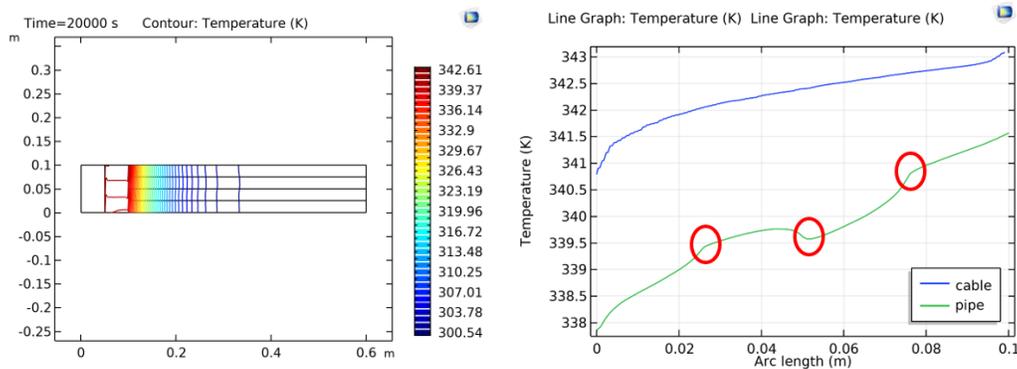
Figure 5-53: Temperature distribution of vertical annulus [0.1 m] with constant heat source (a) isothermal contours; (b) temperature along the boundary of inner cylinder and outer cylinder.

It is clear seen that some hotspots form at the interface between each two adjacent layer along the pipe boundary. Regarding to the problem of geometry size, a similar model with length of 1 meter is also tested. It can be found that the plot shows a similar tmeperature distribution as the case with 0.1 meter's height and even the temperature difference between bottom and top region does not change much.

55
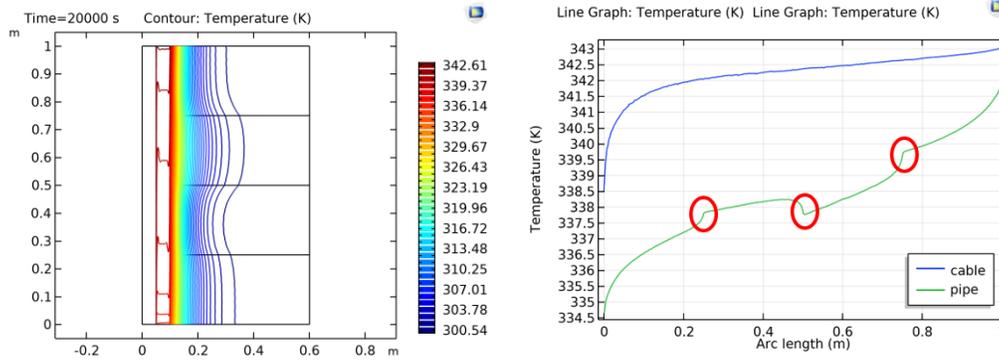
Figure 5-54: Temperature distribution of vertical annulus [1m] with isothermal cable (a) isothermal contours; (b) temperature along the boundary of inner cylinder and outer cylinder.

Generally, the hotspots exist in each model, no matter changing the height of the annulus or switching between heat source and isothermal layer function. An initial conclusion can be drawn that at the joint edge between each two adjacent soil layers, hotspot foroms if the thermal conductivity of soil drops in the positive y-axis direction.

Another important conclusion is about the application of heat source and isothermal layer function. It can be seen from Figure 5-51 and Figure 5-52 that in the annulus with cable as heat source, the temperature difference between top and bottom region on the surface of cable and pipe becomes larger with the height increase of the annulus. However, according to the temperature distribution plots in the annulus with isothermal cable in Figure 5-53 and Figure 5-54, it can be found in this case the temperature difference is approximately similar when the height increases from 0.1meter to 1meter. This is because according to the isothermal setting in COMSOL, the temperature in arbitrary position on the isothermal boundary will never change no matter heat conductive or convective transfer occurs.

In the following section, a case with higher temperature difference case (around 50K) needs to be discussed. Hence, it is not wise to continue using heat source condition since the soil area required to achieve the temperature difference (50 K) will be extremely large. As shown by a evaluation with eq. 5-1, in a conduction case, $T_{cable} = T_{boundary} + \Delta T = 343.15K$, $T_{boundary} = 293.15K$, the temperature difference $\Delta T = 50\ K = P * R_{general}$,

$$R_{general} = \frac{\Delta T}{P} = \frac{50}{30} = ln\left(1 + \frac{2t_1}{d_c}\right) * \frac{1/k}{2\pi}, \quad t_1 = \left(e^{\frac{4}{3}*\frac{2\pi}{\frac{1}{k}}} - 1\right) * \frac{d_c}{2} = 1765.55m$$

The radius of the soil space t_1 requires to be 1765.55 m to achieve the temperature increase in x-axis direction, which is a radius too large to be set in COMSOL.

5.4 Final scenario case

The analysis of previous completed cases has demonstrated that COMSOL has a good accessibililty to model heat transfer process. Dimensionless models of horizontal and vertical concentric cylinders in Section 4.1 and Section 4.2 shows flow motion change in the annulus with different combinations of Rayleigh number and Prandtl number. The scenario models of horizontal concentric and eccentric cylinders in Section 5.1 further prove the accuracy of COMSOL modelling by exporting result consistent with the experimental results in relevant paper.

Finally, the scenario model of horizontal directional drilling (HDD) with one cable installed in a pipe buried in layed soil is built. Considering the time cost and computation limit of computer, the original scenario model is scaled down to implement a feasible simulation. A cuboid with hight 24m, width 1.5m and depth 2.6m is set as geometry to represent the soil space where the HDD path crosses. The length of the pipe is 17.41m and the depth from ground to the surface is 1.85m. The angle

between horizontal and inclined pipes is 18 degree. The inclined pipe crosses five layers of soil with different thermal conductivity: $1\,W/m \cdot K$, $2\,W/m \cdot K$, $0.9\,W/m \cdot K$, $1.5\,W/m \cdot K$ and $0.7\,W/m \cdot K$ from top to bottom layer. Due to the drawback of heat source function found in Section 5.3.6, a fixed temperature layer "$T_w = 343.15\,K$" is set first on the surface of cable. The ambient temperature is set as $T_{ambient} = 300\,K$ on the surface of the cuboid.

Firstly, the Rayleigh number of the transverse section of the horizontal annulus in the bottom soil layer can be calculated based on the fluid properties evalauted with the film temperature ($T_f = \frac{T_{ambient} + T_W}{2} = 321.58\,K$):

$$L = \frac{D_o - D_i}{2} = 0.05m, \ Ra_L = \frac{g\beta c_p\,\rho^2}{k\,\mu}(T_i - T_o)\,L^3 = \frac{10 * 0.0004 * 4176.5 * 988.8^2}{0.7 * 5.62} * 43.15 * 0.1^3 \approx 1.8 * 10^5$$

The Prandtl number of water is $Pr = 5.45$. According to Table 4-1, Table 4-2 and Table 4-3, it can be determined that the natural convection in this case is in laminar regime and the relevant conclusions drawn in the previous chapters for laminar flow can be used here.

The final scenario case requires extremely fine mesh to make the simulation result grid-independent and the completed mesh setting is shown as below:
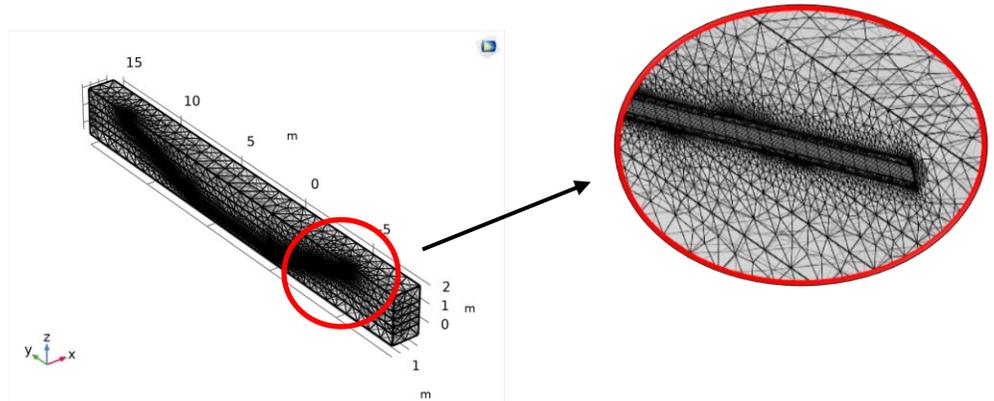
Figure 5-55: Mesh of the scenario case

After using extremely fine mesh, the temperature distribution along the pipe path is shown in Figure 5-56:
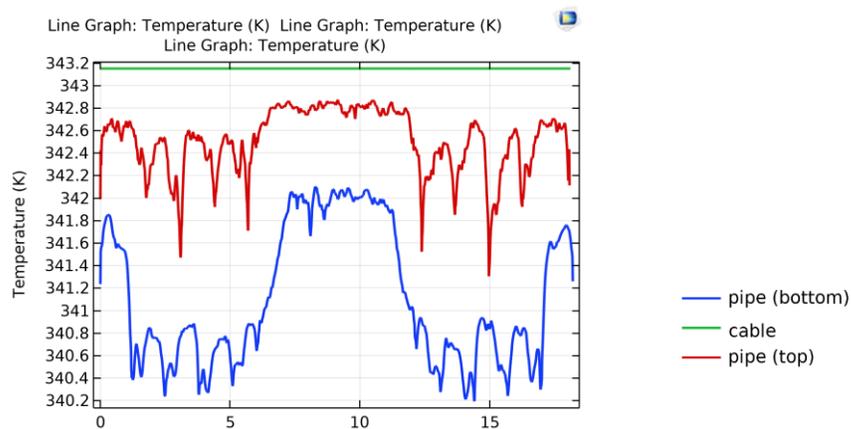
Figure 5-56: Temperature distribution of scenario model (using isothermal boundary condition

As it can be seen, the temperature distribution is not as expected since it does not reflect apparent characteristics of heat convective transfer along the pipe, especially on the inclined part (the temperature distribution is too homogeneous on the

top region of pipe surface). It is found that the reason is due to the isothermal setting on the surface of cable. If a fixed temperature is set in COMSOL, it means the temperature in arbitrary position on the surface of cable will never change no matter heat conductive or convective transfer occurs or not (as can be seen from the green line in Figure 5-56). Hence, the isothermal setting has an influence on the computation for convection in the area closed to the cable and therefore only heat conduction from the pipe surface to soil can be reflected in Figure 5-56. Due to the minimum thermal conductivity (0.7 W/m · K), the horizontal annulus section in the bottom soil layer shows the highest temperature increase along the pipe path. Following the x-axis direction from x=12 to x=18, the temperatures plot on pipe surface shows an oscillation in the inclined part, which is due to the variation of soil thermal conductivity (0.7 W/m · K−→ 1.5 W/m · K−→ 0.9 W/m · K−→ 2 W/m · K−→ 1W/m · K). Besides, due to the narrow annulus space between the cable and pipe, the temperature plots on pipe surface might also be distorted by the isothermal setting and hence the result is not reliable. New setting has to be applied instead of setting isothermal layer on the cable surface.

Since isothermal layer is proved to be wrong as boundary condtion for cable, applying heat source function is unavoidable. One factor should be considered that the original model has been scaled down and the width of soil space is only 1.5m (which means the distance between heat source and ambient isothermal layer is only 1.5m). Due to the influence of the geometry size to the magnitude of temperature increase discussed in Section 5.3.6, only a limited temperature increase can be obtained after replacing the isothermal condition with the heat source condition $Q_w = 31.72\ W/m$ in the cable domain. According to the evaluation by empricial equation 5-1, in pure conduction situation,

$$\Delta T = P * R_{general} = P * ln\left(1 + \frac{2t_1}{d_c}\right) * \frac{\frac{1}{k}}{2\pi} \approx 30 * 0.4 = 12K$$

The temperature change in convection mode should be smaller that in conduction mode with the same external conditions. Hence, only a temperature increase smaller than $12K$ can be expected. After running the new time-dependent model (with times $1*10^7$[s]), the steady-state reaches and the new temperature distribution plot with heat source setting in the cable domain is shown in Figure 5-57.
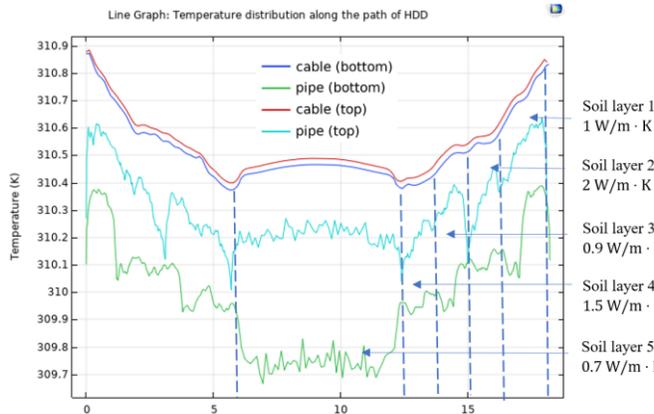
Figure 5-57: Temperature distribution of scenario model (using heat source function)
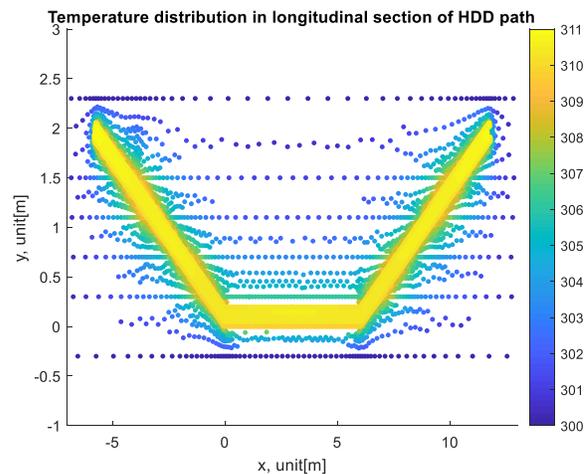
Figure 5-58: Temperature distribution in vertical longitudinal section of HDD path

It can be seen that, compared to the previous simulation with isothermal boundary condition, an obvious and continuous temperature increase is shown in Figure 5-57. One thing should be noted is that in the geometry setting, the pipe position is not perfectly symmetric with regard to the soil space around it. That's the reason why the temperature plots in Figure 5-57 are not perfectly symmetric about the vertical line in the middle position.

Comparing the temperature distribution on the bottom and top side of the pipe and cable, some conclusions can be drawn. In the middle part (from x=7 to x=12), which corresponds to the horizontal annulus section, the temperature on the upside is much higher than that on the underside of the pipe surface. This phenomenon is due to buoyancy force, which promotes the heated fluid (less dense) to move upwards and can be explained further by the conclusion drawn in Section 5.1 and Section 5.2. In the laminar regime, for the outer cylinder (pipe), the maximum temperature occurs at the top point of the horizontial annulus due to the raising plume (hot fluid). The temperature difference between upside and underside of the pipe is relatively large. For the inner cylinder (cable), the temperature on the upside surface is still higher than that on the downside surface , but the temperature difference is smaller compared to the outer cylinder (pipe). The oscillaion curve of the pipe temperature distribution might be due to the mesh setting. If a even better mesh setting can be applied, the plots of temperature distribution should be smoother. Due to the computation limit and time cost, this mesh improvement part can be set as future work.

The temperautre distribution shows a increase tendency in the inclined part of the HDD path from the bottom to the top soil layer. This indicates the existance of buoyancy force, which is formed due to inhomogeneous fluid properties. The heated fluid flow (with less densnsity) has a tendency to rise upwards and induces active heat convective transfer in the inclined part. In this region, following the x-axis direction from x=12 to x=18, the temperature increases and the plot shows a sawtooth waveform due to the variation of soil thermal conductivity ($0.7 \text{ W/m} \cdot \text{K} \rightarrow 1.5 \text{ W/m} \cdot \text{K} \rightarrow 0.9 \text{ W/m} \cdot \text{K} \rightarrow 2 \text{ W/m} \cdot \text{K} \rightarrow 1 \text{W/m} \cdot \text{K}$). The tendency of temperature increase is suppressed when the thermal conductivity increases (e.g. in the vertical direction from soil layer 3 to soil layer 2) while the temperature increase smoothly when the thermal conductivity decrease (e.g. in the vertical direction from soil layer 4 to soil layer 3).

To verify the conclusion drawn above about the influence of thermal conductivity, the thermal conductivity is changed by taking the reciprocal of the original value. It means now the inclined pipe crosses five layers of soil with different thermal conductivity: $1 \text{ W/m} \cdot \text{K}$, $0.5 \text{ W/m} \cdot \text{K}$, $1.11 \text{ W/m} \cdot \text{K}$, $0.67 \text{ W/m} \cdot \text{K}$ and $1.43 \text{ W/m} \cdot \text{K}$ from the top to the bottom layer. The temperature distribution along the cable and pipe surface with this new thermal conductivity layed soil is shown as below:
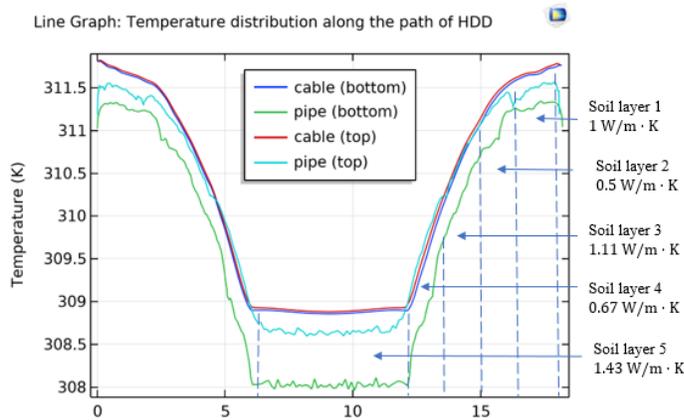

Figure 5-59: Temperature distribution of scenario model (using heat source function)
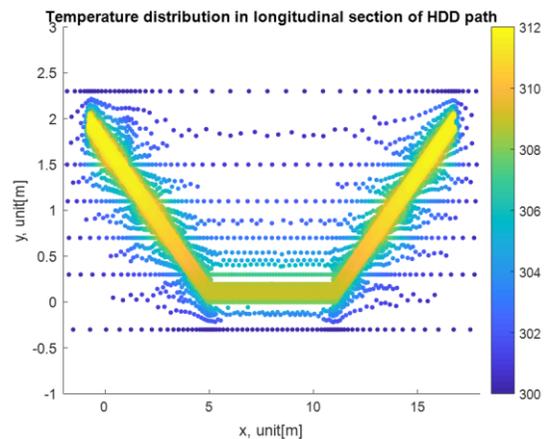
Figure 5-60: Temperature distribution in vertical longitudinal section of HDD path

In the horizontal annulus section part (from x=7 to x=12), the temperature plot is smoother compared to Figure 5-57 and the temperature on the upside is still higher than that on the underside of the pipe surface due to natural convection of water. For the inner cylinder (cable), the temperature difference between upside surface and downside surface is small compared with pipe. The temperautre distribution shows a smoother increase plot in the inclined part of the HDD path from the bottom to the top soil layer compared to Figure 5-57. In this case, even the thermal conductivity variation of soil still exist, the plot has no obvious sawtooth waveform like Figure 5-57. The reason is reserved for future study.

Generally, due to natural convection of water in the annulus, the temperature on the upside of pipe surface is much higher than that on the underside, especially in the horizontal section. The temperature on the cable surface shows a similar distribution compared to the pipe but the temperature difference between upside and underside is relatively smaller. In the inclined section, both pipe and cable show a temperature increase with the reduction of depth. The tendency of temperature increase is suppressed when the thermal conductivity of soil increases, and vice versa. Due to the limit of computation performance, the scenario model is scaled down in COMSOL modelling (the actual HDD path should be around 500 meters while in COMSOL model it is only 18 meters). The simulation result in COMSOL might differ from the scenario data. This drawback can be improved in the future work by improving the mesh setting and scaling up the geometry size.

6 CONCLUSION

The discussion from the previous chapters can lead to the following conclusions:

1. The objective to build a 3D time-dependent model in COMSOL, taking into account of laminar flow in fluids, heat transfer in soilds and fluids, to investigate the influence of layered soil structure on temperature distribution and location of hotspots along the HDD path is met.

2. For dimensionless model in Chapter 3 and Chapter 4,

   - The benchmark method applied in Chapter 3 validated the feasibility of studying buoyancy flow problems in COMSOL and the completed unit space model can be used for analysis of natural convection cases in the future.

   - For horizontal annulus in Chapter 4, in general, the flow is stable in $10^2 \leq Ra_L \leq 10^6$ and becomes turbulent when $Ra_L \geq 10^7$. The transition Ra_L, which corresponds to the transitory stage from laminar to turbulent flow, varies with different Prandtl number Pr.

   - In vertical cylinder case in Chapter 4,, the increase of radius ratio develops the convection flow while the increase of aspect ratio suppresses it. Multi celluars (vortices) form when the aspect ratio equals 15.

3. For scenario model in Chapter 5,

   - It was found that for 3D horizontal cylinders, the maximum temperature occurs in the top region of the concentric annulus while it occurs in the bottom region of the eccentric annulus.

   - In 3D vertical concentric cylinder case, the temperature is much hotter in the top region compared to the bottom region due to buoyancy force. The temperature increase is suppressed when the thermal conductivity of soil increases in the positive vertical direction, and vice versa.

   - In the model with a cable installed in a pipe buried in HDD path, the highest temperature occurs on both ends of the HDD path. In the inclined section, both pipe and cable show a temperature increase with the reduction of depth. Hotspots form at the joint edge between soil layers when the thermal conductivity decrease in the position vertical direction.

7 FUTURE WORK

Based on the results in this thesis, additional research goals can be proposed. In this chapter, some accessible improvement ideas are summarized based on the issues found in previous chapters.

The scenario model was simplifed in this thesis due to mesh complexity and computation performance limit in COMSOL. The cable was set as a solid inner cylinder without considering the structure of conductor, screen, sheath or insulation. In the future work, the structure of cable can be added to the current model to build a more accurate 2D scenario model and then developed into 3D model step by step.

The heat source function in COMSOL provides an approach to observe the dynamic process of heat convective transfer and natural convection of water. In this project, "heat source" condition (set in cable domain) is used in collocation with "isothermal"condition (set on the boundary of soil space) to build a enclosed space with temperature difference, which causes the occurrence of natural convection flow and heat convective transfer in water. However, the issues of expsensive time cost and high requirement of computer performance cannot be ignored. The problem of long simulation time can be improved with a better boundary condition setting. The "heat flux" condition is recommended to replace the "isothermal" condition to set on the boundary of soil space. The reason why the "heat flux" condition was not used in this project is because a heat convective transfer coefficient is required when setting this condition in COMSOL. COMSOL can implement simulations more close to reality and save the computation time if the heat transfer coefficient from layed soil to the air can be measured and calculated according to scenario data. After that, the current scenario model can be extended to larger size according to actual engineering requirement.

In this thesis, it is assumed that the total energy loss of cable (ohmic loss of conductor, sheath loss and dielectric loss) is constant with the "heat source" condition. However, in reality, the resistance of cable is temperature dependent and so the heat production in the conductor changes with temperature variation. The heat is produced by the current through the conductor. By applying "Livelink" function, COMSOL model can be imported into MATLAB to modify and operate with the command line and scripts. Scenario data of current value with regard to time in power system can be imported into MATLAB synchronously to provide a real-time input for the heat source condition.

8 REFERENCES

[1] *Bejan, Adrian, and Allan D. Kraus, eds. Heat transfer handbook. Vol. 1. John Wiley & Sons, 2003.*

[2] *S. Sukhatme, A Textbook On Heat Transfer, Universities Press (India) Private Limited, Hyderabad, India, 2005.*

[3] *de Vahl Davis G, Jones I P. Natural convection in a square cavity: a comparison exercise[J]. International Journal for numerical methods in fluids, 1983, 3(3): 227-248.*

[4] Kuehn T H, Goldstein R J. An experimental and theoretical study of natural convection in the annulus between horizontal concentric cylinders[J]. Journal of Fluid mechanics, 1976, 74(4): 695-719.

[5] Kuehn T H, Goldstein R J. An experimental study of natural convection heat transfer in concentric and eccentric horizontal cylindrical annuli[J]. 1978.

[6] "The CFD Module User's Guide - COMSOL Documentation," [Online]. Available: https://doc.comsol.com/5.4/doc/com.comsol.help.cfd/CFDModuleUsersGuide.pdf.

[7] *Gonzalez O, Stuart A M. A first course in continuum mechanics[M]. Cambridge University Press, 2008.*

[8] *G.G. Stokes, Trans. Camb. Phil. Soc., 8, pp. 287–305, 1845.*

[9] COMSOL, "Using the Boussinesq Approximation for Natural Convection," [Online]. Available: https://www.comsol.com/blogs/using-the-boussinesq-approximation-for-natural-convection/.

[10] *Multiphysics C. Introduction to COMSOL multiphysics®[J]. COMSOL Multiphysics, Burlington, MA, accessed Feb, 1998, 9: 2018.*

[11] *Kuehn T H, Goldstein R J. Correlating equations for natural convection heat transfer between horizontal circular cylinders[J]. International Journal of Heat and Mass Transfer, 1976, 19(10): 1127-1134.*

[12] *Çengel, Yunus A. (2002). Heat and Mass Transfer (Second ed.). McGraw-Hill. p. 336.*

[13] W. S. o. Engineering, "The Nusselt Number," 03 April 2019. [Online]. Available: https://pages.jh.edu/~virtlab/heat/nusselt/nusselt.htm.

[14] *Incropera F P, Lavine A S, Bergman T L, et al. Fundamentals of heat and mass transfer[M]. Wiley, 2007.*

[15] *de Bruyn J R, Bodenschatz E, Morris S W, et al. Apparatus for the study of Rayleigh–Bénard convection in gases under pressure[J]. Review of scientific instruments, 1996, 67(6): 2043-2067.*

[16] "Raithby G D, Hollands K G T. A general method of obtaining approximate solutions to laminar and turbulent free convection problems[M]//Advances in heat transfer. Elsevier, 1975, 11: 265-315".

[17] *Fusegi T, Hyun J M, Kuwahara K, et al. A numerical study of three-dimensional natural convection in a differentially heated cubical enclosure[J]. International Journal of Heat and Mass Transfer, 1991, 34(6): 1543-1557.*

[18] *Yang X, Kong S C. Numerical study of natural convection in a horizontal concentric annulus using smoothed particle hydrodynamics[J]. Engineering Analysis with Boundary Elements, 2019, 102: 11-20.*

[19] *de Vahl Davis G. Natural convection of air in a square cavity: a bench mark numerical solution[J]. International Journal for numerical methods in fluids, 1983, 3(3): 249-264.*

[20] *Wang P, Zhang Y, Guo Z. Numerical study of three-dimensional natural convection in a cubical cavity at high Rayleigh numbers[J]. International Journal of Heat and Mass Transfer, 2017, 113: 217-228.*

[21] *Bilski S M, Lloyd J R, Yang K T. An experimental investigation of the laminar natural convection velocity field in square and partitioned enclosures[C]//International Heat Transfer Conference Digital Library. Begel House Inc., 1986.*

[22] *Krane R J. Some detailed field measurements for a natural convection flow in a vertical square enclosure[C]//Proceedings of the First ASME-JSME Thermal Engineering Joint Conference, 1983. 1983, 1: 323-329.*

[23] Bilski S M, Lloyd J R, Yang K T. An experimental investigation of the laminar natural convection velocity field in square and partitioned enclosures[C]//International Heat Transfer Conference Digital Library. Begel House Inc., 1986.

[24] CrashCourse, "Stress, Strain & Quicksand: Crash Course Engineering #12," 9 8 2018. [Online]. Available: https://www.youtube.com/watch?v=ouTJkNLepF0.

[25] "Kaminski D A, Jensen M K. Introduction to thermal and fluids engineering[M]. John Wiley & Sons, 2017".

[26] Coulson J M, Richardson J F, Backhurst J R, et al. Chemical Engineering Vol. 1: Fluid Flow[J]. Heat Transfer and Mass Transfer, 1999, 1: 204.

[27] Luo K, Yi H L, Tan H P. Eccentricity effect on bifurcation and dual solutions in transient natural convection in a horizontal annulus[J]. International Journal of Thermal Sciences, 2015, 89: 283-293.

[28] Davis G D V, Thomas R W. Natural convection between concentric vertical cylinders[J]. The Physics of Fluids, 1969, 12(12): II-198-II-207.

[29] Sheikholeslami M, Gorji-Bandpy M, Ganji D D, et al. Effect of a magnetic field on natural convection in an inclined half-annulus enclosure filled with Cu–water nanofluid using CVFEM[J]. Advanced Powder Technology, 2013, 24(6): 980-991.

[30] Bishop E H, Mack L R, Scanlan J A. Heat transfer by natural convection between concentric spheres[J]. International Journal of Heat and Mass Transfer, 1966, 9(7): 649-662.

[31] Farouk B, Gu¨c¸eri S I. Laminar and turbulent natural convection in the annulus between horizontal concentric cylinders[J]. 1982.

[32] Yeh C L. Numerical investigation of the three-dimensional natural convection inside horizontal concentric annulus with specified wall temperature or heat flux[J]. International journal of heat and mass transfer, 2002, 45(4): 775-784.

[33] M. G. Niasar, "Lecture 3 – Cable accessories, cable ampacity, and cable installation," High Voltage Cable system, p. 46, 2020.

[34] Cho C H, Chang K S, Park K H. Numerical simulation of natural convection in concentric and eccentric horizontal cylindrical annuli[J]. 1982.

[35] https://en.wikipedia.org/wiki/Vorticity#Mathematical_definition.

[36] Shan X. Simulation of Rayleigh-Bénard convection using a lattice Boltzmann method[J]. Physical Review E, 1997, 55(3): 2780.